

POLITECNICO DI TORINO

Corso di Laurea Magistrale in Ingegneria Civile

Tesi di Laurea Magistrale



**Influence of DCFP bearing properties on
the seismic performance of isolated
bridges**

Relatore: Prof. Castaldo Paolo

Candidato:

Roberto Gnisci 230926

Marzo 2018

Acknowledgements

Abstract

This work analyzes the behaviour of a continuous bridge isolated with Double Concave Friction Pendulum (DCFP) under seismic excitation. The main purpose is to understand how the bridge behaviour is affected by the isolation parameters, and to find optimal solutions for isolation. The investigation technique is based on non-linear time-history analyses, from which response parameters are post-processed to serve the objective of this study.

Chapter 1 focus on the reason why it is necessary to protect bridges from earthquakes, explaining the main risks for bridges in seismic zones.

Chapter 2 focus on the state of the art of seismic design of building and bridges, especially of isolation devices.

Chapter 3 focus on the mathematical basis of the seismic isolation, particularly for the FPS (Friction Pendulum System) and the DCFP.

Chapter 4 describe the MATLAB model used for the analyses and the choices made to achieve it. Particularly, the comparison between the MATLAB model and another one, developed with another software, is of vital importance to attest the validity of the study and of its results.

Chapter 5 focus on the performed analyses and on the results. The analyses take into account a wide range of variability for the dynamic characteristics of the structure and the seismic uncertainty, performing a high number of non-linear time-history analyses. Results are finally given in non-dimensional form, in order to carry out a parametrical analysis of peak responses of the system, finding optimal values of friction coefficient and performing regression analyses to obtain closed-form expressions useful to design DCFP isolators.

Chapter 6 discusses the results of the analyses, the possible future developments of the research and provides an example of application of the results.

Index of content

1	SEISMIC RISK	1
1.1	VULNERABILITY EVALUATION	2
1.1.1	<i>Empirical methods.....</i>	2
1.1.2	<i>Methods based on expert's evaluations.....</i>	3
1.1.3	<i>Analytical methods.....</i>	3
1.2	SEISMIC HAZARD EVALUATION.....	4
1.2.1	<i>Seismic hazard abroad</i>	7
1.2.2	<i>The strongest documented earthquakes.....</i>	9
1.3	SEISMIC RISK FOR BRIDGES	9
1.4	SEISMIC DAMAGES IN BRIDGES.....	10
1.4.1	<i>Failure for excessive displacements.....</i>	11
1.5	PIER FAILURE.....	12
1.5.1	<i>Flexural failure.....</i>	13
1.5.2	<i>Inadequate flexural ductility.....</i>	14
1.5.3	<i>Inadequate dimensioning of anchorage length.....</i>	14
1.5.4	<i>Shear failure</i>	14
1.6	FAILURE CONSEQUENCES	15
1.6.1	<i>Cost of repair</i>	16
2	DESIGN STRATEGIES AND ISOLATION	17
2.1	VIBRATIONS CONTROL.....	17
2.2	SEISMIC BASE ISOLATION IN STRUCTURES	19
2.3	HISTORICAL NOTES ON SEISMIC ISOLATION	21
2.4	SEISMIC ISOLATION IN ITALY	25
2.4.1	<i>Gervasutta Hospital, Udine</i>	25
2.4.2	<i>Del Mare Hospital, Naples.....</i>	26
2.4.3	<i>C.A.S.E. Project, L'Aquila.....</i>	28
2.5	SEISMIC ISOLATION ABROAD.....	31
2.5.1	<i>San Francisco City Hall.....</i>	31
2.5.2	<i>Bolu Viaduct (Turkey)</i>	33
2.6	ELASTOMERIC SEISMIC DEVICES.....	36
2.6.1	<i>Laminated rubber bearing.....</i>	37
2.6.2	<i>High Damping Rubber Bearing (HDRB)</i>	37
2.6.3	<i>Lead Rubber Bearing (LRB).....</i>	38
2.7	SLIDING ISOLATORS	38
2.7.1	<i>Plane sliding isolators: Friction Slider</i>	39

2.7.2	Friction Pendulum System (FPS)	39
3	DYNAMIC OF ISOLATED SYSTEMS	41
3.1	LINEAR THEORY OF SEISMIC ISOLATION	41
3.2	FRICTION PENDULUM SYSTEM	46
3.2.1	Dynamic behaviour	48
3.3	FRICTION	51
3.3.1	Adhesion	52
3.3.2	Plowing	52
3.3.3	Visco-elastic effects	53
3.3.4	Stick-slip phenomenon	53
3.3.5	Modeling of the friction-velocity behavior	54
3.3.6	Effect of load permanence and travelled path	56
3.3.7	Effect of normal load variation over seismic behaviour of device	57
3.4	MODELLING CRITERIA	58
3.4.1	Linear modelling	59
3.4.2	Non-linear modelling	60
3.5	DCFP	60
3.6	TRIPLE FP BEARING	63
4	MODEL	65
4.1	VALIDATION OF THE MODEL	71
4.2	FPSs MODEL VALIDATION	74
4.3	DCFPs MODEL VALIDATION	76
5	PARAMETRICAL ANALYSIS	80
5.1	INPUT PARAMETERS OF THE SYSTEM	80
5.1.1	Pier main period T_p	80
5.1.2	Isolation period T_d	80
5.1.3	Mass ratio of the pier to the deck	81
5.1.4	Seismic input	81
5.1.5	Normalized friction coefficients Π_μ	82
5.2	DCFP PARAMETERS	83
5.3	DIMENSIONLESS PARAMETERS	84
5.3.1	Additional parameters	86
5.3.2	DCFPs deformations	87
5.3.3	Single FPSs deformations	87
5.3.4	Pier cap displacement	87
5.3.5	DCFP forces	87
5.4	STATISTICAL HYPOTHESES	88

5.5	RESULTS.....	89
5.5.1	Case A.....	89
5.5.2	Case B.....	101
5.6	OPTIMAL FRICTION VALUES	113
5.6.1	Case A.....	114
5.6.2	Case B.....	116
5.7	REGRESSION ANALYSES.....	117
5.7.1	Case A.....	119
5.7.2	Case B.....	129
6	CONCLUSIONS.....	139
6.1	OPTIMAL FRICTION VALUES	140
6.2	REGRESSION ANALYSES.....	140
6.3	PRACTICAL APPLICATION.....	141
6.4	FUTURE DEVELOPMENTS.....	142
7	REFERENCES	143

Index of figures

Figure 1.1 - Map of seismic hazard in terms of expected PGA with exceeding probability of 10% in 50 years	4
Figure 1.2 - Seismic reliability	5
Figure 1.3 - Europe seismic hazard map	7
Figure 1.4 - U.S.A. seismic hazard map	8
Figure 1.5 - Viaduct collapse caused by Northridge earthquake, California, 1994.	11
Figure 1.6 - Failures for loss of support: Kobe earthquake (Japan, 1995) on the left and Jiji earthquake (Taiwan, 1999) on the right	12
Figure 1.7 - Pounding damages: Kobe earthquake (Japan, 1995) on the left and Sichuan Earthquake (China, 2008) on the right	12
Figure 1.8 - Deck overturning due to piers failure, Kobe earthquake (1995)	13
Figure 1.9 - Interaction diagram of a pier	13
Figure 1.10 - Shear failure of the piers, Northridge earthquake (California, USA, 1995)	15
Figure 1.11 - Failure of Oakland Bay Bridge	16
Figure 2.1 - Control theory	18
Figure 2.2 - Fixed base (left) vs. base isolation (right)	19
Figure 2.3 - Pseudo-acceleration and displacement spectra	20
Figure 2.4 - Swiss Full Base Isolation System, Skopje, Macedonia, 1969	22
Figure 2.5 - Building isolated with rubber bearings	23
Figure 2.6 - Behaviour of laminated rubber bearing	23
Figure 2.7 - Électricité-de-France system	24
Figure 2.8 - Gervasutta Hospital piers	26
Figure 2.9 - Gervasutta Hospital, isolation devices detail	26
Figure 2.10 - Del Mare Hospital, plane-volumetric view	27

Figure 2.11 - Del Mare Hospital, installation of the isolators.	28
Figure 2.12 - View of the residential complex C.A.S.E. project	29
Figure 2.13 - Base plate of C.A.S.E. project	30
Figure 2.14 - C.A.S.E. Isolators -	30
Figure 2.15 - Installed isolator, C.A.S.E. project	31
Figure 2.16 - San Francisco City Hall	31
Figure 2.17 - Rubber bearings at the base of columns and shear walls	32
Figure 2.18 - Bolu Viaduct (Turkey)	33
Figure 2.19 - Bridge scheme and fault direction	34
Figure 2.20 - Retrofit scheme at typical interior pier	35
Figure 2.21 - Friction Pendulum Isolation bearing	36
Figure 2.22 - Laminated rubber bearing (Bridgestone)	37
Figure 2.23 - Laminated high damping bearing (Bridgestone)	37
Figure 2.24 - Lead rubber bearing (Bridgestone)	38
Figure 2.25 – Friction Slider (FIP Industriale)	39
Figure 3.1 - Model of a single storey isolated structure	41
Figure 3.2 - Modal shapes	44
Figure 3.3 - Friction Pendulum System behaviour	47
Figure 3.4 - FPS isolator (FIP Industriale)	47
Figure 3.5 – Pendulum behaviour	48
Figure 3.6 - FPS's bi-linear behaviour.	50
Figure 3.7 - Hysteretic behaviour of a FPS.	51
Figure 3.8 - View of a junction, apparent and true area of contact.	52
Figure 3.9 - Stick-slip phenomenon.	53
Figure 3.10 - Dependency of friction coefficient from sliding velocity and pressure	55
Figure 3.11 – Friction vs sliding velocity diagram	56

Figure 3.12 - DCFP conceptual sketch	61
Figure 3.13 - Push-over curves for tri-linear and bi-linear DCFPs	62
Figure 3.14 - Cross section of the Triple FP bearing	63
Figure 3.15 - Comparison between analytical, experimental and modeled behaviour	64
Figure 4.1 - General scheme of an isolated continuous bridge.	65
Figure 4.2 - Model scheme	66
Figure 4.3 – Simulink Model	71
Figure 4.4 – Simulink sub-model for instantaneous friction evaluation	71
Figure 4.5 - Test earthquake record	72
Figure 4.6 - Deck displacement comparison (FPS)	74
Figure 4.7 - Pier cap displacement comparison (FPS)	75
Figure 4.8 - Abutment isolator force-displacement law comparison (FPS)	75
Figure 4.9 - Pier isolator force-displacement law comparison (FPS)	76
Figure 4.10 - SAP2000 DCFP model	78
Figure 4.11 - Deck displacement comparison (DCFP)	78
Figure 4.12 - Pier cap displacement comparison (DCFP)	79
Figure 4.13 - Force-displacement law comparison (DCFP)	79
Figure 5.1 - Relation between DCFP radii and isolation period	81
Figure 5.2 - Response spectra of the used earthquakes and average spectrum	82
Figure 5.3 - Relation between curvature radii when $R_1/R_2 = 2$.	84
Figure 5.4 - Force-displacement behaviour of abutment DCFP under seismic excitation for $r_f = 4$ (red) and $r_f = 2$ (blue).	84
Figure 5.5 - Scaled response spectra (unitary value for $T = 3$ s)	85
Figure 5.6 - Scaled seismic spectra (unitary value for $T = 3$ s), detail	86
Figure 5.7 - CDF and PDF obtained from analysis results for the 30 seismic events for $T_d = 2$ s, $T_p = 0.1$ s, $l_p = 0.1$, $f = 0.3/g$, case A	88

Index of tables

Table 1.1 – Relation between exceeding probability in 50 years and return period according to NTC08	5
Table 1.2 - Ground types according to NTC08.....	6
Table 1.3 - The strongest documented earthquakes	9
Table 4.1 – FPSs model, modal period comparison.....	74
Table 4.2 - DCFPs model, modal period comparison	77
Table 5.1 – Input parameters	80
Table 5.2 - Earthquakes used and their main characteristics.	82
Table 5.3.....	90
Table 5.4	91
Table 5.5.....	92
Table 5.6	93
Table 5.7.....	94
Table 5.8	95
Table 5.9	96
Table 5.10.....	97
Table 5.11	98
Table 5.12.....	99
Table 5.13.....	100
Table 5.14.....	102
Table 5.15.....	103
Table 5.16.....	104
Table 5.17.....	105
Table 5.18.....	106
Table 5.19.....	107

Table 5.20.....	108
Table 5.21	109
Table 5.22.....	110
Table 5.23.....	111
Table 5.24.....	112
Table 5.25 - Optimal dimensionless friction: median values (case A)	114
Table 5.26 - Optimal dimensionless friction: 16th and 84th percentiles (case A)	115
Table 5.27 - Optimal dimensionless friction: median values (case B).....	116
Table 5.28 - Optimal dimensionless friction: 16th and 84th percentile (case B)	117
Table 5.29 - Regression analysis results (friction and pier cap displacement - A)	119
Table 5.30 - Numerical vs regression results: optimal dimensionless friction (left) and pier cap displacement (right) for the 50th, 16th and 84th percentiles (case A).	120
Table 5.31 - Regression analyses results (x_6).....	121
Table 5.32 - Numerical vs regression results (x_6)	122
Table 5.33 - Regression analysis results (x_7 - A)	123
Table 5.34 - Numerical vs regression results (x_7 - A).....	124
Table 5.35 - Regression analysis results (x_8 - A)	125
Table 5.36 - Numerical vs regression results (x_8 - A).....	126
Table 5.37 - Regression analysis results (x_9 - A)	127
Table 5.38 - Numerical vs regression results (x_9 - A).....	128
Table 5.39 - Regression analysis results (friction and pier cap displacement - B)	129
Table 5.40 - Numerical vs regression results: optimal dimensionless friction (left) and top pier displacement (right) for the 50th, 16th and 84th percentiles (case B).	130
Table 5.41 - Regression analysis results (x_6 - B).....	131

Table 5.42 - Numerical vs regression results (x_6 - B)132

Table 5.43 - Regression analysis results (x_7 - B)133

Table 5.44 - Numerical vs regression results (x_7 - B).....134

Table 5.45 - Regression analysis results (x_8 - B).....135

Table 5.46 - Numerical vs regression results (x_8 - B)136

Table 5.47 - Regression analysis results (x_9 - B)137

Table 5.48 - Numerical vs regression results (x_9 - B) 138

1 Seismic risk

Seismic hazard (H) is the probability that an earthquake will occur in a geographical area within a given window of time, and with ground motion intensity, expressed in term of magnitude M or PGA (*peak ground acceleration*), exceeding a given threshold.

Seismic consequences depend also by building resistance to earthquake effects. The potential damage that a building may suffer is called Vulnerability (V). The more a building is vulnerable, the worse the consequences that may affect it would be, and this is determined by the structural typology, a possible inadequate design, the possible use of poor materials, construction methods or lack of maintenance.

At last, the number of economic activity exposed to the risk, the possibility of damage in economic term, from either the historical or the architectural point of view or in sense of human losses is called Exposition (E). This loss is quantified in term of costs that have to be sustained to bring the system back to the previous state.

Combining the three terms introduced above, the seismic Risk is defined as the damage expected in a given window of time, for a certain type of earthquake, a given building resistance and from the quality and quantity of activity exposed to possible damages.

(NTC, 2008)

$$R = H \cdot V \cdot E \quad (1.1)$$

Leaving aside the Exposition, the Seismic Risk is defined as the failure probability of a building in a given window of time. The limit state function Z is negative if the limit state condition is reached or exceeded. The probability of having a negative Z is then called failure probability P_f . In earthquake engineering, this limit state function may be expressed comparing two variables: seismic demand (D), understood as the performance required to the structure

during the earthquake, and the structural capacity (C), understood as the dynamic response of the structure. The failure probability may be then expressed as:

$$P_f = P[Z \leq 0] = P[C \leq D] \quad (1.2)$$

1.1 Vulnerability evaluation

As previously said, the vulnerability is the sum of the potential damages to people, buildings and businesses. Three types of vulnerability are defined:

- Direct vulnerability, the propensity of a single elements to be damaged by effect of an earthquake;
- Induced vulnerability, the propensity of a structure to suffer a structural crisis because of the failure of a single element;
- Delayed vulnerability, or the effect occurring after earthquakes.

The first step is define the Intensity Measure (IM) and the damaging level. The first may be a peak value of an earthquake, such as the PGA (Peak Ground Acceleration) or the PGV (Peak Ground Velocity), or a significant spectral acceleration or velocity value.

Fragility or vulnerability curves estimates the probability to reach or exceed the limit states for various type of structures. There are three methods to define them:

- Empirical methods, based on the available data of historical earthquake damages;
- Methods based on expert judgement;
- Analytical methods.

1.1.1 Empirical methods

Empirical methods provide information on seismic vulnerability of many categories of structures. This approach is based on real data but may show some limits: firstly, it is difficult to find an amount of data large enough to create a database; secondly, fragility curves must be related to groups of structures and not to specific structures, which are the object of these methods. Lastly, these methods cannot provide any information about the seismic vulnerability of modern

buildings, since it is likely that they are constructed with new techniques and material and there are not available data on their seismic damages or failure.

1.1.2 Methods based on expert's evaluations

These methods are used generally where there are not data available. Experts and specialists use their own evaluations to construct fragility curves for many values of IM, waiting for a collection of actual data. However, these evaluations do not have a true scientific basis, and it is not possible to have reliable data in new or unpredictable conditions where not even the experts have experience. In Italy, first and second level vulnerability charts are drawn by the GNDT (National Group for Earthquakes Defence) of the CNR (National Research Centre).

1.1.3 Analytical methods

Analytical methods may be used to determine fragility curves, when a database of earthquake-induced damages is available or when lab experiments are too much expensive. Several types of analyses may be used to build the fragility curves: static or dynamic, linear or non-linear. Naturally, computational time increases with the required accuracy. The most used method is the non-linear dynamic analysis.

1.2 Seismic Hazard evaluation

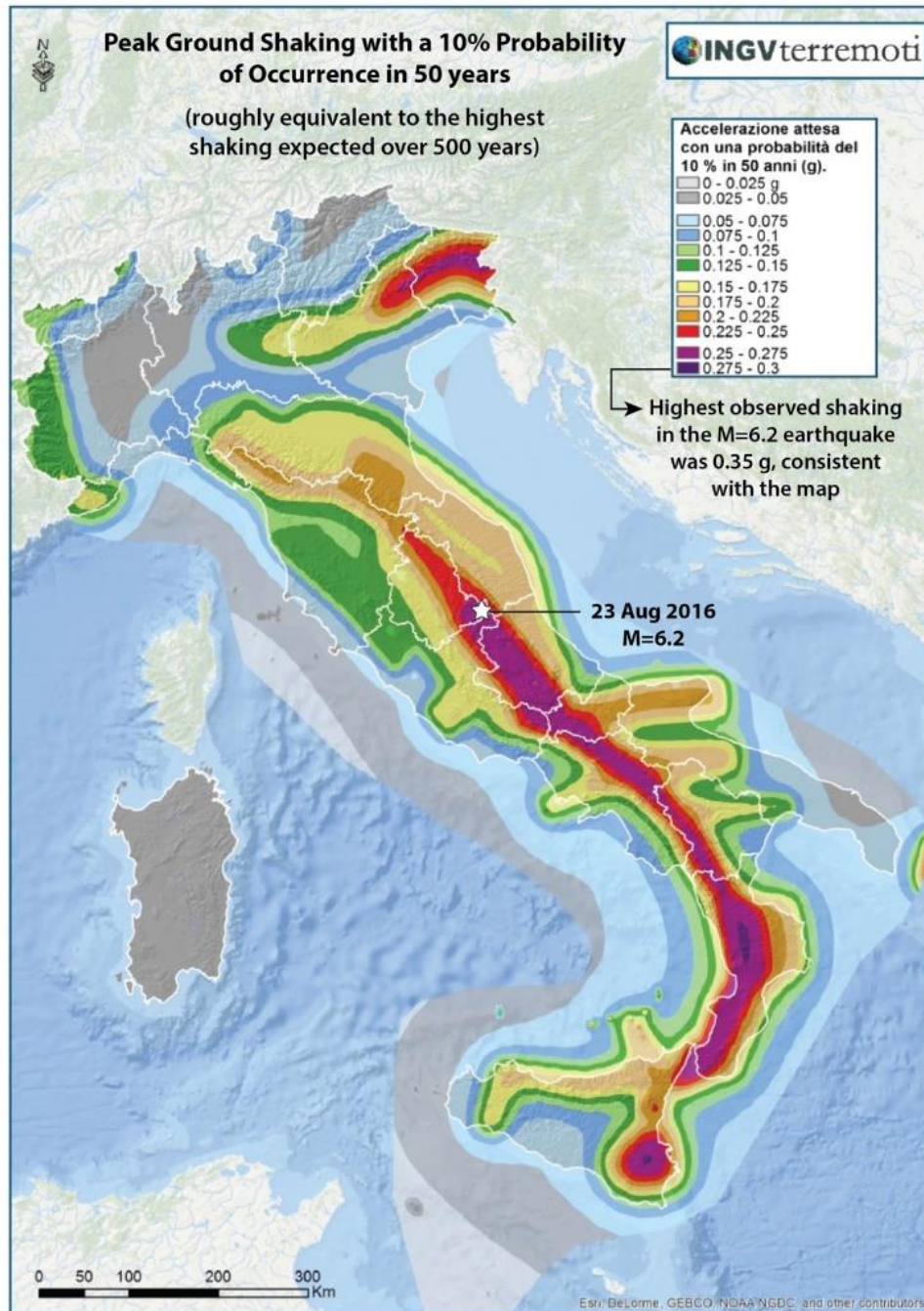


Figure 1.1 - Map of seismic hazard in terms of expected PGA with exceeding probability of 10% in 50 years

Thanks to the work of the Italian INGV (National Institute of Geophysics and Volcanology) and of the Department of Civil Protection, maps of seismic hazard are available for the entire Italian territory. This is the result of the S1 project (DPC-INGV S1 Project, 2106)

The project consisted in running probabilistic analyses that resulted in defining a grid extended to the entire Italian territory. Points of the grid are spaced with a

maximum distance of 5 km (about 0.5° of latitude and longitude). The results of this study were integrated in the NTC08. Maps of seismic hazard are available in terms of expected PGA and for hard ground, which means very stiff soils (cat. A according to EC8, which means with $v_{s,30} > 800$ m/s). Data are available for the following lists of:

Exceeding probability in 50 years [%]	81	63	50	39	30	22	10	5	2
Return period [years]	30	50	72	100	140	200	475	975	2475

Table 1.1 – Relation between exceeding probability in 50 years and return period according to NTC08

Seismic hazard maps were drawn through acceleration spectra, S_{pa} , for the following vibrational periods: 0.1, 0.15, 0.2, 0.3, 0.4, 0.5, 0.75, 1, 1.5 and 2 s.

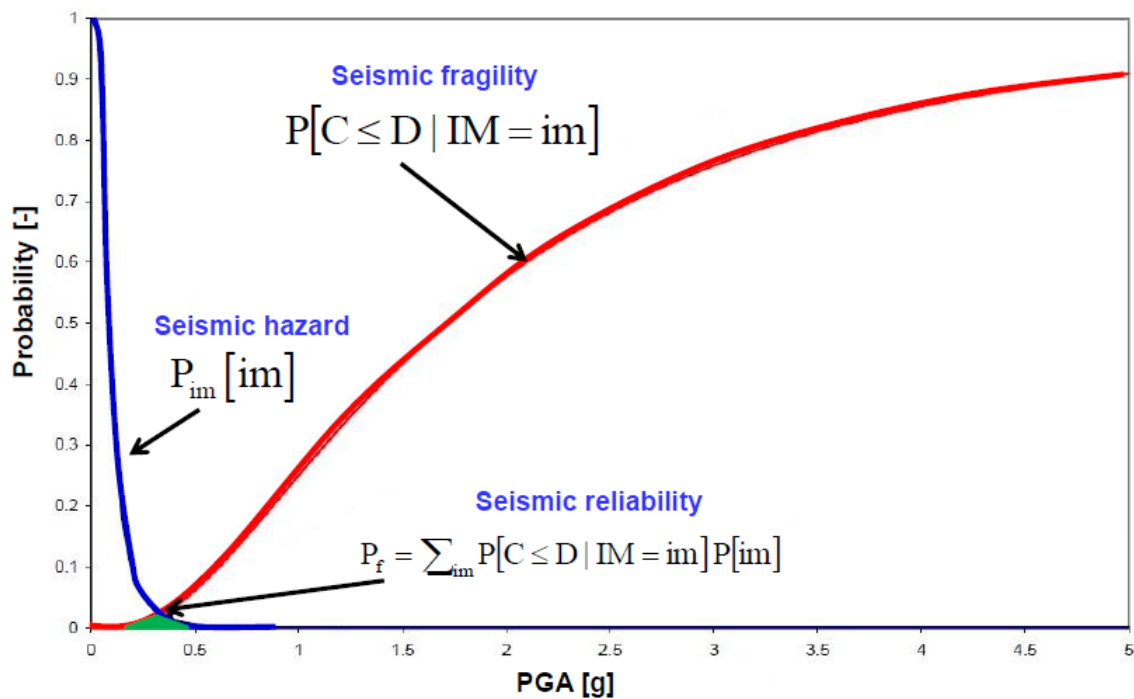


Figure 1.2 - Seismic reliability

Ground type	Description of stratigraphic profile	Parameters		
		$v_{s,30}$ (m/s)	N_{SPT} (blows/30cm)	c_u (kPa)
A	Rock or other rock-like geological formation, including at most 5 m of weaker material at the surface	> 800	—	—
B	Deposits of very dense sand, gravel, or very stiff clay, at least several tens of m in thickness, characterised by a gradual increase of mechanical properties with depth	360 – 800	> 50	> 250
C	Deep deposits of dense or medium-dense sand, gravel or stiff clay with thickness from several tens to many hundreds of m	180 – 360	15 - 50	70 - 250
D	Deposits of loose-to-medium cohesionless soil (with or without some soft cohesive layers), or of predominantly soft-to-firm cohesive soil	< 180	< 15	< 70
E	A soil profile consisting of a surface alluvium layer with v_s values of type C or D and thickness varying between about 5 m and 20 m, underlain by stiffer material with $v_s > 800$ m/s			

Table 1.2 - Ground types according to NTC08

1.2.1 Seismic hazard abroad

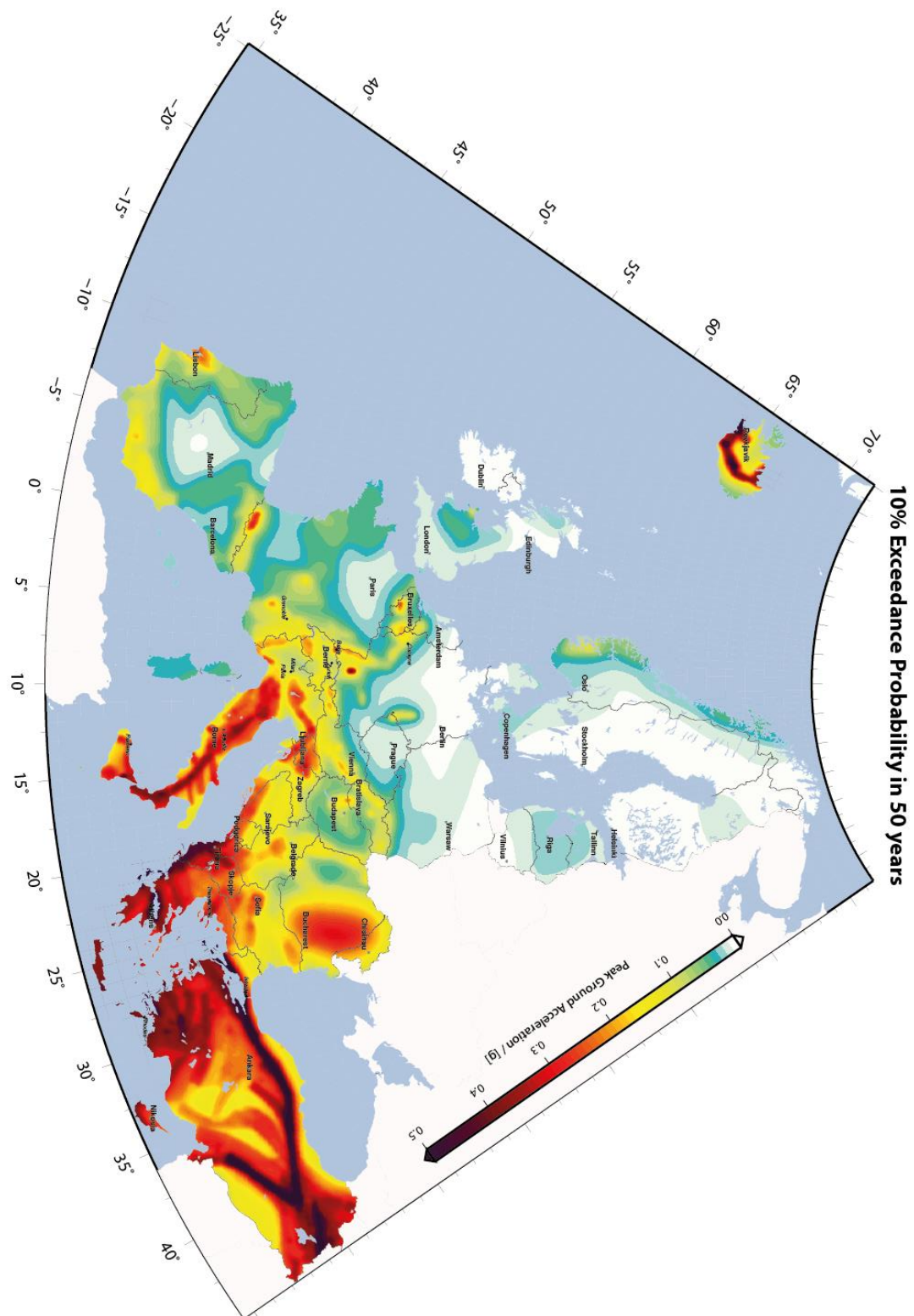


Figure 1.3 - Europe seismic hazard map

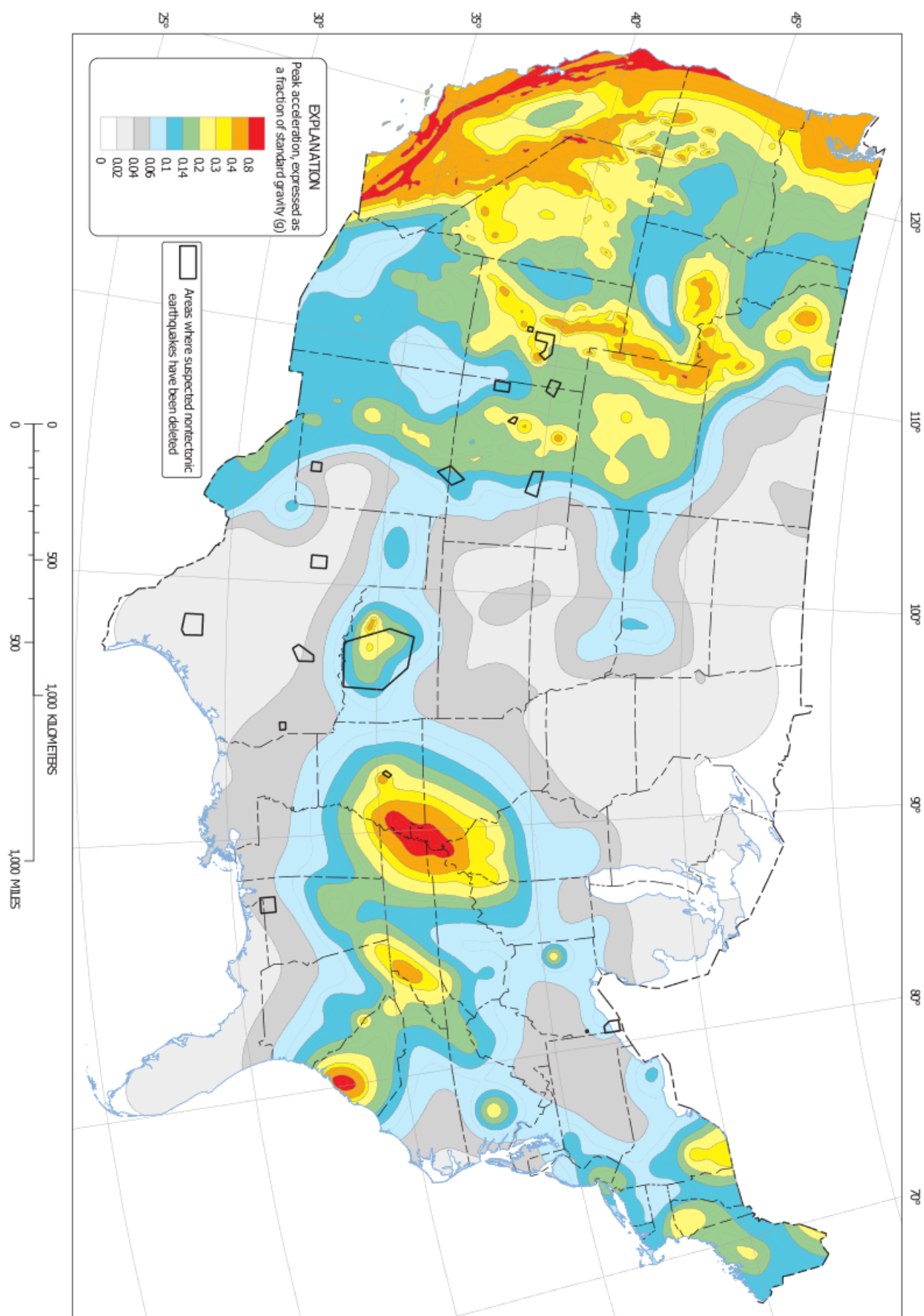


Figure 1.4 - U.S.A. seismic hazard map

1.2.2 The strongest documented earthquakes

	Date	Location	Magnitude
1	May 22, 1960	Valdivia (Chile)	9.5
2	March 28, 1964	Prince William Sound (Alaska, USA)	9.2
3	December 26, 2004	off the west coast of Sumatra (Indonesia)	9.1
4	November 4, 1952	Kamchatka (URSS, now Russia)	9.0
5	August 13, 1868	Arica (Peru, now Chile)	9.0
6	January 26, 1700	Subduction zone of Cascadia (USA, Canada)	9.0
7	March 11, 2011	Sendai and Tōhoku (Japan)	8.9
8	February 27, 2010	Pelluhue (Chile)	8.8
9	January 31, 1906	Esmeraldas Coast (Ecuador)	8.8
10	February 4, 1965	Rat Islands (Alaska, USA)	8.7

Table 1.3 - The strongest documented earthquakes

1.3 Seismic risk for bridges

Bridges are a fundamental part of the infrastructure of a nation, since they are necessary to cross valleys, rivers, straits, etc. establishing a physical link between geographical areas which otherwise would be physically separated. This allows the develop of mobility and commerce, and to save money instead of spending for alternative path or alternative means of transportation. Bridges are anyway exposed to natural disasters such as earthquakes or tsunamis that may damage or even destroy them.

Nowadays, in an increasing traffic demand context that contrasts with the ageing of the infrastructure, it is of vital importance to assess and choose carefully which viaduct and bridges need to be reinforced and which ones not. The evaluation of seismic safety is affected by some uncertainties, of which many are related to the deterioration of the structures, due to environmental causes, utilization, previous seismic events, etc.

Most of the Italian highway network includes bridges and viaducts constructed after World War II, especially between 1960 and 1980, a period remembered in history as a true economic boom. During those years, not only most of the current knowledge on concrete degradation was still unknown, but also seismic forces were not taken into account in design. For those reasons, the oldest bridges and viaduct are unable to resist to earthquakes. A proper evaluation of the seismic hazard has been conducted only lately, and before the introduction of the new building codes, there was no use of the ductility or energy dissipation concepts in structural design.

Structural ductility was introduced only with the NTC08, within a design method known as *capacity design*, which allows the formation of plastic hinges in the structures dissipate energy during earthquakes and aim to avoid shear failure mechanisms, which are known to be fragile. Energy dissipation reduces seismic base shear forces, increasing the safety of the structure.

These considerations imply that old structures need to be adjusted through consolidation, and that new structures must be designed with new criteria. Consolidation is usually preferable to demolition and reconstruction, even if the results are not the same in terms of seismic performance, because of the reduced costs. The consolidation type depends usually by structural scheme, load types and structural elements characteristics and materials.

1.4 Seismic damages in bridges

Seismic damages and failure for bridges are classified according to the part of the bridge that is effectively involved in the failure mechanism (usually a pier, a longitudinal beam or a joint). In a wider sense, also failures connected to the Serviceability Limit States (SLSs) are meant, such as excessive vertical displacement in the deck mid-span or failure of non-structural parts of the superstructure (Lapointe, 2004).

1.4.1 Failure for excessive displacements



Figure 1.5 - Viaduct collapse caused by Northridge earthquake, California, 1994.

Excessive lateral displacements are one of the main reasons of damaging and failure for bridges during earthquakes. Underestimate the lateral force and/or overestimate the lateral stiffness of the superstructures may lead to an inadequate design of seismic resistant bridges. For reinforce concrete bridges, there are two typical examples of failure mechanism: *loss of support* and *pounding*.

In addition, excessive displacements in longitudinal direction may lead to the collapse through the superstructure disassembly, while in case of presence of adjacent structures transversal displacements may lead to repeated collisions that may severely damage both the bridge and the adjacent structure.

- **Failure for loss of support**

This type of failure is particularly problematic for simply supported bridges when seismic intensity is high in the longitudinal direction of the deck. If in this direction the available bearing space is not enough, the entire superstructure may loss support and fall down. Typically, this type of failure occurs in bridges with high piers and long spans, especially in case of soft soil.



Figure 1.6 - Failures for loss of support: Kobe earthquake (Japan, 1995) on the left and Jiji earthquake (Taiwan, 1999) on the right

- **Failure for pounding**

Pounding in a bridge is caused by excessive displacements of part of the structure. It may take place where the deck is very close to other structures, whether they are part of the bridge or not. The unconstrained movement in these regions may lead to repeated collisions that can severely damage the deck. This type of damaging may even occur between jointed parts of the deck, or between deck and abutment.



Figure 1.7 - Pounding damages: Kobe earthquake (Japan, 1995) on the left and Sichuan Earthquake (China, 2008) on the right

1.5 Pier failure

Pier failure during an earthquake is a significant type of failure, since it implies the collapse of the entire bridge: this is why the purpose of isolation in bridges is to protect the piers from the horizontal action coming from the deck. The mechanisms that occurs in pier failure may be a flexural or a shear one.



Figure 1.8 - Deck overturning due to piers failure, Kobe earthquake (1995)

1.5.1 Flexural failure

The inadequate flexural resistance of the bridges built during 80s and 90s years is generally due to the use of conventional seismic design action of about 4-10% of structure's weight. Nowadays, it is an acquired knowledge that lateral elastic response forces may indeed go beyond dead weights.

Elastic design is based on a linear interaction between M and N , but if plastic resources of the materials are taken into account, the interaction diagram become a parabola with horizontal axis. The loads acting on a pier generally induce a small compressive stress, and at that level it may not be available an adequate flexural resistance to dissipate enough energy during high-intensity earthquakes.

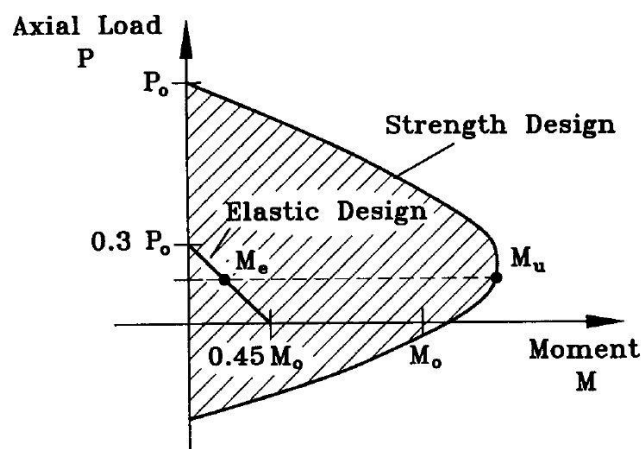


Figure 1.9 - Interaction diagram of a pier

1.5.2 Inadequate flexural ductility

Ductility is a fundamental parameter in seismic design, and it may be defined as the ability of a structural element to undergo large plastic deformations without collapsing. If a structure is designed to resist earthquakes with Capacity Design, it will necessarily need ductility to deform itself as much as needed to dissipate seismic energy through the formation of plastic hinges. Low ductility would prevent the formation of plastic hinges, making the structure resist to earthquakes thanks to its strength only, which is usually impossible.

1.5.3 Inadequate dimensioning of anchorage length

Improper calculation of anchorage and overlapping length of reinforcing bars in the columns leads to a premature reaching of steel yielding in anchorage and overlap zones, causing the formation of plastic hinges in undesirable position, leading to partial or global failure of the structure.

1.5.4 Shear failure

The different shear mechanisms share a complex relationship, for this reason it is difficult to outline the characteristics of a shear failure respect to a flexural failure. While flexural failure is usually ductile and shows many evidence before occurring, shear failure is a fragile mechanism: in a collapse, many failures may combine themselves leading to an after-collapse scenario where the main cause of the collapse may not be easy to detect. Failure of transversal reinforcement is a classical example of shear failure, and it leads to a reduction in concrete compressive strength in longitudinal direction; this is why buckling of the longitudinal reinforcing bars usually accompanies shear failure. This type of failure described is usually called shear-compression failure. Short piers are sensible to shear failure since they are subjected to a high shear respect to the bending moment (high ratio V/M).



Figure 1.10 - Shear failure of the piers, Northridge earthquake (California, USA, 1995)

1.6 Failure consequences

Bridges are hardly ever intended to be a stand-alone element, but they are practically always a part of a wider infrastructure system, such as roads, highways, speedways or railways. Hence, collapse consequences usually hit areas much greater than their geographical position, especially for strategic bridges: in this case, the performance of the entire infrastructure web of which they form part are drastically reduced.

- Loss of human lives.
- Bridge replacement cost.
- Loss of utilities.
- Loss of elements of architectural merit.
- Cost of provisional measures.
- Cost related to web congestion.
- Social impact costs, incurred by companies and community. These costs include journey variation of public transports, longer journeys for emergency vehicles and economic impact on local industries and companies.

For example, the Oakland Bay Bridge (San Francisco, CA) has been closed for 30 days after the Loma Prieta earthquake (1989), forcing 250,000 daily users to radically change their habits: many commuters were forced to lengthen significantly their daily travel, while others switched to using railways or bus transportation. Many retailers and workers of the delivery sector suffered reductions of business. If this closure did last years, it would have caused severe change in the socio-economic system of San Francisco and beyond.



Figure 1.11 - Failure of Oakland Bay Bridge

The estimation of the losses after a major earthquake is a difficult operation. Losses can be grouped in three types:

- Direct economic losses (bridge damaging, cost of repairs);
- Indirect economic losses (users delaying, impact on economic growth);
- Non-economic losses (deaths, injuries, environmental and social damages);

1.6.1 Cost of repair

Once a bridge collapse, it may be reconstructed to let it fulfill its task as a part of an infrastructure. While determining the importance of a bridge, it is explicitly assumed that this has to be reconstructed (otherwise, it would not have sense to evaluate its importance). In the particular case, where the benefits given by the bridge are inferior to the cost of reconstruction, this one would not be reconstructed usually.

To estimate the cost of reconstructions of a bridge, it is generally supposed that it is reconstructed exactly as it was before. This hypothesis is made to ease the task of the engineers that have to estimate the costs before it is constructed. Reconstruction costs are usually related to civil engineering works and may be estimated in accord to current costs of material and labour, structural geometry e geographical position (Imhof, 2004).

2 Design strategies and isolation

Since the 70s, traditional design methods for earthquake resistant structures were purely elastic, ruling out any chance of controlling ductility resources of structural elements and dissipating energy through them. (Priestley, Seible, & Calvi, 1996).

Ductility, i.e. the ability of a material to deform itself while undergoing constant stresses, is nowadays recognized as a crucial resource of a proper seismic design. Increasing the strength of the structure and of its elements would mean bear higher costs and would imply anyway to accept large acceleration acting on the structure during earthquakes: this point is often crucial, since it may cause the damaging of non-structural elements and make the entire structure condemned for the occupants and the users. Increasing the overall ductility of the structure, through a design that aim to create favorable plastic mechanism in the structure that can avoid the structure collapse. This strategy, that implements the principle of the hierarchy of the resistances, is called *Capacity Design*.

2.1 Vibrations control

Nowadays, the approaches currently used to protect structures from earthquakes are derived from a dynamic's branch, which is called theory of vibrations control. According to this theory, vibrations induced by dynamic forces, such as wind or earthquakes, are controlled by devices that cannot be considered as structural components.

- Passive control consists in a fixed change in the physical parameters of the structure. Seismic isolators and supplementary dampers are examples of passive control devices.
- Active control uses some external adjustable, or active, device (actuator) to provide control forces. Unlike passive control, active control depends on current measurements (feedback or feed-forward/closed-loop).

- Hybrid control mixes
- Semi-active control consists in an adjustable change in the physical parameters of the structure, which does not require any addition of energy into the system.

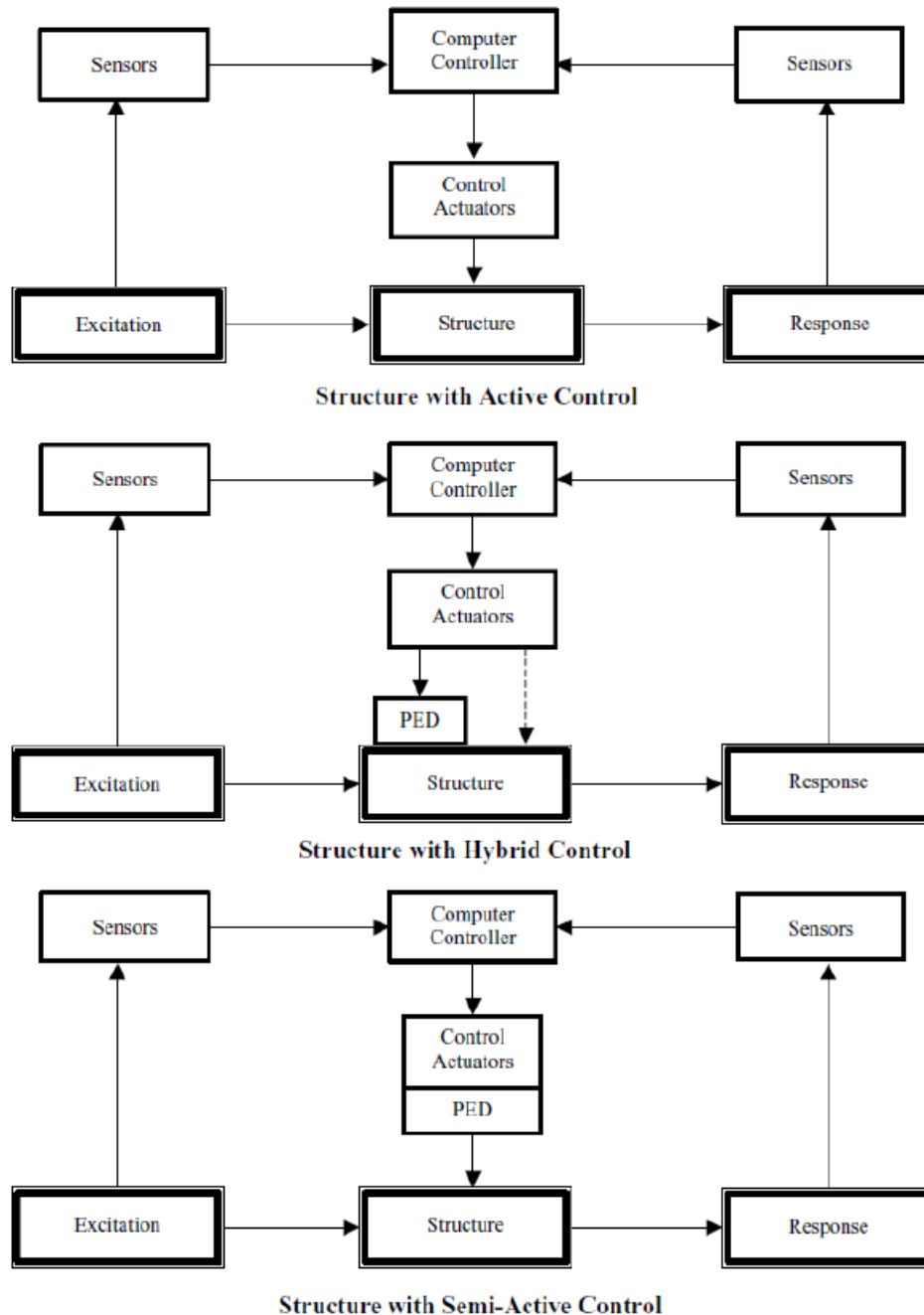


Figure 2.1 - Control theory

In order to protect structures from earthquake damaging and maintain their functionality, many strategies have been formulated in the recent years. Leaving aside strategies like *capacity design*, the best one nowadays adopted is the installation of isolators and/or dampers. While the firsts allow uncoupling the

structure from the motion of the ground, drastically reducing the energy and forces transmitted during earthquakes, the second reduces forces transmitted through structural elements by dissipating energy, thanks to viscous or viscoelastic hysteresis cycles. In both cases, the non-linearity of the devices usually have to be taken into account.

2.2 Seismic base isolation in structures

Seismic base isolation consists usually in the interposition of low lateral stiffness and high vertical rigidity elements, accompanied by high dissipative ability, between the ground and the superstructure, reducing the acceleration perceived by the latter during earthquakes. Horizontal ground shaking and structure motion result then uncoupled, reducing drastically the energy transmitted from the ground to the superstructure. Isolators act like filters, modifying amplitude and frequency content of harmonic components of seismic excitations.

Since seismic excitations have a high energetic content in correspondence of frequency typical the short and medium-rise buildings (1-10 Hz), isolators have the main scope of filter these frequencies. In addition, a proper design of isolator devices must take into account the dynamic characteristics of the structure and of the ground, to avoid undesirable and dangerous phenomena, such as resonance.

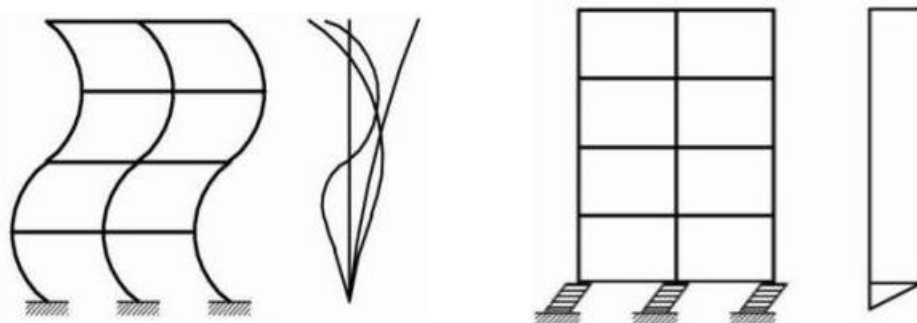


Figure 2.2 - Fixed base (left) vs. base isolation (right)

The principle of seismic isolation is to lengthen the main vibrational period of the structure from the fixed-base typical period (0.3-1.5 s) to values in the range 2-4 s, where the acceleration spectra do not reach high values. On the other hand, displacement spectra show in that region large displacements, while they are limited in the fixed-base period range. The isolators should then absorb this high demand in term of displacements, since they are very deformable in horizontal direction. To improve the performance of the isolators, they should be able to

dissipate part of the energy transmitted by the earthquake, using mechanism such as a friction or viscous damping.

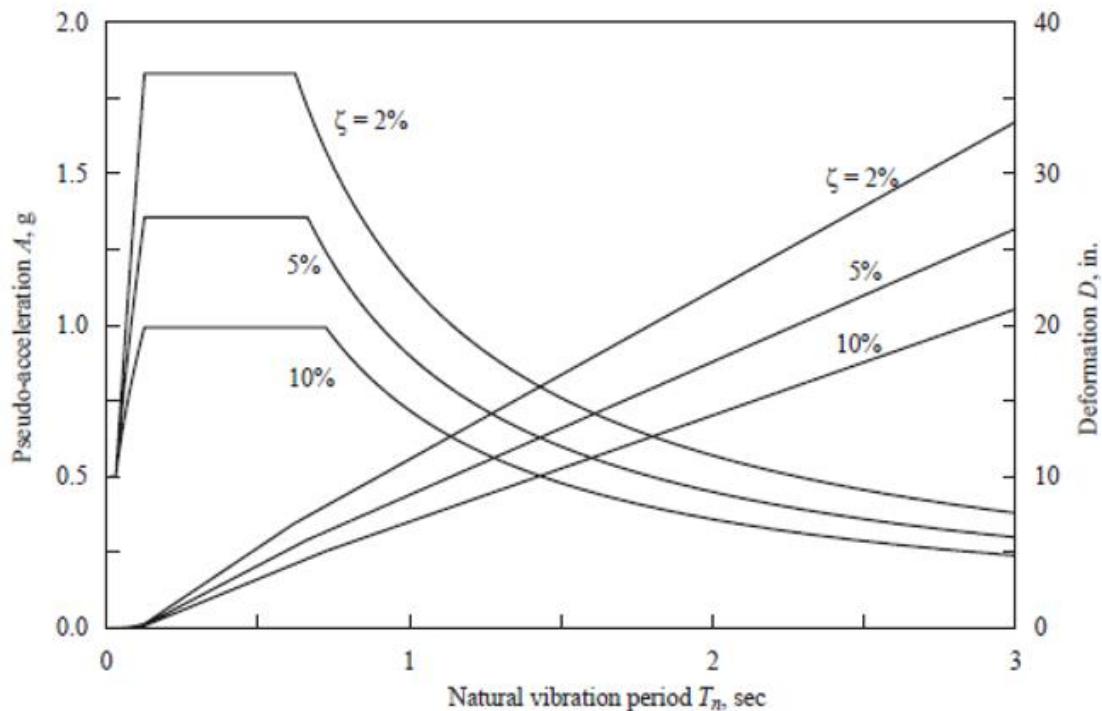


Figure 2.3 - Pseudo-acceleration and displacement spectra

Consequently, two positive effects, not feasible in fixed-base structures, are observed:

- A significant reduction of the acceleration transmitted to the part of the structure above of the isolators (the superstructure);
- A significant reduction of the inter-story drifts. This is because the isolators generate a rigid block-like behaviour in the superstructure, absorbing a vast part of the deformations.

In terms of construction technique, the main advantages are:

- The structure stays in elastic field, avoiding structural damaging that may cause reduction in the vertical bearing capacity;
- Non-structural elements may result not damaged even after strong earthquakes;
- Buildings and infrastructures are fully operative immediately after the earthquake;
- Buildings are perceived as safe structures, reducing the stress and the panic of the occupants during seismic events.

It follows that in a well designed base isolated structure, the behaviour of the entire system is governed practically only by the first modal shape, which has a period very close to the isolation period.

The efficiency of the isolation depends then on the ratio between the fundamental frequency of the sole superstructure ω_s and the frequency of the superstructure moving rigidly along with the isolators ω_{is} . This ratio is defined *Seismic Isolation Grade*:

$$I_d = \frac{\omega_s}{\omega_{is}} = \frac{T_{is}}{T_s} \quad (2.1)$$

The seismic response of the superstructure increases with the increasing I_d , and in the meantime the displacement of the first storey tends to increase sensibly in correspondence of small value of this ratio.

This work focuses on the isolation of bridges, whose mechanism of isolation are different from buildings'. Generally, a bridge superstructure consists in a multi-span deck supported by piers, which form, together with the foundation, the substructure. The isolation system is placed between the piers and the deck.

In this way, it is possible that deck, piers and abutments remain in elastic field even in the Ultimate Limit State (ULS) combinations. Designers are then allowed to not apply the capacity design, neither the details for ductility, regardless of the materials used in the construction (concrete or steel), allowing a consistent save of money and time required by the construction process.

2.3 Historical notes on seismic isolation

After Messina's earthquake in 1908, whose death toll stood at 160,000 people, the Italian government set up a technical committee with the purpose to propose adequate techniques of protection and reconstruction of the destroyed areas; back then the vast majority of the buildings were built in masonry and without any particular seismic precaution. The commission brought up two possible solutions: the first was to base isolate the rebuilt buildings, through the interposition between buildings and ground of sand and rollers right below the bearing columns; the second approach philosophy was to limit the height of the buildings. In addition, it was proposed for the first time to adopt a basic static seismic analysis, introducing lateral forces to simulate the earthquake effect. This second idea was

accepted instead of the first one, postponing once again the introduction of isolation techniques, even if rudimental.

In 1929, it was introduced the *flexible first storey concept* thanks to R. R. Martel. This concept consist in introducing flexible columns at the first floor of a building to lengthen the main vibrational period of the structure. The following developments came with the studies of Green (1935) and Jacobsen (1938), with the *soft first storey method*, introducing the idea of absorbing energy through material yielding. The Olive View Hospital of Los Angeles was built applying this concept, even if it revealed itself not successful because of the vast damaging caused by San Fernando earthquake in 1971, soon after the end of construction of the hospital. The structural system was evidently unable to work, but it was somehow useful to learn a lesson: it is not possible to absorb seismic energy with just a single storey of columns. In 1969, the first pioneering application of the base isolation was put in practice with the construction of the elementary school Johan Heinrich Pestalozzi in Skopje, Macedonia. The Swiss engineers who designed the building used for the first time a system, called *Swiss full base isolation 3d*, consisting in 5 simple non-reinforced rubber bearings, obtained by square rubber layers, 70 cm wide and 7 cm thick.



Figure 2.4 - Swiss Full Base Isolation System, Skopje, Macedonia, 1969

The absence of reinforcing steel in the rubber sheets caused the bearing to have not enough vertical rigidity, which was comparable to the lateral rigidity. This caused the structure to have not enough resistance to rocking motion, a mechanism that occurs during earthquakes and that may cause overturning of the entire building.

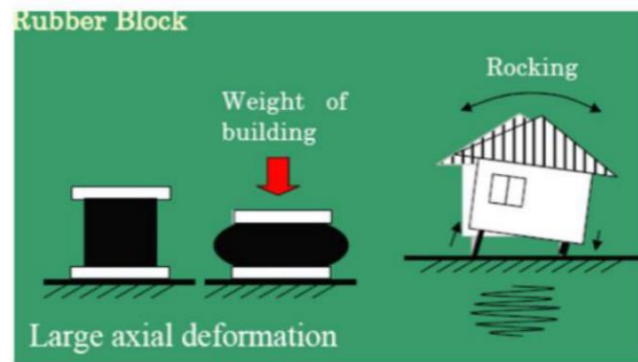


Figure 2.5 - Building isolated with rubber bearings

During the 70s, the Malaysian Rubber Producers' Research Association (MRPRA) started to produce in England the first elastomeric devices in reinforced rubber, throughout a production process base on vulcanization of rubber layers with steel plates.

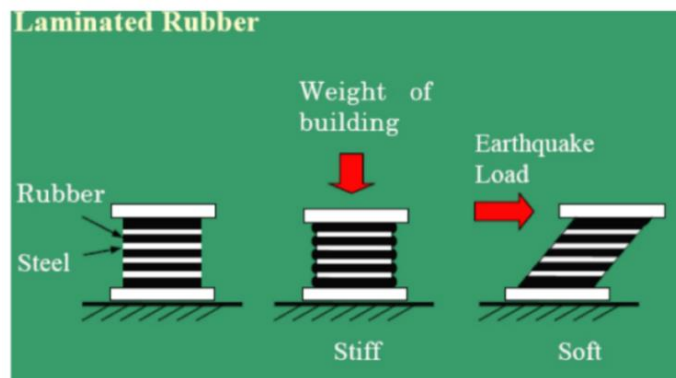


Figure 2.6 - Behaviour of laminated rubber bearing

A first large-scale application was carried out in France to protect nuclear plants from earthquakes with expected PGAs of about 0.2g. The main requisite was to leave unaltered the existing structure, and for this purpose, bearing in laminated neoprene and steel were used. In high seismicity regions, also sliding devices, with a friction coefficient of 20%, were used.

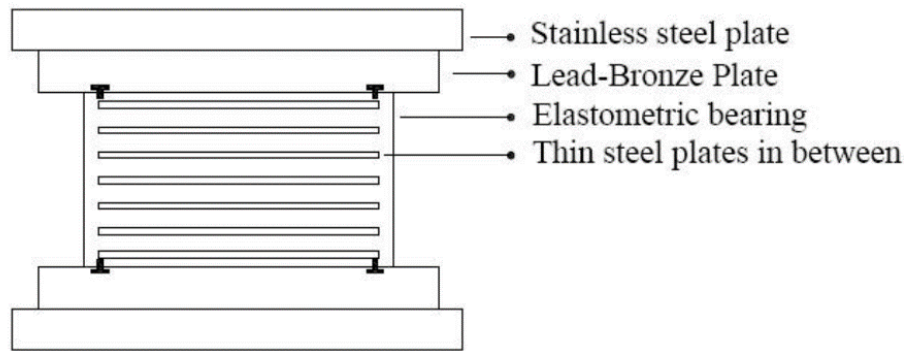


Figure 2.7 – Électricité-de-France system

The system was a combination of elastomeric bearing and sliding device: a neoprene core reinforced with steel plates and connected to lead-bronze plate, in the turn connected to a stainless steel plate. Neoprene has small deformability, and when the displacement capacity provided by it was reached, steel plates started to slide over lead-bronze plates. Except for the neoprene core, there was no re-centering device

Apart from the elastic contribution of the neoprene during the unloading phase, there was no re-centering feature in this type of isolator. Maintenance of the devices was then mandatory after every major earthquake.

During the 80s, the seismic isolator were for the first time diffused and used all around the globe, especially in the USA, Japan and New Zealand.

Isolation systems may also be used for retrofit of existing buildings, especially for the ones of historical or architectural merit, where introducing shear walls and/or dissipative bracing would be undesirable. The technical difficulties are anyway manifold. Base isolation can not be used if the foundation system consists of isolated footings, but it must be a rigid concrete slab situated just above the isolation plane; otherwise, a new foundation has to be realized. In any case, it is necessary to shore up the building during construction of the isolation and foundation systems, and installing the isolators may be very complicated, depending on the existing structural scheme.

Another problem is related to the motions that occur during a seismic event once the isolators are effective: the structure's relative displacement respect to the ground may be very large, and this could not be compatible with existing utilities such as plumbing, electrical, and telephone lines, which may happen to pass underground.

2.4 Seismic isolation in Italy

The Somplago viaduct on the Udine-Carnia highway, designed by Eng. Renzo Medeot was the first modern example of isolated bridge. From that first experience, isolation has been applied again for more than 150 bridges, reaching 150.000 linear meters of isolated deck in the entire country. By contrast, only a small number of buildings takes advantage of the base isolation, because of the lack of a national code or rules in the subject. In addition to that, the bureaucratic procedures necessary to obtain the approval by the *National Council of Public Works* were long and complex. Nevertheless, the potential owned by Italian engineers was, and still is, immense. The *Vigili del Fuoco Home Base* is the first Italian base-isolated building: it was built in the early 1980s, designed by Prof. Federico Massimo Mazzolani, of the *Engineering School Federico II* of Naples.

2.4.1 Gervasutta Hospital, Udine

This is the first medical facility realized In Italy with base isolation. It is a reinforced concrete frame building of 2338 m², where the base isolation purpose is to maintain the full functionality of the hospital during, and after, “rare” seismic events (PGA = 0.35g). In this way, it has been possible to reduce the deformation of the structural parts of the building but also the deformations of the non-structural parts, such as operating tables, monitoring, diagnostic and resuscitation machinery, etc.

Fifty-two elastomeric isolators have been used, with the following properties:

- Diameter: 600 ÷ 800 mm
- Maximum vertical bearing force: 2500 ÷ 4300 kN
- Maximum lateral displacement: ± 180 mm
- Equivalent viscous damping: 10%

The isolation system is placed just below the first floor slab, hardened by a grillage, on top of columns and walls. The main period of the isolated structure is about two s. Isolators were placed in order to minimize the distance between the mass centre and the rigidity centre of the structure, to reduce torsional effects on the structure during earthquakes.



Figure 2.8 - Gervasutta Hospital piers



Figure 2.9 - Gervasutta Hospital, isolation devices detail

2.4.2 Del Mare Hospital, Naples

Speaking about base isolated hospital, the *del Mare* Hospital, Naples, is one of the largest seismic isolated building in Europe. It has more than 500 beds, 15 operating rooms and 2 birthing rooms. The building is very irregular both in plant and in elevation,



Figure 2.10 - Del Mare Hospital, plane-volumetric view

The structure of the building is a 3D reinforced concrete frame, designed in accord to the OPCM 3431. The site characteristics are $a_g = 0.25g$ and ground type B, the importance coefficient is 1.4, and the structure coefficient q is equal to 1.5 for the superstructure. The first three vibrational period of the isolated structure are between 2.32 and 2.74 s, close to the target period of 2.5 s. According to the estimations, the isolation allowed to save about the 40% of the reinforcing steel that would have been used without isolation.

The isolation system consist of 327 isolators of three different typologies, with diameters in the range 600-800 mm, lateral stiffness 1.51-4.89 kN/mm and a primary shape factor always bigger than 24. The elastomeric cantilevers used are two, both with equivalent viscous damping equal to 15%, $G = 0.8$ MPa for 600 mm diameters isolator, and $G = 1.4$ MPa for the others. The design maximum displacement is 204 mm, including a reliability coefficient of 1.2 required by OPCM 3431, by analogy with EC8.



Figure 2.11 - Del Mare Hospital, installation of the isolators.

2.4.3 C.A.S.E. Project, L'Aquila

C.A.S.E. project, developed after the L'Aquila earthquake (04/06/2009), consisted in the construction of 185 apartments seismically isolated with Friction Pendulum System, whose first applications were implemented during the beginning of the 80s at Berkeley (CA, USA). FPS's working principle is based on the pendulum behaviour, and its purpose is to control the motion of the superstructure under horizontal motion.



Figure 2.12 - View of the residential complex C.A.S.E. project

The residences were built by the Italian government, under supervision of Civil Protection, over an area of 1700 m², including distribution and stairs. The structural concept is extremely simple: two 500 mm-thick reinforced concrete slabs separated by columns with uniform spacing of 6 m in both directions and isolators, of which one is supported by the ground and the others support the rest of superstructure (the apartments). While the bottom slab acts like a foundation, the top slab is the basement on which the entire superstructure is anchored, allowing a certain variety of architectural design.



Figure 2.13 - Base plate of C.A.S.E. project

The isolated prototype results to be made up, in short, by three elements: the first is the foundation substructure, which has to be rigidly connected to the ground; the seconds are the isolation devices, characterized by large lateral deformability and vertical rigidity, allowing the structure to behave normally under gravity load and to translate rigidly under horizontal loads such as seismic forces; the third is the superstructure, free to move in the plane of the structure according to the flexibility and the displacement capacity of the isolators.

Radius of curvature: 4 m

Equivalent viscous damping: 20%

Maximum lateral displacement: 260 mm

Maximum vertical load: 3000 kN



Figure 2.14 - C.A.S.E. Isolators -



Figure 2.15 - Installed isolator, C.A.S.E. project

2.5 Seismic isolation abroad

2.5.1 San Francisco City Hall



Figure 2.16 - San Francisco City Hall

The San Francisco City Hall in San Francisco, California, is a good example of retrofit of existing buildings. Constructed in 1915, after a strong earthquake destroyed the previous City Hall in 1906, it is listed in the National Register of Historic Places, being an outstanding example of classical architecture. The

structural scheme is a steel frame and concrete slabs with unreinforced brick masonry integral with the granite cladding, hollow clay tile infill walls, and limestone or marble panels lining many of the interior spaces.

During the 1989 Loma Prieta earthquake, centered about 95 km away, the building sustained substantial damage. The fixed-base fundamental period of vibration of the building was approximately 0.9 s. To improve the earthquake resistance of this structure, base isolation was adopted especially because it preserved the historic fabric of this building. In addition, the superstructure was strengthened by new shear walls within the building. The retrofit project was completed 9 years after, in 1998.

The isolation system consisted of 530 isolators, each a laminated rubber bearing with lead plugs, located at the base of each column and of the shear walls. The 53-cm-high bearings varied from 80 to 90 cm diameter. The column are supported on one or more isolators under a cruciform-shaped steel structure; multiple isolators were provided only for the heavily loaded columns. Installation of the isolators proved to be very complicated and required shoring up and cutting the columns while transferring their loads to temporary supports. The plane of isolation is just above the existing foundation. The isolation period is 2.5 s.



Figure 2.17 - Rubber bearings at the base of columns and shear walls

A major problem of this retrofit was to find a way to permit large motion of the isolated building: under a design earthquake with PGA of 0.4g, the isolated building is estimated to move 45 to 65 cm. A moat was constructed around the building to provide a minimum seismic gap of 70 cm. Flexible joints were provided for utilities, such as plumbing, electrical and telephone lines, crossing this moat space to accommodate movement across the isolation system.

2.5.2 Bolu Viaduct (Turkey)



Figure 2.18 - Bolu Viaduct (Turkey)

The following example of a retrofit procedure of a viaduct is taken from (Ghasemi, 2004).

The Düzce earthquake occurred on November 12, with a moment magnitude of 7.2, along the secondary Düzce fault, a branch of the North Anatolian Fault (NAF). According to seismologists, the rupture on November 12 resulted from the stress created by the Kocaeli earthquake, which occurred in the nearby on August 17. The epicenter of Düzce earthquake occurred very close to the Bolu Viaduct, a 2.3 km long elevated highway structure located on the last segment of Trans-European Motorway (TEM) which was under construction. The Bolu Viaduct, which utilized a hybrid isolation system, suffered extensive damage due to propagation of a surface fault rupture between segments of viaduct piers. At the Düzce station near the epicenter, a PGA of 1.0g was recorded before the ground motion instrumentation was clipped due to its limitation on recording acceleration above 1.0g. The instruments at Bolu, located 30 km east of the epicenter, registered a PGA of 0.8g. The Bolu Viaduct is located between these two stations, in the town of Kaynasli. As part of the retrofit it was necessary to replace both the damaged sliding pot-bearings and the damaged Energy Dissipation Units (EDU).

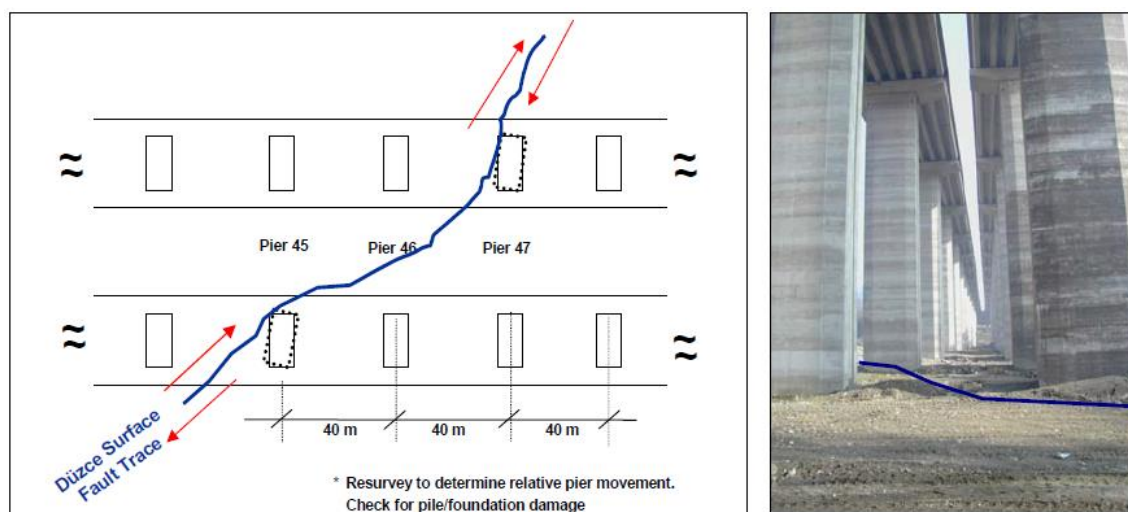


Figure 2.19 - Bridge scheme and fault direction

Seismic isolation of the superstructure from the piers was identified early on as essential for the repair/retrofit of the elevated highway. In addition, the use of seismic isolation technology assured that the piers of the Bolu Viaduct will remain elastic for future major earthquakes. As part of the retrofit design program, the original (1992) probabilistic seismic hazard studies for ground shaking and fault rupture were updated to include more recent data, particularly the two 1999 earthquakes. The Italian consultants (G.M. Calvi and Nigel Priestley) carried out the design of the repair and retrofit of the damaged elevated highway.

In consideration of all seismological studies, it was agreed with the Client (Turkish Government Karayollari Genel Mudurlugu) that the input ground motion should be characterized by the following properties:

- Design peak ground acceleration (PGA) 0.81g, which corresponds to a 2000-yr return period
- Design peak spectral acceleration (PSA) 1.8 – 2.0g at 5% damping
- Design peak spectral displacement (PSD) 600mm, resulting from a future fault rupture at the site
- Consideration of possible near-field effects

In addition to the demand arising from the ground motion, a permanent ground deformation resulting from ground creep and fault slip equal to $\pm 250\text{mm}$ was considered during the design life of the viaduct.

In the final design approach, two isolation bearings will be utilized at the internal support between the diaphragm and the pier cap and four isolation bearings at the expansion joints. In order to optimize the design and to consider the variation in the height of the piers and the crossing of the fault rupture at a specific location, three different Friction Pendulum isolation bearings are to be used. These are:

- Displacement capacity $\pm 700\text{mm}$, large radius (smaller height piers and abutments)
- Displacement capacity $\pm 700\text{mm}$, small radius (tall piers)
- Displacement capacity $\pm 900\text{mm}$, large radius (piers P40 to P50, where the fault rupture crossed during Duzce earthquake)

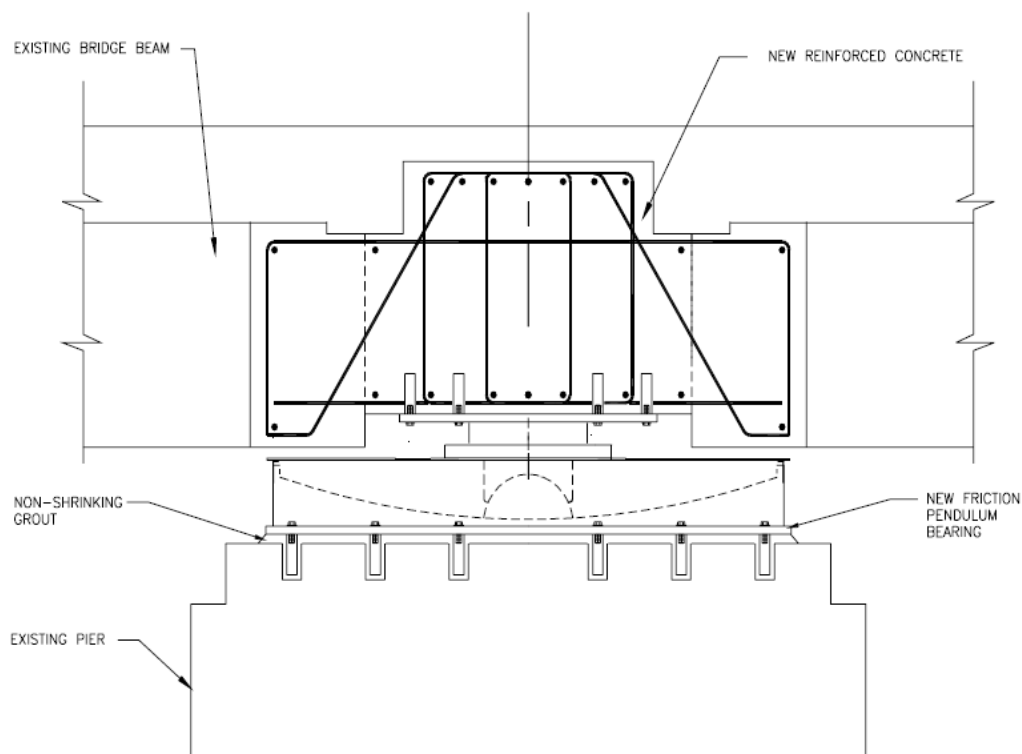


Figure 2.20 - Retrofit scheme at typical interior pier



Figure 2.21 - Friction Pendulum Isolation bearing

2.6 Elastomeric seismic devices

Nowadays, there is a very wide range in terms of details for base isolators, but the main principle is always to introduce a layer of low lateral stiffness between the superstructure and the foundation (buildings) or between the superstructure and the piers (bridges). This procedure modifies permanently the overall stiffness matrix: results of modal analysis show the presence of a new main vibrational period, which has to be much bigger than the fixed-base natural period. Deformation of the structure is then supposed to increase considerably, but the isolators will take the most of this displacement, while the structure remains practically undeformed. This happens regardless the properties of the system, which can be linear or non-linear, damped or undamped.

Elastomeric isolator are the most common in the isolation technique. They are composed of sheets of elastomeric material, of 5-20 mm thickness, alternated to steel plates of 2-3 mm thickness. The two different materials are bonded through vulcanisation process. These bearings need to be connected to the foundation and to the superstructure by mean of a couple of flanges.

Rubber can be either natural or synthetic:

- Natural rubber is chemically constituted by regular sequences of isoprene (C_5H_8), forming highly elastic chains. This is due to the few number of boundaries between the chains that stretch when subjected to tensile stresses, until they reach a failure point.

- Synthetic rubber are made of neoprene ($(C_5H_8Cl)_n$). This molecule does not differ too much in terms of mechanical properties, but it shows other advantages such as fire resistance, gas impermeability and an increased durability.

Damping capabilities of the rubber is anyway small; hence, its damping properties need to be increased, when required, by means of chemical processes.

2.6.1 Laminated rubber bearing

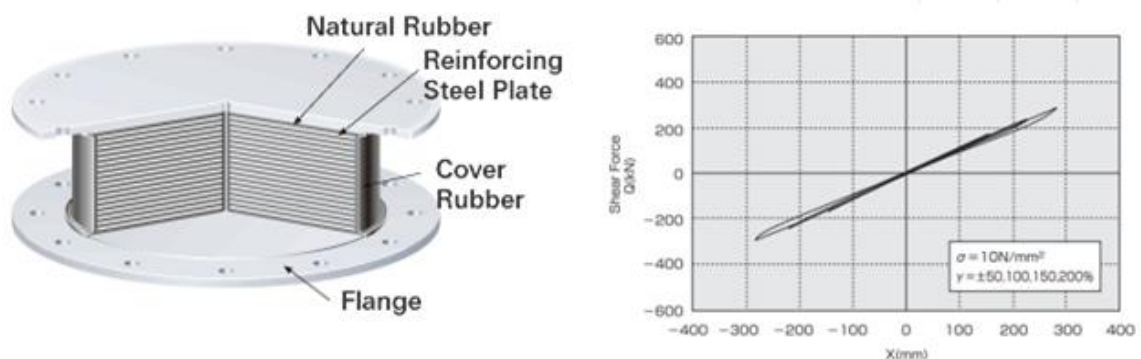


Figure 2.22 - Laminated rubber bearing (Bridgestone)

Natural rubber shows low damping parameters (the equivalent damping factor may be 2-3%), excellent linearity and stable restoring force characteristic. In the design phase, it is possible to choose between several values of the rubber elastic modulus and types of separate damping device, which is usually required. Due to the small values that the re-centering force assumes, these isolators may suffer for instability, as explained in (Kelly & Naeim, Design of Seismic Isolated Structures: from Theory to Practice, 1999).

2.6.2 High Damping Rubber Bearing (HDRB)

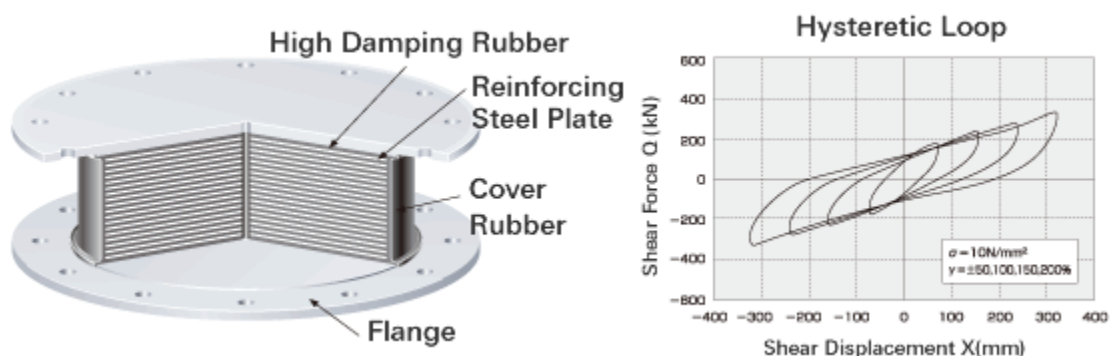


Figure 2.23 - Laminated high damping bearing (Bridgestone)

High damping rubbers may be used, so that a separated damping device is not required, and this may be very useful whereas small space for installation is usually a major constraint in design or in retrofit.

2.6.3 Lead Rubber Bearing (LRB)

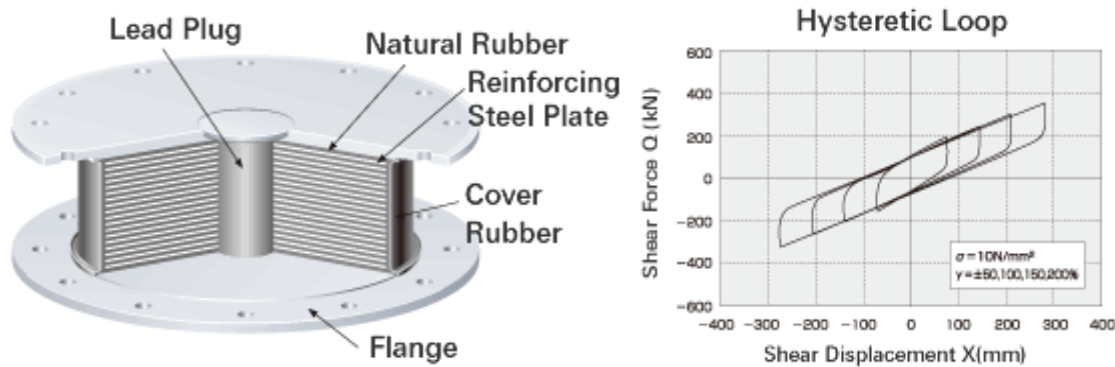


Figure 2.24 - Lead rubber bearing (Bridgestone)

Embedding a lead plug at the center of the laminated natural rubber gives to the bearing high damping capability. In fact, the lead plug is able to undergo plastic deformations and then to recover and recrystallize, showing absence of permanent damages. Hence, this type of bearing too does not need a separated damping device, and its hysteretic behaviour is similar to an elasto-plastic one (bi-linear). It is possible to vary the lead plug diameter in order to fine adjust the equivalent damping factor.

Isolation systems made up with LRB show:

- Higher initial stiffness, compared to the rubber bearing isolators, thanks to the lead plug. The LRB deformation under wind or thermal loads is usually negligible;
- High equivalent damping coefficient (even more than 30%);
- For the same performance of the rubber bearings, they are less expensive;

The force-displacement behaviour is still bi-linear, and it is given by the combination of the behaviours of the lead and the rubber, which show respectively linear elastic and elasto-plastic behaviour.

2.7 Sliding isolators

Isolation systems based on pure sliding are the simplest and oldest solution: they have been used by Greek, Chinese and Peruvian ancient civilizations. They can be

mono or multidirectional and are still in use, with new features but always following the same principles.

2.7.1 Plane sliding isolators: Friction Slider

They are bearing devices, multidirectional, with low friction sliding surface, usually made up by two circular or square plates of different diameters or sides, sliding one on the other. The materials used, steel and PTFE, can produce a small friction: the dynamic friction coefficient is between 5% and 20%, and if the surfaces are lubed it is reduced to 1-2%. In this last case, the forces exerted in horizontal direction are practically negligible: for this reason, these isolators are not a standalone device. They need, in fact, to be coupled with stiffening elements, dampers and centering devices.

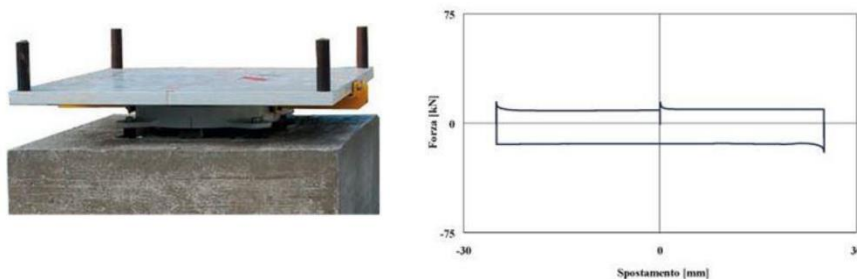


Figure 2.25 – Friction Slider (FIP Industriale)

2.7.2 Friction Pendulum System (FPS)

Friction Pendulum Systems are the main topic of this study. For this reason, the features of these devices will be defined in as much details as possible later in Chapter 3.2.

3 Dynamic of isolated systems

3.1 Linear theory of seismic isolation

The linear theory of seismic isolation has been theorized for the first time in (Kelly, Base Isolation: Linear Theory and Design, Vol. 6, No. 2, 1990), where the dynamic behaviour of base isolated structures is deduced by the results of the analysis of a simplified 2-dof model, which includes the isolation system and the superstructure.

In such a model, only lumped masses, linear spring and linear viscous damping are considered, so that linear modal analysis can be performed in order to identify the modifications introduced by the isolation in terms of vibration frequency and modal shapes. As explained in (Kelly, Base Isolation: Linear Theory and Design, Vol. 6, No. 2, 1990), most of the isolation systems are intrinsically non-linear, which implies that modal analysis gives only an approximation of the effective behaviour of the structure. Spring and damping parameters need then to be linearized, by using many techniques explained in the following.

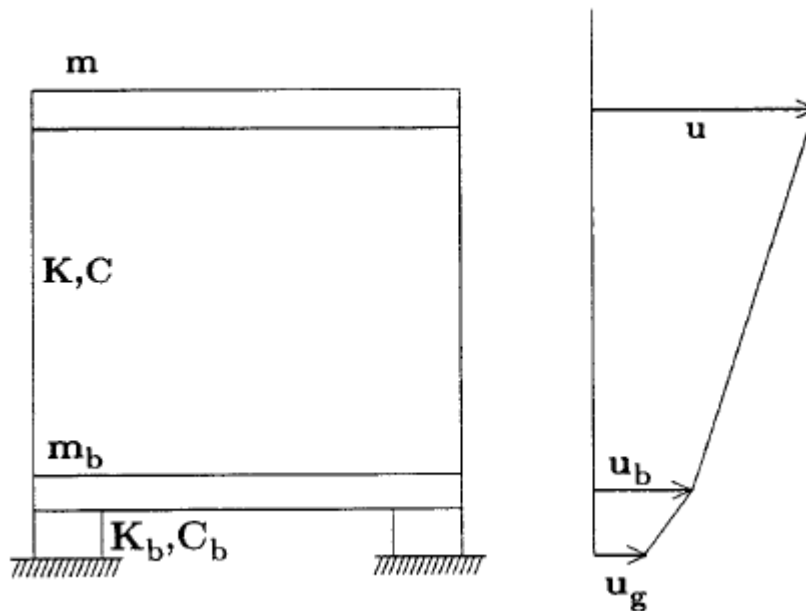


Figure 3.1 - Model of a single storey isolated structure

- m : superstructure mass;
- K, C : rigidity and damping of the superstructure;

- m_b : foundation plate mass;
- K_b, C_b : rigidity and damping of the isolation system;
- u : displacement of the superstructure respect to the ground;
- u_b : displacement of the isolation plane respect to the ground;
- u_g : ground motion, function of time.

The absolute equations of motion are:

$$m\ddot{u} = -c(\dot{u} - \dot{u}_b) - k(u - u_b) \quad (3.1)$$

$$m\ddot{u} + m_b\ddot{u}_b = -c_b(\dot{u}_b - \dot{u}_g) - k_b(u_b - u_g) \quad (3.2)$$

It is convenient to work with relative displacements:

$$v_s = u - u_b$$

$$v_b = u_b - u_g$$

in terms of which the equations of motion become:

$$m\ddot{v}_b + m\ddot{v}_s + c\dot{v}_s + kv_s = -m\ddot{u}_g \quad (3.3)$$

$$(m + m_b)\ddot{v}_b + m\ddot{v}_s + c_b\dot{v}_b + k_bv_b = -(m_b + m)\ddot{u}_g \quad (3.4)$$

This 2-dof system of equation can be solved directly or through modal decomposition. A modal analysis provides insight into the response of isolated systems and the results will be applicable to models that are more elaborate.

$$\begin{bmatrix} M & m \\ m & m \end{bmatrix} \begin{Bmatrix} \ddot{v}_b \\ \ddot{v}_s \end{Bmatrix} + \begin{bmatrix} c_b & 0 \\ 0 & c \end{bmatrix} \begin{Bmatrix} \dot{v}_b \\ \dot{v}_s \end{Bmatrix} + \begin{bmatrix} k_b & 0 \\ 0 & k \end{bmatrix} \begin{Bmatrix} v_b \\ v_s \end{Bmatrix} = \begin{bmatrix} M & m \\ m & m \end{bmatrix} \begin{Bmatrix} 1 \\ 0 \end{Bmatrix} \ddot{u}_g \quad (3.5)$$

$$[M]\{\ddot{v}\} + [C]\{\dot{v}\} + [K]\{v\} = -[M]\{r\}\ddot{u}_g$$

$$\omega_s = \sqrt{\frac{k}{m}} \gg \omega_b = \sqrt{\frac{k_b}{M}}, \quad \varepsilon = \left(\frac{\omega_b}{\omega_s}\right)^2$$

Assuming that ε has an order of magnitude of 10^{-2} , the superstructure is much more rigid than the isolation system, which usually occurs.

$$\xi_s = \frac{c}{2m\omega_s}, \quad \xi_b = \frac{c_b}{2m\omega_b}$$

$$\gamma = \frac{m}{m + m_b} = \frac{m}{M} < 1$$

It is possible to rewrite the system in mass-normalized form, dividing the first equation for M and the second for m , obtaining:

$$\ddot{v}_b + \gamma \ddot{v}_s + 2 \xi_b \omega_b \dot{v}_s + \omega_b^2 v_s = -\ddot{u}_g \quad (3.6)$$

$$\ddot{v}_b + \ddot{v}_s + 2 \xi_s \omega_s \dot{v}_s + \omega_s^2 v_s = -\ddot{u}_g \quad (3.7)$$

or, in matrix form:

$$\begin{bmatrix} 1 & \gamma \\ 1 & 1 \end{bmatrix} \begin{Bmatrix} \ddot{v}_b \\ \ddot{v}_s \end{Bmatrix} + \begin{bmatrix} 2 \xi_b \omega_b & 0 \\ 0 & 2 \xi_s \omega_s \end{bmatrix} \begin{Bmatrix} \dot{v}_b \\ \dot{v}_s \end{Bmatrix} + \begin{bmatrix} \omega_b^2 & 0 \\ 0 & \omega_s^2 \end{bmatrix} \begin{Bmatrix} v_b \\ v_s \end{Bmatrix} = -\begin{Bmatrix} 1 \\ 1 \end{Bmatrix} \ddot{u}_g$$

$$\frac{T_b}{T_s} = \Omega = \frac{1}{\varepsilon}$$

The characteristic equation for ω_n is:

$$(1 - \gamma)\omega_n^4 - (\omega_b^2 + \omega_s^2)\omega_n^2 + \omega_b^2\omega_s^2 = 0 \quad (3.8)$$

The exact roots are given by:

$$\begin{aligned} \omega_2^2 &\equiv \omega_s^{*2} = \frac{1}{2(1 - \gamma)} \left((\omega_s^2 - \omega_b^2) \pm \sqrt{(\omega_s^2 - \omega_b^2)^2 - 4(1 - \gamma)\omega_s^2\omega_b^2} \right) \\ \omega_1^2 &\equiv \omega_b^{*2} \end{aligned} \quad (3.9)$$

When we account for the fact that $\omega_b \ll \omega_s$ and rewrite the radical in the form

$$(\omega_s^2 - \omega_b^2)^2 \left(1 + 4\gamma \frac{\omega_s^2\omega_b^2}{\omega_s^2 - \omega_b^2} \right) \quad (3.10)$$

and expand this by binomial series, we obtain:

$$\begin{aligned} \omega_1^2 &\equiv \omega_b^{*2} = \omega_b^2(1 - \gamma\varepsilon) \\ \omega_2^2 &\equiv \omega_s^{*2} = \frac{\omega_s^2}{1 - \gamma} (1 + \gamma\varepsilon) \end{aligned} \quad (3.11a,b)$$

In many cases, it may be sufficiently accurate to take as approximations for ω_b^* , ω_s^* the first terms:

$$\omega_b^* = \omega_b \quad (3.12a,b)$$

$$\omega_s^* = \frac{\omega_b}{\sqrt{1-\gamma}}$$

This indicates that the isolation frequency variation due to structure flexibility is practically negligible, while the structural frequency is significantly increased by the addition of the base mass. The difference between the isolation period and the fixed-base structural period increases once the isolation and the structure are combined.

$$\begin{aligned} \underline{\phi}_1^T &= \{1, \varepsilon\} \\ \underline{\phi}_2^T &= \left\{1, -\frac{1 - (1 - \gamma)\varepsilon}{\gamma}\right\} \end{aligned} \quad (3.13a,b)$$

The first mode shape is approximately a rigid structure mode, whereas the second involves both structural deformation and isolation system deformations. They are sketched in FIGURE

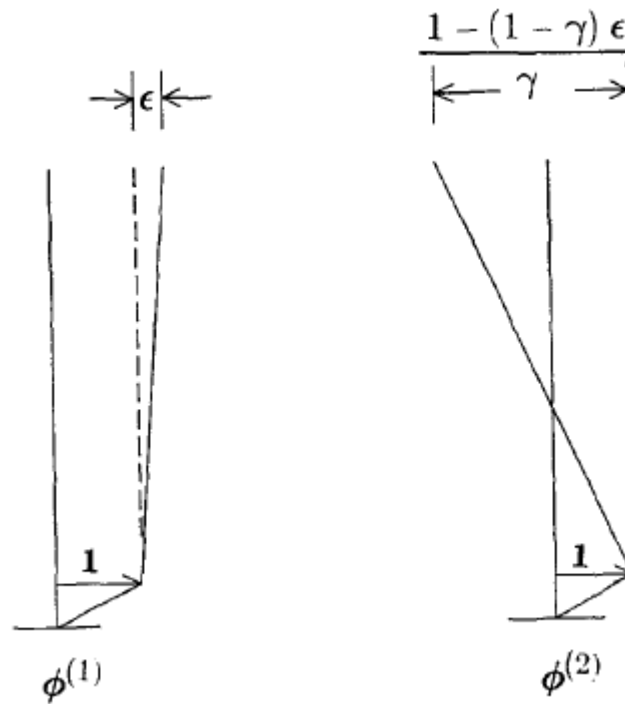


Figure 3.2 - Modal shapes

It is now possible to calculate the displacement of the base and of the superstructure by combining linearly the two mode shapes.

$$v_b = q_1 \phi_b^1 + q_2 \phi_b^2 \quad (3.14a,b)$$

$$v_s = q_1 \phi_s^1 + q_2 \phi_s^2$$

$$\ddot{q}_1 + 2\omega_b^* \xi_b^* \dot{q}_1 + \omega_b^{*2} q_1 = -L_1 \ddot{u}_g$$

$$\ddot{q}_2 + 2\omega_s^* \xi_s^* \dot{q}_2 + \omega_s^{*2} q_2 = -L_2 \ddot{u}_g$$
(3.15a,b)

The mass participation factors are:

$$L_1 = 1 - \gamma \varepsilon$$

$$L_2 = \gamma \varepsilon$$
(3.16a,b)

It is obvious then, that the more the ratio between the isolation period and the structural period is large, the less will be the importance of the second mode shape.

The energy dissipation provided by the isolation system is certainly of primary importance, and in the model described so far is exerted by the viscous damping, proportional to the viscous coefficients c_b and c_s through the velocities \dot{v}_b and \dot{v}_s . By using the FORMULAS it is possible to assess the viscous damping ratios on both modal shapes:

$$\xi_b^* = \xi_b \left(1 - \frac{3}{2} \gamma \varepsilon \right)$$

$$\xi_s^* = \frac{\xi_s}{\sqrt{1 - \gamma}} + \frac{\gamma \xi_b \sqrt{\varepsilon}}{\sqrt{1 - \gamma}}$$
(3.17a,b)

As it can be observed, the structural damping increases because of the presence of damping in the isolation system. This increase is of the order of magnitude of $\sqrt{\varepsilon}$. The factor $\xi_b \sqrt{\varepsilon}$ may yield to a significant increment of ξ_s^* if ξ_s has a small value. In this respect, it has to be highlighted that structural damping is usually about 2-3%, while isolation system damping is usually between 10-30%.

It has to be remarked that a linear analysis of base isolated structures does not take into account the real behaviour of the isolation devices. Many devices show in fact a highly non-linear behaviour, and this implies that if we want to obtain a closed form solution, it is necessary to use a linearization technique proposed in literature.

FPS (Friction Pendulum System) is, by all effect, a non-linear isolation devices because of the presence of the friction as an energy dissipation mechanism, and,

as it will be explained later, the fact that friction coefficient itself depends from the relative velocity between the slider and the sliding surface. This assumes even more importance in the case of DCFP (Double Concave Friction Pendulum), because of the fact that curvature radii and friction coefficient of two FPSs combined in series are not necessarily the same. Other reasons of non-linear behaviour, such as temperature and compressive tension acting on isolators, will be discussed later in the next paragraph.

3.2 Friction Pendulum System

The purpose of this paragraph is to show the basic knowledge necessary to understand the behaviour of a structure isolated with FPS. To do that, it is necessary to remind the physical behaviour of the pendulum in order to understand how it lengthen the isolated structure period (Zayas, Low, & Mahin, 1990).

FPS is an isolator device that provides an increase of the isolated structure's natural period, which becomes independent of the mass of the superstructure. It also offers the possibility to dissipate the energy transmitted through the isolator itself thanks to the friction between the articulated sliding surface and the composite material on the slider.

It is constituted by a concave spherical surface, on which a pivot can move when the superstructure is subjected to horizontal forces. The curvature of the surface provides the restoring force and the friction between the pivot and the surface itself dissipates part of the seismic energy transmitted.

Uncoupling of the structure from the ground motion is possible thanks to an articulated slider able to slide on a spherical surface, which can be united to either the substructure or the superstructure.

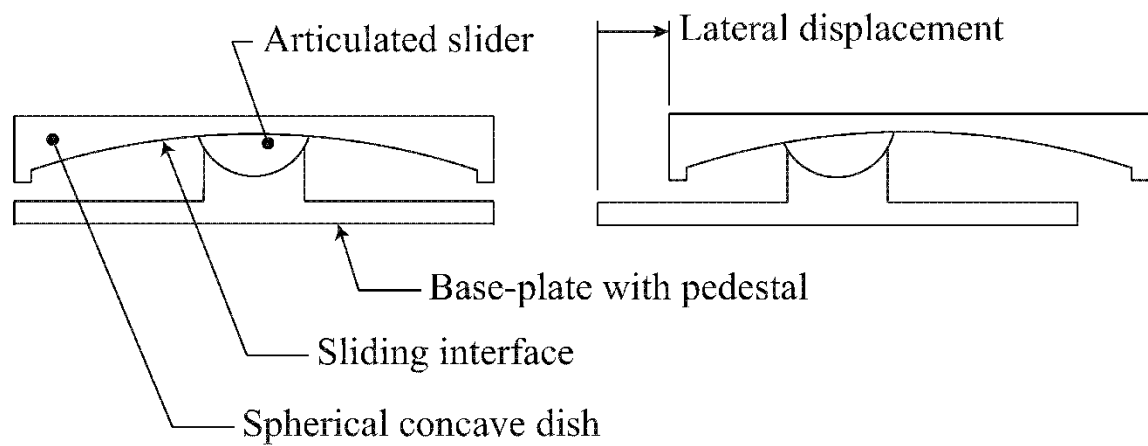


Figure 3.3 - Friction Pendulum System behaviour

The physical behaviour of the FPS depends from the mechanical and geometric properties of the slider and of the surface. These properties determines the energy dissipation capability through friction, the resistance to horizontal actions and the restoring elastic force necessary to bring the structure back to his undeformed shape once the lateral action is over. Essentially, the curvature radius of the spherical surface and the friction between the articulated slider and the sliding surface are sufficient to determine the basic behaviour of the isolator, but it has to be remarked that sometimes they might be in contrast. For example, a high friction coefficient may cause a permanent deformation of the isolator at the end of a seismic action if the curvature radius is not enough small to provide a restoring force that can overcome the frictional force and re-centre the slider.

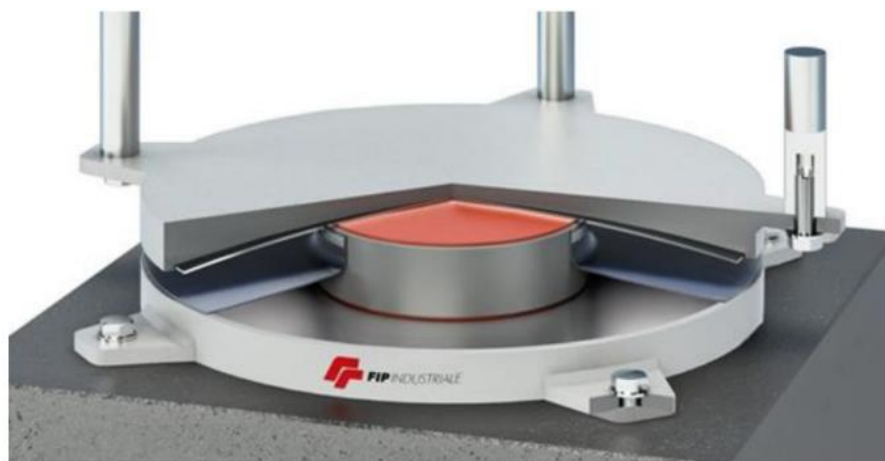


Figure 3.4 - FPS isolator (FIP Industriale)

At the state of the art, sliding surfaces of FPS are made coupling a metallic surface in stainless or chromate steel and a non-lubed plastic material, usually Polytetrafluoroethylene (PTFE), a synthetic fluoropolymer, or its composites. This

results in a friction coefficient between 0.03 and 0.12. The friction between steel and PTFE has been subject of several studies during the years by (Mohka, Constantinou, & Reinhorn, Teflon Bearings in Base Isolation I: Testing, 1990) (Mohka, Constantinou, & Reinhorn, Teflon Bearings in Base Isolation II: Modeling, 1990).

These studies demonstrated that it is incorrect to assume that the steel-PTFE friction has a Coulomb friction force-displacement law (which means that friction coefficient remain constant during relative sliding between surfaces).

3.2.1 Dynamic behaviour

The motion of the slider on the surface of the FPS can be described by the equation of motion for a pendulum, introducing a friction force:

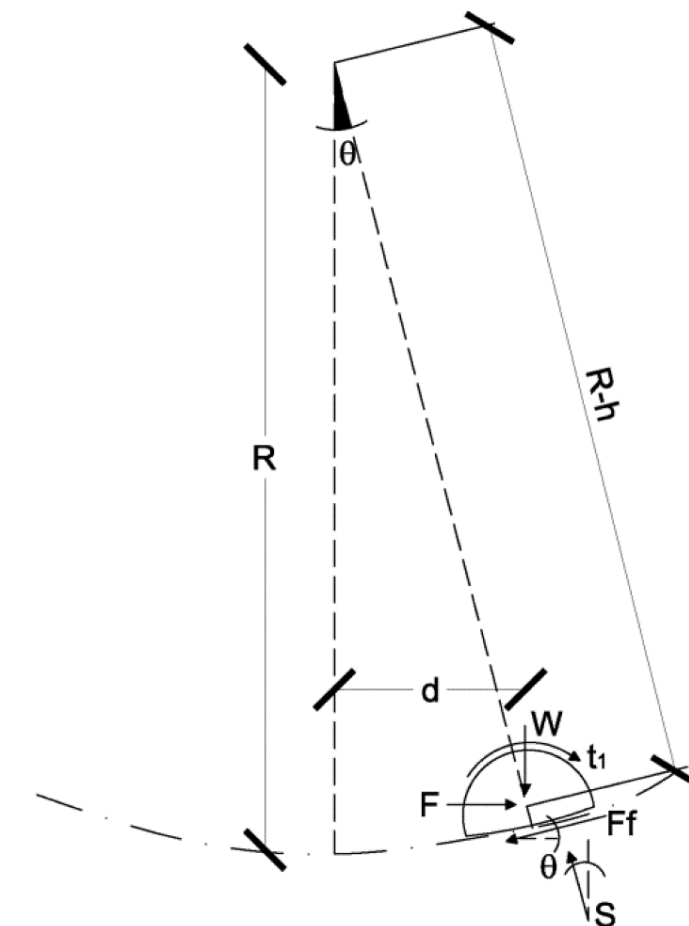


Figure 3.5 – Pendulum behaviour

The symbols in Figure 3.5 represents:

- W is the vertical load acting on the pendulum;

- F is the lateral force acting on the slider;
- $F_f = \mu W$ is the friction force, which is always tangential to the spherical surface;
- S is the contact force, which is always normal to the spherical surface;
- t_1 tensile forces, acting along slider surface, are considered included in the friction force F_f , and so they do not explicitly appear in the equilibrium equation;
- R is the curvature radius of the spherical surface;
- d is the horizontal distance of the slider centre from the centre of the concave surface;
- h is the distance between the surface and the pivot of the slider, which is usually neglected; it may be important only for construction reasons;

It is now possible to write the equilibrium equations in both vertical and horizontal direction:

$$\begin{cases} f_b - S \sin \vartheta - F_f \cos \vartheta = 0 \\ W - S \cos \vartheta + F_f \sin \vartheta = 0 \end{cases} \quad (3.18)$$

Combining the equations, it is possible to isolate the value of the restoring force:

$$f_b = W \tan \vartheta + \frac{F_a}{\cos \vartheta} \quad (3.19)$$

Under the hypothesis of small displacement, it is possible to assume that:

$$\sin \vartheta = \frac{u}{R}, \quad \cos \vartheta = 1, \quad \tan \vartheta = \frac{1}{R}$$

Substituting the trigonometric terms in Equation (3.19), we obtain:

$$F = \frac{W}{R} d + F_f \quad (3.20a)$$

The force-displacement behaviour is then bi-linear, and it is possible to express it as it follows:

$$F = \frac{Mg}{R} u + mgf \operatorname{sgn}(\dot{u}) \quad (3.20b)$$

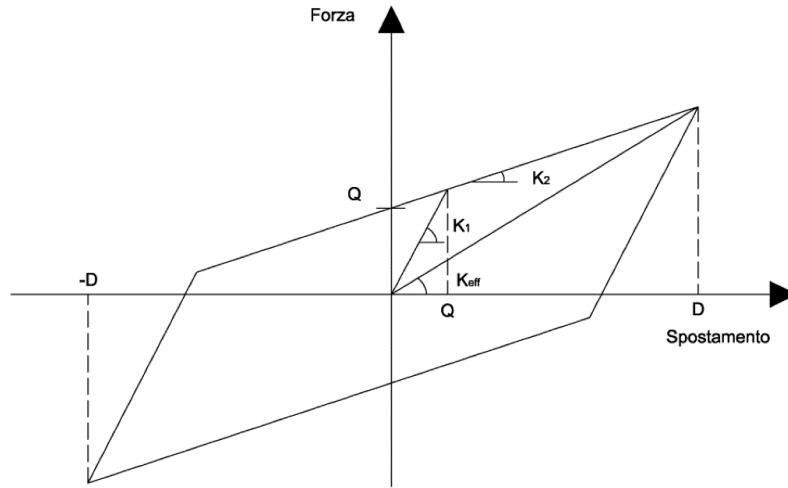


Figure 3.6 - FPS's bi-linear behaviour.

The first term of the previous equation is the secondary stiffness K_2 , and is the lateral stiffness that provides the restoring force:

$$K_2 = \frac{Mg}{R} \quad (3.21)$$

The main period of the isolator is, as expected, independent on the superstructure mass M :

$$T = 2\pi \sqrt{\frac{K_2}{M}} = 2\pi \sqrt{\frac{R}{g}} \quad (3.22)$$

At first, the systems does not react with the initial stiffness K_1 , which is ideally infinite until the bounds due to friction are overcome, i.e. when the sliding starts. This may be simulated numerically by using a very high value of stiffness: for example, $K_1 = 51K_2$ has been proposed in (Kelly & Naeim, Design of Seismic Isolated Structures: from Theory to Practice, 1999). Until the first sliding occurs, superstructure and substructure are rigidly connected and the overall behaviour is the one of a fixed-base structure. Once the external forces overcome the friction force, the motion starts and the actual stiffness become K_2 .

In Figure 3.7 is showed the hysteretic behaviour of an FPS isolator. Vertical axis indicates the total force, i.e. the sum of the elastic force and friction force, and the horizontal axis indicates the lateral deformation of the FPS. During the first phase, usually called sticking phase, the system acts as a body rigidly connected to the ground. Once the maximum friction force is overcome, the lateral stiffness drops

to K_2 . When there is a motion inversion, the friction coefficient drops immediately to zero, and so does the frictional force, to restart the motion in the opposite direction once the lateral force reach the maximum frictional force. The length of the vertical line segment in correspondence of motion inversion is two time the characteristic force Q , which is the maximum value of the frictional force.

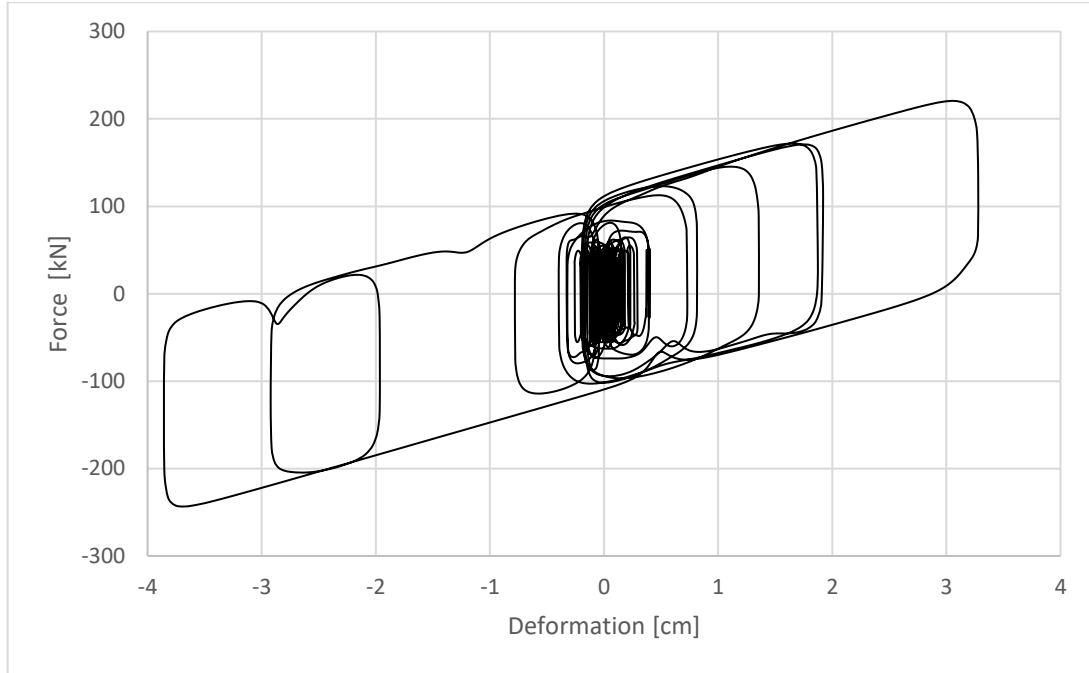


Figure 3.7 - Hysteretic behaviour of a FPS.

It is possible to calculate the domain of the stable equilibrium condition:

$$F_f \geq F_e \rightarrow d \leq \mu R \quad (3.23)$$

Which means that for lateral displacements smaller than μR the system will not be able to re-center itself. If materials with low friction coefficients such as PTFE are used, residual deformation of the isolators are small or negligible. Using materials with high friction coefficient would mean to have large and unacceptable residual deformation and, in this situation, it is necessary to restore the undeformed condition with external forces.

3.3 Friction

Friction is a dissipative force due to tangential stresses that two body exchange through their areas of contact when external forces attempt to make them slide.

In this chapter, we will focus on the mechanisms that govern the friction behaviour, as results of the experimental analyses conducted on devices with

PTFE-steel interfaces. As a general result, the friction coefficient is correlated to the relative sliding velocity and the apparent pressure.

The investigations have been carried out in conditions of both high and low relative sliding velocity.

What follows is based on the studies of (Bowden & Tabor, 1950, 1964, 1973).

3.3.1 Adhesion

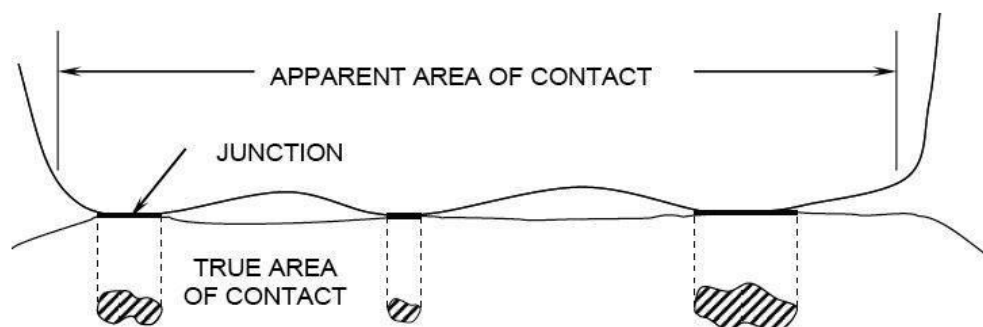


Figure 3.8 - View of a junction, apparent and true area of contact.

The adhesion is the tendency of dissimilar surfaces to cling to one another, by means of atomic bonds through small contact areas. These areas are called *junctions*, and their sum constitute the *true area of contact*, which is always considerably smaller than the *apparent area of contact*. Adhesion mechanism is dominant for clean and smooth sliding surface interfaces.

Junctions are characterized by interface forces of adhesion due to the existence of steel-carbon chemical bond between steel and PTFE. Friction force is then expressed by the product of true area of contact by the shear strength of the bounds:

$$F_a = s A_r \quad (3.24)$$

3.3.2 Plowing

Every surface has a certain roughness, which undergoes elastic or plastic deformations during relative sliding between surfaces. The dissipation of energy due to these deformations is the plowing component of the friction during surface relative sliding. This phenomenon may be understood easily considering a spherical and hard asperity laying on a soft and plane surface. If an axial load is applied on the asperity, this one sticks to the underlying surface and in the

meantime creates a junction. If a shear action is then introduced, the asperity moves horizontally, dragging with itself part of the softer underlying material and creating a furrow along the travelled path. Considering a multitude of asperities, the effect that they have on a softer material during dragging (the PTFE for FPS) constitutes the plowing component of the friction.

3.3.3 Visco-elastic effects

Most of the polymeric materials used for sliding surface of FPS, such as PTFE, show a visco-elastic behaviour. When there is relative sliding between a hard material and a visco-elastic one, the latter dissipates energy undergoing cyclic deformations.

3.3.4 Stick-slip phenomenon

Stick-slip phenomenon is a succession of block and sliding phases, which usually occurs in many ordinary events and responsible of noises such as squeak of the doors, screech of the chalk on a blackboard, the sound of a violin, etc. It is typical of lubed mechanisms and is due to a couple of causes:

- the dynamic friction coefficient is lower than the static one;
- during the static phase, the system can store elastic energy.

The nature of the phenomenon consists in the sudden release of the energy stored when the dynamic phase begins, and this happens because of the tangential stresses applied during relative surface sliding. This behaviour is typical of elastic mechanical systems containing friction and may take place only in presence of a natural variation of the friction coefficient.

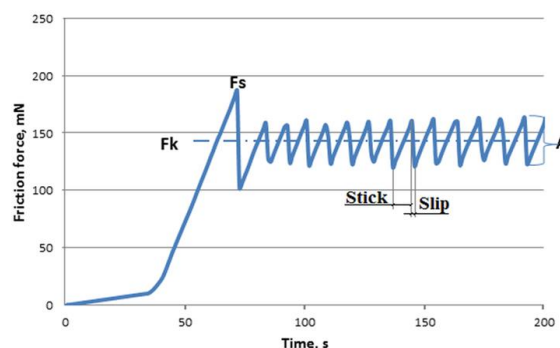


Figure 3.9 - Stick-slip phenomenon.

It is of vital importance to define the properties of the frictional behaviour while relative sliding between surfaces occurs. It is necessary to remark the difference between the many possible dynamic friction coefficients:

- μ_{din} is the coefficient that we have during sliding. It is reached by average velocities comparable to the design ones of FPS: they are about $160 \div 400$ mm/s, considering that typical values of displacements and frequency of an isolated structure are respectively $100 \div 200$ mm and $0.4 \div 0.5$ Hz;
- μ_s is the coefficient that we have immediately before the beginning of the dynamic phase of oscillation;
- μ_{inv} is the coefficient that we have right when the sliding changes its direction, and assumes values between the previously cited ones.

A large series of experimental investigations allowed formulating a series of analytical expressions that highlights the dependency of the dynamic friction coefficient from the sliding velocity besides temperature and apparent pressure.

3.3.5 Modeling of the friction-velocity behavior

Many investigations were carried out on the effective behaviour of the isolation devices to understand how it is affected by the variability of the friction in dynamic conditions.

The dynamic friction coefficient assumes a small value soon after that the sliding occurs, f_{min} , and increases progressively with the sliding velocity. For high sliding velocity, it assumes a constant value, f_{max} . Furthermore, increasing the normal load will lead to a reduction of friction coefficient (Mokha et al., 1990), until a constant value is reached for a limit value of the load. The rate of reduction is practically constant: doubling the contact pressure (from 9.36 to 18.7 MPa) there is a variation of the friction coefficient of 25% at -10°C , up to 33.4% at 50°C (Constantinou, Whittaker, Kalpakidis, Fenz, & Warn, 2007).

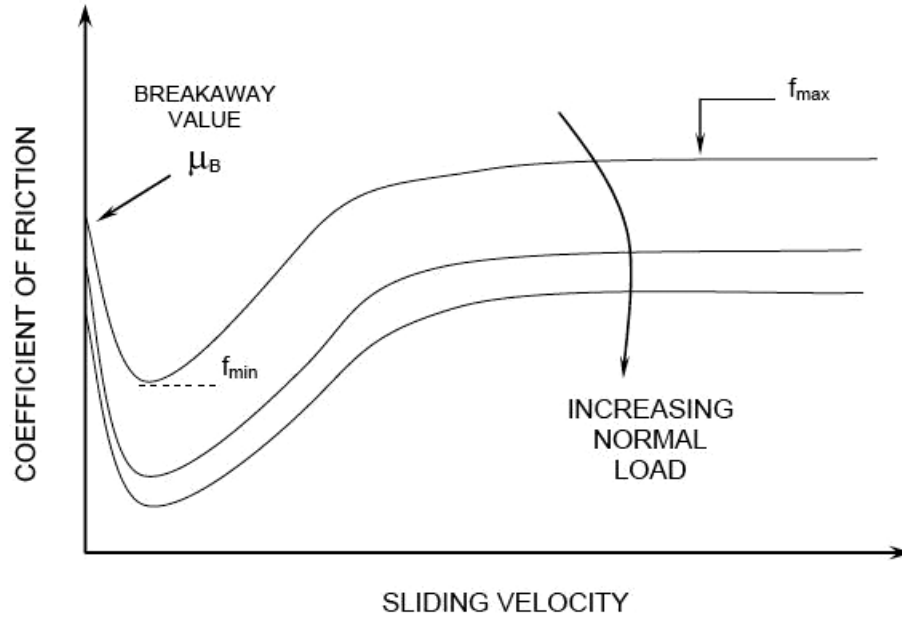


Figure 3.10 - Dependency of friction coefficient from sliding velocity and pressure

The high value of the static friction coefficient, μ_B , is due to adhesion.

When the sliding begins, a crystalline and oriented film of PTFE, of the thickness of the order of 10^{-8} m settles on the stainless steel surface, reducing drastically the friction coefficient from μ_B to f_{min} because of the low shear strength of this material. Increasing sliding velocity, friction coefficient increases too until it reaches a maximum value of f_{max} . The difference between maximum and minimum value of dynamic friction coefficient is as bigger as the contact pressure is smaller, with values next to 12% at a pressure of 9.36 MPa e smaller of 7% at 28.1 MPa. On the other hand, temperature has a small influence on this difference. Generally, for a fixed value of apparent contact pressure, the sliding friction coefficient depends on velocity, as explained by (Mohka, Constantinou, Reinhorn, 1990) and made explicit by the following formula:

$$f(\dot{x}) = f_{max} - (f_{max} - f_{min})e^{-\alpha|\dot{x}|} \quad (3.25)$$

where:

- f_{max} is the maximum sliding friction coefficient at high sliding velocity (200÷800 mm/s);
- f_{min} is the minimum sliding friction coefficient at essentially zero sliding velocity;
- \dot{x} is the sliding velocity;

- α is a parameter that controls the variation of sliding velocity coefficient. More precisely, it is the inverse of the characteristic sliding velocity, and it has typical values of 20-30 m/s for PTFE-steel interfaces.

Figure 3.11 shows friction-velocity law based on this formula, which describes properly experimental results previously cited and A sliding velocity greater than 150 mm/s is enough to reach the maximum value of dynamic friction coefficient of all the PTFE-base materials at standard temperatures.

To sum up:

- Friction coefficient increases quickly with sliding velocity until it reaches a value, after which it remains constant. This value is about 150 mm/s, regardless of the temperature and of the pressure on the sliding surface.
- Friction coefficient for devices with PTFE-steel interface reduces with increasing normal loads. The reduction rate depends on the sliding velocity and on temperature, the maximum variation is of 30% for variation of $\pm 50\%$ of the contact pressure (for $t=20^\circ\text{C}$, $p=18.7\text{ MPa}$, $v \geq 150\text{ mm/s}$), regardless of lubrication.
- The difference between the maximum and the minimum value of the friction coefficient is as larger as smaller is the acting vertical pressure.

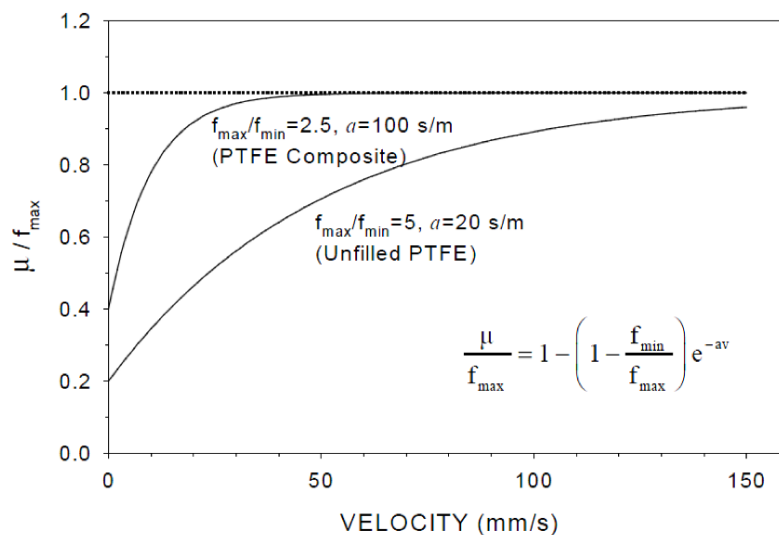


Figure 3.11 – Friction vs sliding velocity diagram

3.3.6 Effect of load permanence and travelled path

It has been observed in (Mohka, Constantinou, & Reinhorn, Teflon Bearings in Base Isolation I: Testing, 1990) that static friction coefficient is practically the

same regardless of the duration of the application of the load. More specifically, there are no significant difference for loads applied for 30 minutes and for 594 days. Many other tests were conducted and everyone demonstrated that the fluctuations in the friction coefficient cannot not be attributed to the duration of the load. Instead, it has been observed that surfaces subjected to previous load cycles showed a static friction coefficient considerably smaller after a first load cycle, confirming the existence of a PTFE film that settles on the steel surfaces after a first cycle.

Generally, the dynamic friction coefficient at high sliding velocity, f_{max} , diminish when the travelled path increases, going from an initial value of 12.5% to 10% right after 40 m of travelled path; once a threshold of about 300 m is reached, it shows a new increase. The dynamic friction coefficient at high sliding velocity, f_{min} , shows fluctuations in the range 0-40 m.

Friction coefficient tends to diminish during load cycle at high velocity, due to PTFE visco-elastic properties. This reduction is estimated to be of the order of 25-30%.

3.3.7 Effect of normal load variation over seismic behaviour of device

FPS isolators are intended as vertical bearing devices, and they have only compressive strength. This has to be taken into account during the design phase: tensile axial loads cannot be bear by the device, which would result damaged at the sliding interface; also, the articulation may get off its case. Assuming that the device is subjected only to compressive forces is a necessary condition to perform an analysis of whichever structure implementing FPS, even more so in case of linear analysis.

While the isolation period T depends only on the curvature radius chosen for the spherical surface of the device, where the relative sliding between surfaces takes place, the equivalent period and the horizontal force developed by the isolation system are function of the axial load N acting on the devices. Equivalent period and shear are both subjected to the continuous variation of N , implying that they cause irregularity in the force-displacement behaviour of isolators.

3.4 Modelling criteria

There are two different parameters that can describe the period of the isolators, depending of which stiffness parameters is considered. If the stiffness considered is K_2 , the period T is the one calculated with the FORMULA. If we refer instead to the secant stiffness K_{eff} , defined as the ratio between the maximum lateral force in correspondence of the maximum lateral displacement and the maximum lateral displacement itself.

$$K_{eff} = \left(\frac{1}{R} + \frac{\mu}{d} \right) W \quad (3.26)$$

With this formula, it is possible to calculate the effective period:

$$T_{eff} = 2\pi \sqrt{\frac{M}{K_{eff}}} = 2\pi \sqrt{\frac{M}{\left(\frac{1}{R} + \frac{\mu}{d} \right) Mg}} = 2\pi \sqrt{\frac{Rd}{(R + \mu d)g}} \quad (3.27)$$

Each time the system may be described by an equivalent linear model, the effective period differs from the tangent period of no more than 14%. This means that the deviation from the non-linear model is practically insignificant also in terms of dynamic behaviour. In absence of necessary requirements for the use of an equivalent linear model, the NTC08 prescribes to use a non-linear analysis to evaluate the dynamic response, since it allows identifying the difference of the phenomena associated to the transition from states characterized by different stiffness.

Another important parameter that defines the friction isolator behaviour is the equivalent viscous damping coefficient, which allows calculating the energy dissipated by the friction with the following formula:

$$\xi_{eff} = \frac{\text{hysteresis cycle area}}{4\pi K_{eff} d^2} \quad (3.28)$$

This formula allows linearizing a system that dissipates energy through friction by calculating an equivalent viscous damping coefficient that dissipates the same amount of energy when the system undergoes the same displacement history. Considering that the hysteresis cycle area is equal to $4\mu Wd$ and the previously written formula for K_{eff} , we obtain:

$$\xi_{eff} = \frac{4\mu W d}{4\pi \left(\frac{1}{R} + \frac{\mu}{d}\right) W d^2} = \frac{2\mu}{\pi \left(\frac{d}{R} + \mu\right)} \quad (3.29)$$

which clearly shows how the equivalent damping is a function of the friction coefficient, of the curvature radius and of the displacement demand; the latter may be considered as a design input for the displacement at an arbitrary limit state condition. It follows that the equivalent dissipation to be adopted in a linear analysis is function on the considered limit state, and assumes different values depending on the displacement demand of the system. Generally, the usual value is referred to the SLV, used for verification of isolated structure.

To design devices respect to the system fragility in regard of failure mechanism related to the overpassing of the ultimate displacement capacity, it has to be considered the displacement demand at collapse conditions (SLC).

3.4.1 Linear modelling

Modelling the isolation system as a linear spring, characterized by a spring rigidity and by an equivalent viscous damping, represents an obvious simplification in the first steps of the design phase, and, as of that, may be applied only under specifics conditions:

- the equivalent rigidity of the isolation system must be at least the 50% of the secant value for cycles with deformation of the 20% of the ideal displacement. For pendulum devices, the cited limitation become:

$$\frac{R}{d_{ac}} \leq \frac{1}{3\mu_{din}} \quad (3.30)$$

where d_{ac} is the rigidity centre of the isolation system at the considered limit state, R the curvature radius and μ_{din} the dynamic friction coefficient of the device;

- equivalent linear damping of the isolation system must be smaller than 30%;
- force-displacement behaviour of the isolation system must not be subjected to variation bigger than 10% due to effect of deforming velocity variation or vertical load applied to the devices;

- the increase of the force in the isolation system for displacement between $0.5 d_{dc}$ and d_{dc} must be at least the 2.5% of the total weight W of the superstructure. This request implies the use of a curvature radius of at maximum 20 times the design maximum displacement.

3.4.2 Non-linear modelling

Even if the vertical acceleration component is not considered, it must be verified that the variation of axial load acting on the isolation devices due to the opposition to overturning induced by horizontal seismic forces is less than the 10% of the value in quasi-permanent condition. Otherwise, it is mandatory to perform a non-linear analysis, adopting a proper force-displacement behaviour and proceeding with a time-step integration of the motion equations.

3.5 DCFP

A DCFP is made up by two spherical sliding surfaces, between which it is interposed a slider. This device allows to reduce the in-plane dimensions and the eccentricity given by the horizontal displacement of the structure.

A double concave friction pendulum (DCFP) system consists of two sliding surfaces and may be modelled as a couple of friction pendulum systems (FPSs) in series. Knowing that the force-displacement behavior of the FPS is bi-linear, the DCFP's may be either bi-linear or tri-linear. While in the first case the DCFP is practically equivalent to a single FPS, and so friction coefficients and radii of curvature of both the surfaces must be equals, in the tri-linear case several combinations of the two parameters may be used to obtain various force-displacement behaviors.

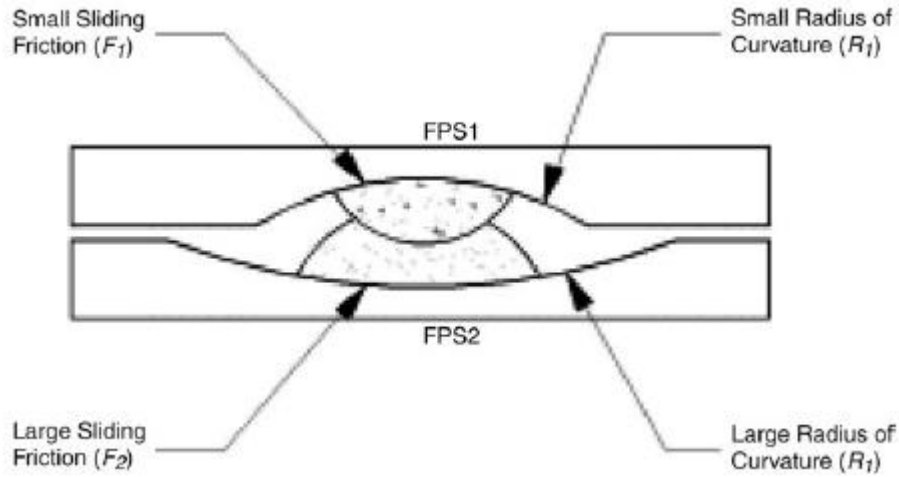


Figure 3.12 - DCFP conceptual sketch

Owing to the serial nature and neglecting the inertia effect of the small mass of the slider, the reaction forces at two FPSs become identical, from which the reaction force of the DCFP can readily be obtained (Constantinou M. C., Friction Pendulum Double Concave Bearing, 2004) (Constantinou & Fenz, Behaviour of the double concave friction pendulum bearing, 2006):

$$F = F_1 = F_2 = \frac{mgu}{R_1 + R_2} + \frac{mg(R_1 f_1 \text{sgn}(\dot{u}_1) + R_2 f_2 \text{sgn}(\dot{u}_2))}{R_1 + R_2} \quad (3.31)$$

The first part of the right hand side of (3.31) is related to the restoring stiffness (K_{comb}) of the combined DCFP, from which the restoring natural period (T_{comb}) of the DCFP can be obtained as:

$$K_{comb} = \frac{mg}{R_1 + R_2} \quad (3.32)$$

$$T_{comb} = \sqrt{T_1^2 + T_2^2} = 2\pi \sqrt{\frac{R_1 + R_2}{g}} \quad (3.33)$$

On the other hand, the second part of the right hand side of (3.31) represents the combined friction force, from which the equivalent friction coefficient of the DCFP can be derived as:

$$f_{eqv} = \frac{f_1 R_1 + f_2 R_2}{R_1 + R_2} \quad (3.34)$$

where two FPSs are assumed to move in the same direction.

A tri-linear DCFP consisting of two different FPSs shows bi-linear behavior under small ground motion, while it shows tri-linear behavior under large ground motion, as explained in (Kim & Yun, 2007). This happens because, as it is shown in Figure 3.13, small ground motion does not cause forces large enough to activate the motion on the surface with the higher friction coefficient; hence, the push-over curve does not go beyond the bi-linear part. For bridges instead, it is obvious that the intensity of the motion must not be evaluated at the ground level, but at the bearing support level, since it may be considerably different from ground motion, depending on pier main vibrational period.

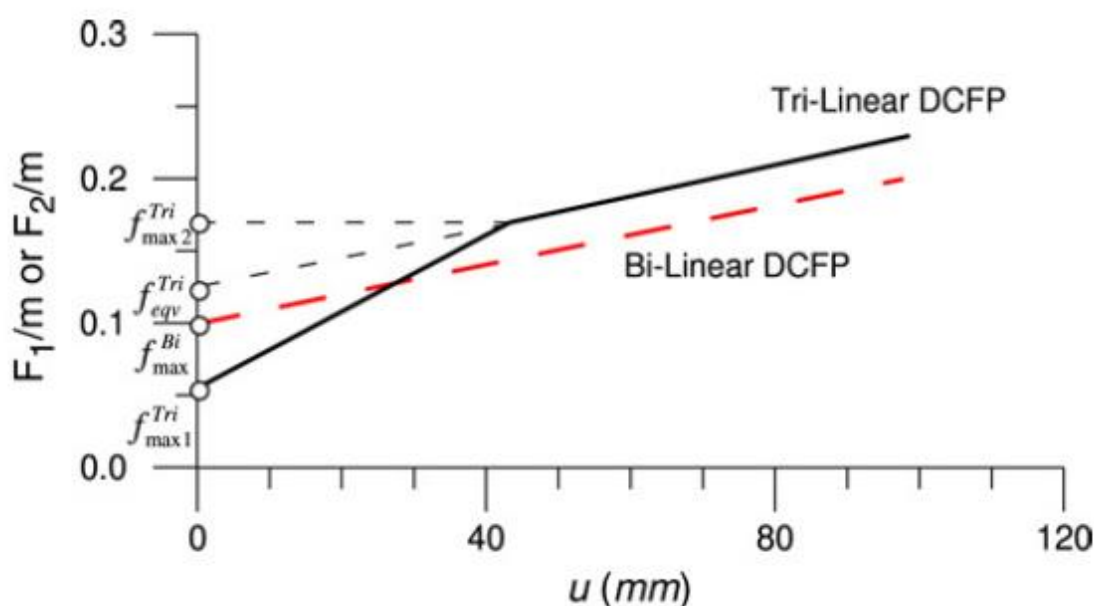


Figure 3.13 - Push-over curves for tri-linear and bi-linear DCFPs

(Kim & Yun, 2007) demonstrated that using a tri-linear DCFP in bridge deck isolation leads to:

1. Reduction of base shear forces on the pier in the range of 15%-40% over a bi-linear DCFP, especially for moderate but frequent earthquake events. This effect has been found to be more significant as the mass ratio of the pier to deck (λ_p) and the base isolation period of the bridge (T_d) increase.
2. Reduction of reaction forces on the DCFP bearings in the range of 7%-28% for moderate earthquakes, and increasing of the same forces for strong and extreme earthquakes, in the range of 8%-14%. Both results are given over a bi-linear DCFP.
3. Increase of the bearing deformations, which is judged to be consistent for moderate and strong earthquakes but insignificant for extreme ones.

3.6 Triple FP bearing

There also exist the possibility to implement a device that is made up by a DCFP placed “inside” a bigger DCFP: such a device is called Triple Friction Pendulum bearing. Its behaviour cannot be described as a series of FPS and it may result pretty complicated; besides, to fully illustrate how to model it is not a purpose of this work.

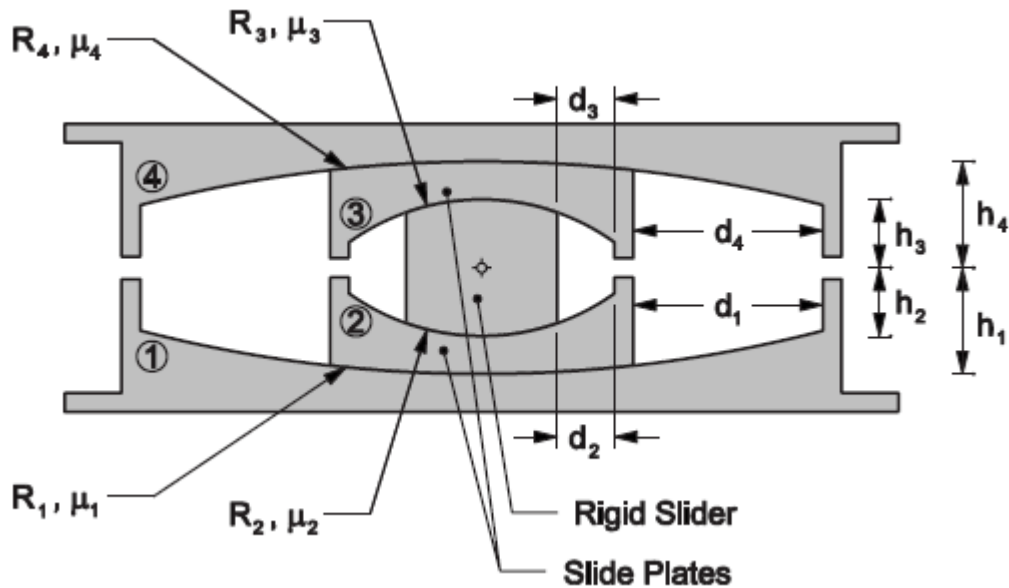


Figure 3.14 - Cross section of the Triple FP bearing

Anyway, it has to be said that the modeling difficulties derive from the fact that simultaneous sliding cannot occur at both interfaces of the internal slide plates. This was observed in experimental testing, and was also predicted analytically and is the reason why it is not possible to model Triple FP bearing as four FPS in series. An example of modeling of the Triple FP was proposed in (Fenz & Constantinou, 2008), implemented on SAP2000 by using both FP elements and gap elements. The model behaviour was found to be practically equal to the experimental and analytical ones, as shown in Figure 3.15. Nowadays, many software have implemented the Triple FP bearing, such as SAP2000.

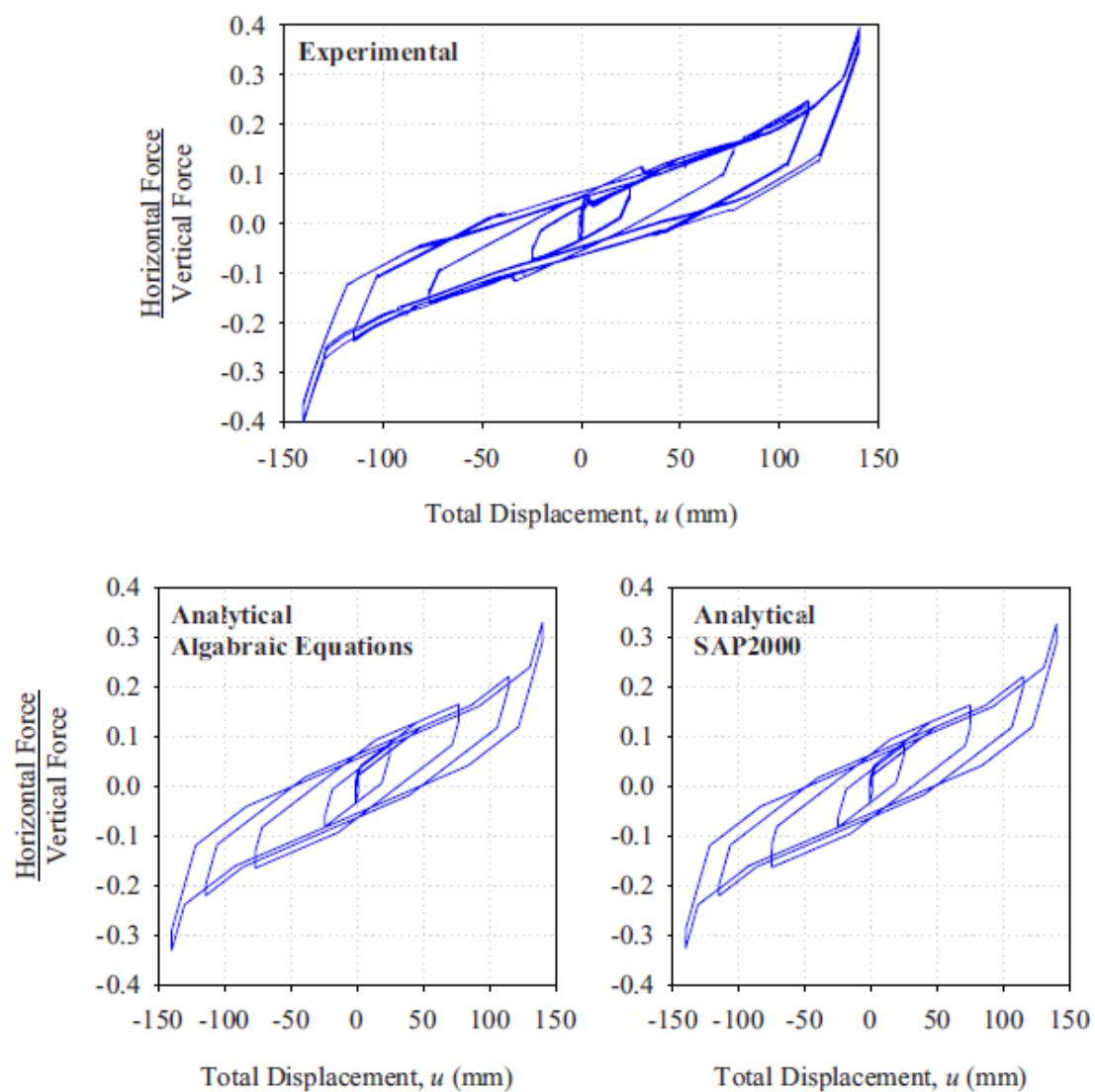


Figure 3.15 - Comparison between analytical, experimental and modeled behaviour

4 Model

The objective is to investigate the behaviour of DCFP system in bridge isolation. More specifically, the bridge is supposed to be symmetrical, so that it is possible and convenient, to analyze the behaviour of just half of it. Since the model is plane, it is implicitly assumed that the main direction of seismic excitation is the longitudinal; transversal behaviour is not taken into account.

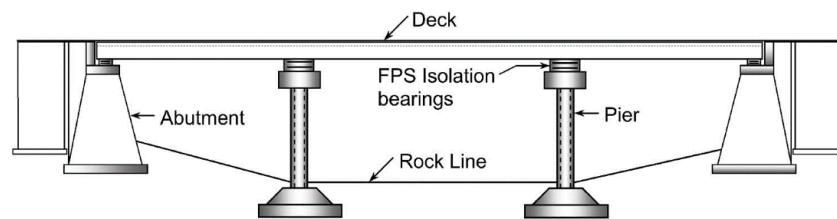


Figure 4.1 - General scheme of an isolated continuous bridge.

The deck is modeled as a lumped mass m_d , supported by the DCFPs of the pier and the abutment. It is supposed to behave as a rigid body, able to move only in longitudinal direction.

The abutment is modeled as a full restraint of that bears, through a DCFP, half of the weight of the deck.

The pier is modeled as a series of discretized masses, is fully restrained at the bottom and bears, through another DCFP, the other half of the weight of the deck. Only lateral deformability of the pier is taken into account.

Finally, the bridge is modeled as an 8-dofm system:

- 5 degrees of freedom are given by the lumped masses of the pier,
- 1 degree of freedom is given by the deck mass,
- 2 degrees of freedom are given by the sliders masses of the two DCFP, placed on top of the abutment and the pier.

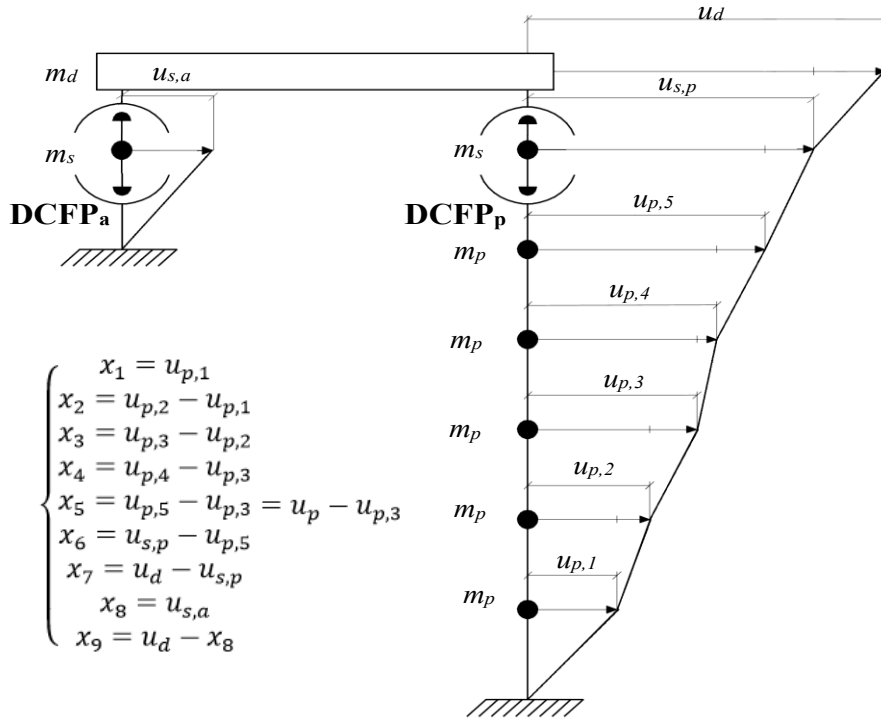


Figure 4.2 - Model scheme

It is possible to write an equation of motion for each one of the n lumped masses that constitute the pier, obtaining the following n equations:

$$m_{p,1}(\ddot{u}_{p,1} + \ddot{u}_g) + c_{p,1}\dot{u}_{p,1} + k_{p,1}u_{p,1} - c_{p,2}(\dot{u}_{p,2} - \dot{u}_{p,1}) - k_{p,2}(u_{p,2} - u_{p,1}) = 0 \quad (4.1)$$

$$m_{p,1}(\ddot{u}_{p,1} + \ddot{u}_g) + c_{p,1}\dot{u}_{p,1} + k_{p,1}u_{p,1} - c_{p,2}(\dot{u}_{p,2} - \dot{u}_{p,1}) - k_{p,2}(u_{p,2} - u_{p,1}) = 0 \quad (4.2)$$

$$m_{p,i}(\ddot{u}_{p,i} + \ddot{u}_g) + c_{p,i}(\dot{u}_{p,i} - \dot{u}_{p,i-1}) + k_{p,i}(u_{p,i} - u_{p,i-1}) - c_{p,i+1}(\dot{u}_{p,i+1} - \dot{u}_{p,i}) - k_{p,i+1}(u_{p,i+1} - u_{p,i}) = 0 \quad (4.3)$$

$$m_{p,n}(\ddot{u}_{p,n} + \ddot{u}_g) + c_{p,n}(\dot{u}_{p,n} - \dot{u}_{p,n-1}) + k_{p,n}(u_{p,n} - u_{p,n-1}) - F_{2,p} = 0 \quad (4.4)$$

Determination of pier stiffness:

Determining the pier stiffness matrix is relatively simple under the hypothesis of $k_{p,i} = k_p$. Once that pier mass matrix $[M]$ and isolated pier main vibrational period T_p are both known, it is possible to write the equation of the eigenvalues problem. Having considered the pier as isolated, forces coming from the DCFP are not considered in this problem, and so applies for the damping matrix $[C]$, which does not play any role in the classical eigenvalues problem. Hence, k_p happens to be the only unknown in the following equation:

$$\det([M] - \omega_p^2[K]) = 0 \quad (4.5)$$

where $\omega_p^2 = \frac{2\pi}{T_p^2}$.

If the displacements are referred to the ground, the matrixes $[M]$ and $[K]$ are then diagonal and tri-diagonal, respectively, and assumes the following aspect:

$$[M] = \begin{bmatrix} m_p & 0 & 0 & 0 & 0 \\ 0 & m_p & 0 & 0 & 0 \\ 0 & 0 & m_p & 0 & 0 \\ 0 & 0 & 0 & m_p & 0 \\ 0 & 0 & 0 & 0 & m_p \end{bmatrix}; \quad [K] = \begin{bmatrix} k_p & -k_p & 0 & 0 & 0 \\ -k_p & 2k_p & -k_p & 0 & 0 \\ 0 & -k_p & 2k_p & -k_p & 0 \\ 0 & 0 & -k_p & 2k_p & -k_p \\ 0 & 0 & 0 & -k_p & 2k_p \end{bmatrix}$$

The equation obtained is a fifth order algebraic one in k_p , as expected. Its five real and positive roots are all possible stiffness for the pier system, since they satisfy the eigenvalues problem equation. The correct k_p must however be the largest one, because one of the other 4 smaller values would imply that the assigned ω_p would not be the smallest one of the five different that would be found solving the equation respect to ω_p (and, by consequence, T_p would not be the largest one and so the main vibrational period).

Two equations are given by the equilibrium condition of the DCFPs' sliders masses:

$$m_{s,p}(\ddot{u}_{s,p} + \ddot{u}_g) - F_{1,p} + F_{2,p} = 0 \quad (4.6)$$

$$m_{s,a}(\ddot{u}_{s,a} + \ddot{u}_g) - F_{1,a} + F_{2,a} = 0 \quad (4.7)$$

The force equilibrium condition of the deck yield the last equation of motion:

$$m_d(\ddot{u}_d + \ddot{u}_g) + F_{1,a} + F_{1,p} = 0 \quad (4.8)$$

where:

u_d , $u_{s,p}$, $u_{s,a}$ and $u_{p,i}$ are the relative displacements of the deck, the slider between two sliding surfaces of the pier and the abutment respectively, and the i^{th} lumped mass of the pier to the ground motion in horizontal direction,

The nonlinear reaction forces on two surfaces can be obtained as:

$$F_{1,p} = \left(\frac{u_d - u_{s,p}}{R_{1,p}} + f_{1,p} \operatorname{sgn}(\dot{u}_d - \dot{u}_{s,p}) \right) \frac{m_d g}{2} \quad (4.9)$$

$$F_{2,p} = \left(\frac{u_{s,p} - u_{p,n}}{R_{2,p}} + f_{2,p} \operatorname{sgn}(\dot{u}_{s,p} - \dot{u}_{p,n}) \right) \left(\frac{m_d}{2} + m_{s,p} \right) g \quad (4.10)$$

where $u_d - u_{s,p}$ represents the deformation of FPS1 and $u_{s,p} - u_{p,n}$ represents the deformation of FPS2.

In this study, DCFP placed on the abutment and on top of the pier are assumed identical, so that:

$$m_{s,p} = m_{s,a} = m_s \quad R_{1,p} = R_{1,a} = R_1 \quad R_{2,p} = R_{2,a} = R_2$$

$$f_{\max,1,p} = f_{\max,1,a} = f_{\max,1} \quad f_{\max,2,p} = f_{\max,2,a} = f_{\max,2}$$

$$f_{\min,1,p} = f_{\min,1,a} = f_{\min,1} \quad f_{\min,2,p} = f_{\min,2,a} = f_{\min,2}$$

The equations are then implemented in MATLAB, obtaining a system, which is, in matrix form:

$$[M'](\{\ddot{u}\} + \{\ddot{u}_g\}) + [C']\{\dot{u}\} + [K']\{u\} + \{\mu\} = \{0\} \quad (4.11)$$

If we want perform the analysis working with drifts between lumped masses of the systems instead of relative displacements respect to the ground, the following linear transformation is applied:

$$\begin{cases} [M']\{\ddot{u}\} = [M'][T]\{\ddot{x}\} \\ [C']\{\dot{u}\} = [C'][T]\{\dot{x}\} \\ [K']\{u\} = [K'][T]\{x\} \end{cases} \quad (4.12)$$

where $[T]$ is a linear transformation between variables:

$$[T] = \begin{bmatrix} 1 & 0 & 0 & 0 & 0 & 0 & 0 & 0 \\ 0 & 1 & -1 & 0 & 0 & 0 & 0 & 0 \\ 0 & 0 & 1 & -1 & 0 & 0 & 0 & 0 \\ 0 & 0 & 0 & 1 & -1 & 0 & 0 & 0 \\ 0 & 0 & 0 & 0 & 1 & -1 & 0 & 0 \\ 0 & 0 & 0 & 0 & 0 & 1 & -1 & 0 \\ 0 & 0 & 0 & 0 & 0 & 0 & 1 & -1 \\ 0 & 0 & 0 & 0 & 0 & 0 & 0 & 1 \end{bmatrix}$$

After a few manipulations, the equations system that will be implemented in MATLAB and Simulink can be written as:

$$[M]\{\ddot{x}\} + [C]\{\dot{x}\} + [K]\{x\} + \{\mu\} = -[M']\{\ddot{u}_g\} \quad (4.13)$$

$$[M] = \begin{bmatrix} m_s & 0 & 0 & 0 & 0 & 0 & 0 & 0 \\ 0 & m_d & m_d & m_d & m_d & m_d & m_d & m_d \\ 0 & m_d & m_d + m_s & m_d + m_s & m_d + m_s & m_d + m_s & m_d + m_s & m_d + m_s \\ 0 & m_d & m_d + m_s & m_d + m_p + m_s & m_d + m_p + m_s & m_d + m_p + m_s & m_d + m_p + m_s & m_d + m_p + m_s \\ 0 & m_d & m_d + m_s & m_d + m_p + m_s & m_d + 2m_p + m_s & m_d + 2m_p + m_s & m_d + 2m_p + m_s & m_d + 2m_p + m_s \\ 0 & m_d & m_d + m_s & m_d + m_p + m_s & m_d + 2m_p + m_s & m_d + 3m_p + m_s & m_d + 3m_p + m_s & m_d + 3m_p + m_s \\ 0 & m_d & m_d + m_s & m_d + m_p + m_s & m_d + 2m_p + m_s & m_d + 3m_p + m_s & m_d + 4m_p + m_s & m_d + 4m_p + m_s \\ 0 & m_d & m_d + m_s & m_d + m_p + m_s & m_d + 2m_p + m_s & m_d + 3m_p + m_s & m_d + 4m_p + m_s & m_d + 5m_p + m_s \end{bmatrix}$$

$$[C] = \begin{bmatrix} 0 & 0 & 0 & 0 & 0 & 0 & 0 & 0 \\ 0 & 0 & 0 & 0 & 0 & 0 & 0 & 0 \\ 0 & 0 & 0 & 0 & 0 & 0 & 0 & 0 \\ 0 & 0 & 0 & c_p & 0 & 0 & 0 & 0 \\ 0 & 0 & 0 & 0 & c_p & 0 & 0 & 0 \\ 0 & 0 & 0 & 0 & 0 & c_p & 0 & 0 \\ 0 & 0 & 0 & 0 & 0 & 0 & c_p & 0 \\ 0 & 0 & 0 & 0 & 0 & 0 & 0 & c_p \end{bmatrix}$$

$$[K] = \begin{bmatrix} k_1 + k_2 & -k_1 & -k_1 & -k_1 & -k_1 & -k_1 & -k_1 & -k_1 \\ -k_1 & 2k_1 & k_1 & k_1 & k_1 & k_1 & k_1 & k_1 \\ -k_1 & k_1 & k_1 + k_2 & k_1 & k_1 & k_1 & k_1 & k_1 \\ -k_1 & k_1 & k_1 & k_1 + k_p & k_1 & k_1 & k_1 & k_1 \\ -k_1 & k_1 & k_1 & k_1 & k_1 + k_p & k_1 & k_1 & k_1 \\ -k_1 & k_1 & k_1 & k_1 & k_1 & k_1 + k_p & k_1 & k_1 \\ -k_1 & k_1 & k_1 & k_1 & k_1 & k_1 & k_1 + k_p & k_1 \\ -k_1 & k_1 & k_1 & k_1 & k_1 & k_1 & k_1 & k_1 + k_p \end{bmatrix}$$

Normalizing the equations by dividing them by the deck mass m_d , the following ratios are introduced:

- Mass ratios:

$$\lambda_p = \frac{m_p}{m_d}$$

$$\lambda_s = \frac{m_s}{m_d}$$
(4.14a,b)

- Damping coefficients:

$$\xi_d = \frac{c_d}{2m_d\omega_d}$$

$$\xi_p = \frac{c_p}{2m_p\omega_p}$$
(4.15a,b)

- Circular frequencies:

$$\omega_d^2 = \frac{k_d}{m_d}$$

$$\omega_p^2 = \frac{k_p}{m_p}$$
(4.16a,b)

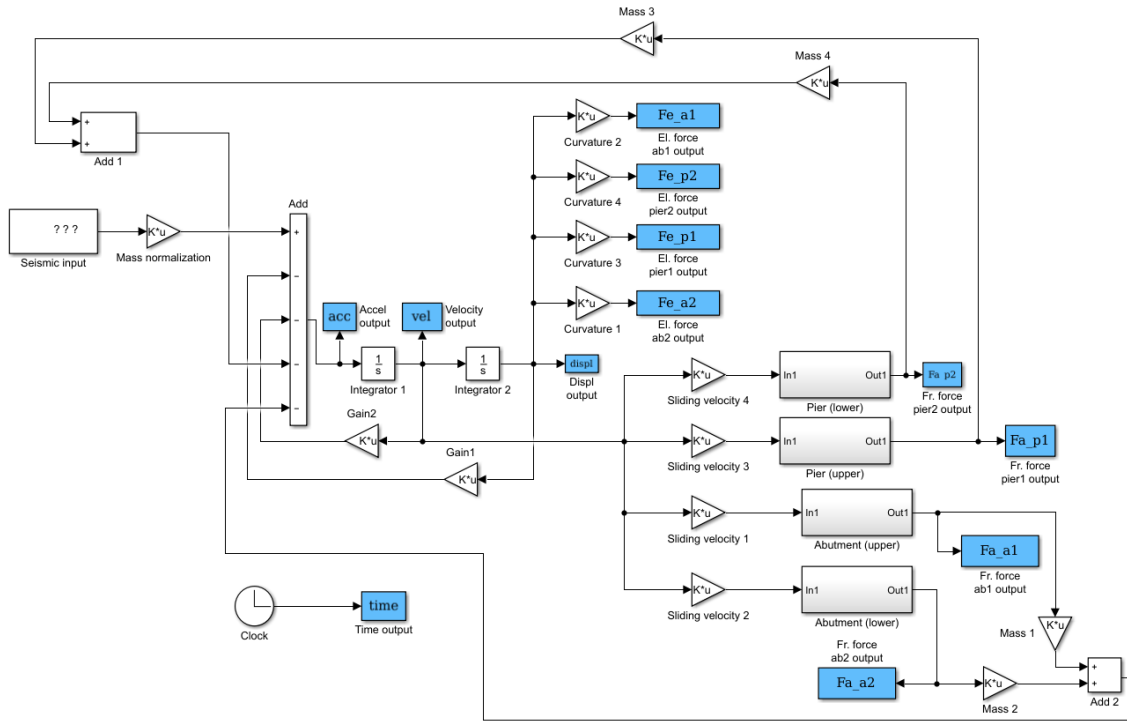


Figure 4.3 – Simulink Model

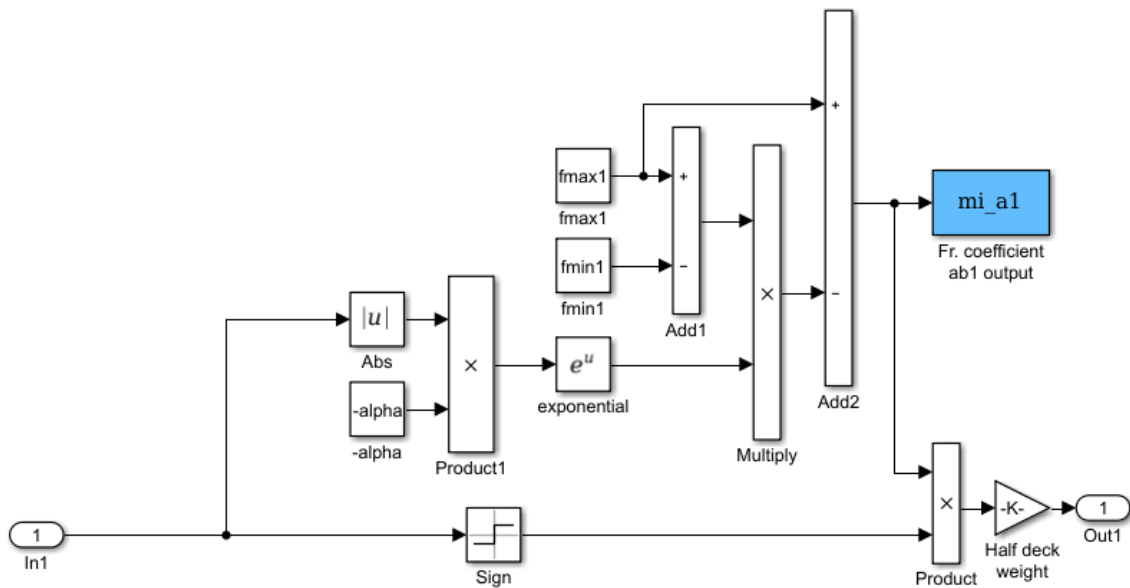


Figure 4.4 – Simulink sub-model for instantaneous friction evaluation

4.1 Validation of the model

The model implemented in MATLAB & Simulink needs to be validated through a comparison of the results of an analysis, with an arbitrary set of parameters, with the results obtained carrying out the same analysis with a software. Since it has many features that makes it suitable for non-linear dynamics analysis, SAP2000 has been chosen for this purpose. It is necessary to point out that different software

may use different methods, with different accuracy, to solve a system of differential equations; nevertheless, results have to be approximately the same to ensure the validity of the model, particularly for the peak response values.

The following graphs show the comparison between the results of two analyses performed independently with SAP2000 and MATLAB & Simulink. Analyses have been run with the following set of parameters:

- $T_d = 2$ s
- $T_p = 0.1$ s
- $\lambda_s = 0.1$
- $f_{max} = 0.03$

The non-scaled seismic external action is the following one:

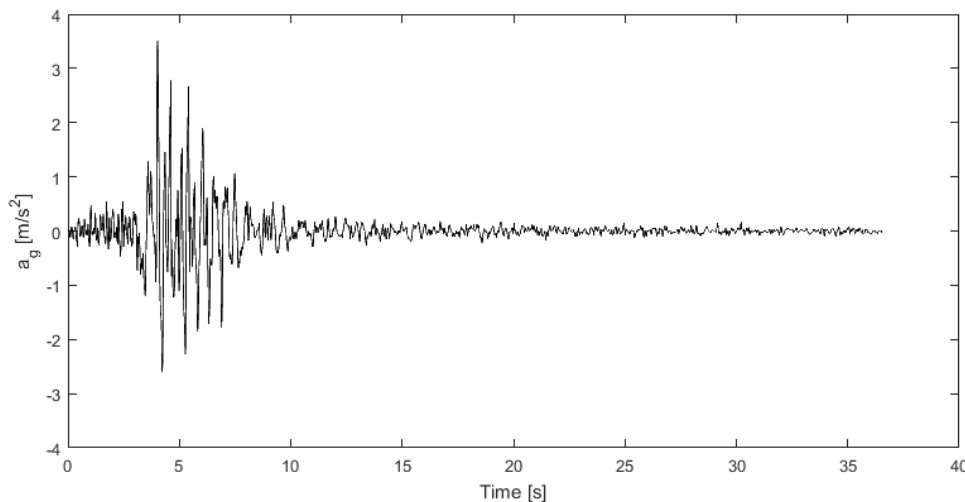


Figure 4.5 - Test earthquake record

and the time integration methods used to solve the analysis are:

- SAP2000: HHT (Hilber-Hughes-Taylor) method, with $\alpha = 0, \beta = 0.25, \gamma = 0.5$.
- Simulink: variable-step ode23tb (stiff/TR-BDF2), with a relative tolerance of $1e-2$ and an absolute tolerance of $1e-5$

Such a model needs to be validated through a comparison with another one that uses equivalent FPSs instead of DCFPs. This equivalence can be imposed as follows:

$$\begin{aligned}
K_{FPS} &= \frac{mg}{R_{eqv}} = K_{DCFP} = \frac{mg}{R_1 + R_2} \xrightarrow{\text{yields}} R_{eqv} = R_1 + R_2 \\
f_{eqv} &= \frac{f_1 R_1 + f_2 R_2}{R_1 + R_2} \xrightarrow{\text{yields}} f_1 = f_2 = f_{eqv}
\end{aligned}
\tag{4.17a,b}$$

where two FPSs in series are assumed to move in the same direction.

The validation is then made up by two steps:

1. After performing a modal analysis of both models, the main vibration periods (T_d , T_p) of the global structure have to be identical. Usually, the differences between the secondary vibration periods of the pier are negligible.
2. A non-linear dynamic analysis has to be performed then, and the models have to give the same results in terms of relative displacement between pier and deck and relative displacement of the top of the pier with respect to the ground. However, plotting them against time will give slightly different results, because the systems that are numerically integrated are not the same. Peak values of the displacement time history have anyway to be equals, in order to prove that the presence of the slider masses does not influence the overall behavior of the structure. In addition, a comparison between the force-displacement laws of the two isolation systems has to give approximatively the same hysteretic behavior.

Simulink offers the possibility to choose between several time integration methods, which can be variable-step or fixed-step. Although variable-step methods are usually more accurate than fixed-step, their use implies a considerable increment of the time required for the analysis, up to 50 times the fixed-step integration. Given this, both time integration methods have been tested on a single seismic event in order, with assigned structural parameters, in order to evaluate the approximation errors of the fixed-step and find an acceptable time step to perform the analysis.

More specifically, the comparison has been made on two different time integration methods:

- Fixed-step: ode3 (Bogacki-Shampine)
- Variable-step: ode23tb (stiff/TR-BDF2), with a relative tolerance of $1e-2$ and an absolute tolerance of $1e-5$.

Both of them are available on Simulink solver.

4.2 FPSs model validation

T_i [s]	MATLAB	SAP2000
$T_{p,5}$	0.014832	0.01484
$T_{p,4}$	0.016915	0.01692
$T_{p,3}$	0.021725	0.02174
$T_{p,2}$	0.034221	0.03424
T_{is}	2.012488	2.01853
$T_{p,1}$	0.098907	0.09896

Table 4.1 – FPSs model, modal period comparison

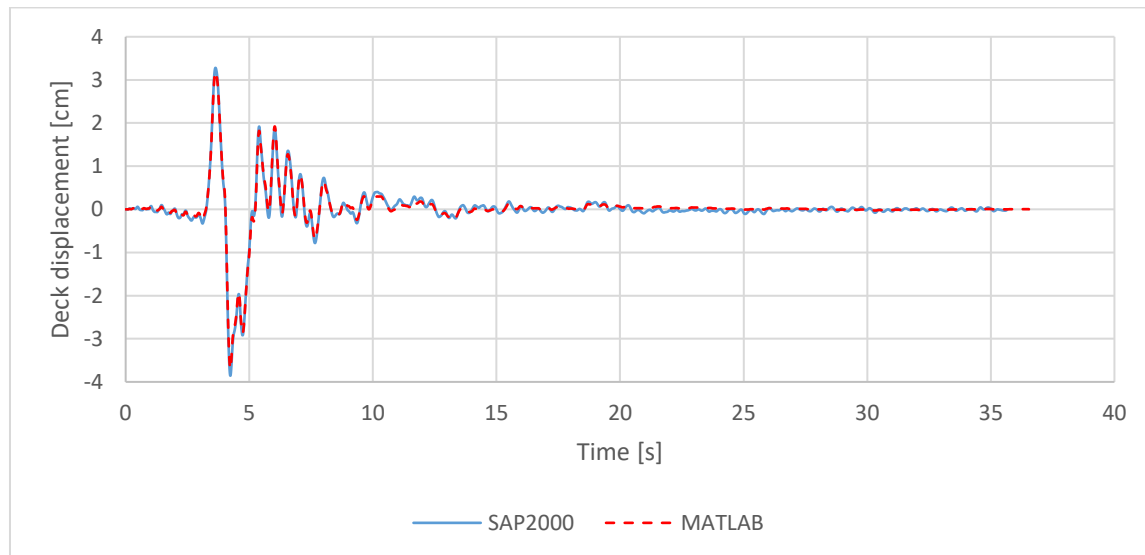


Figure 4.6 - Deck displacement comparison (FPS)

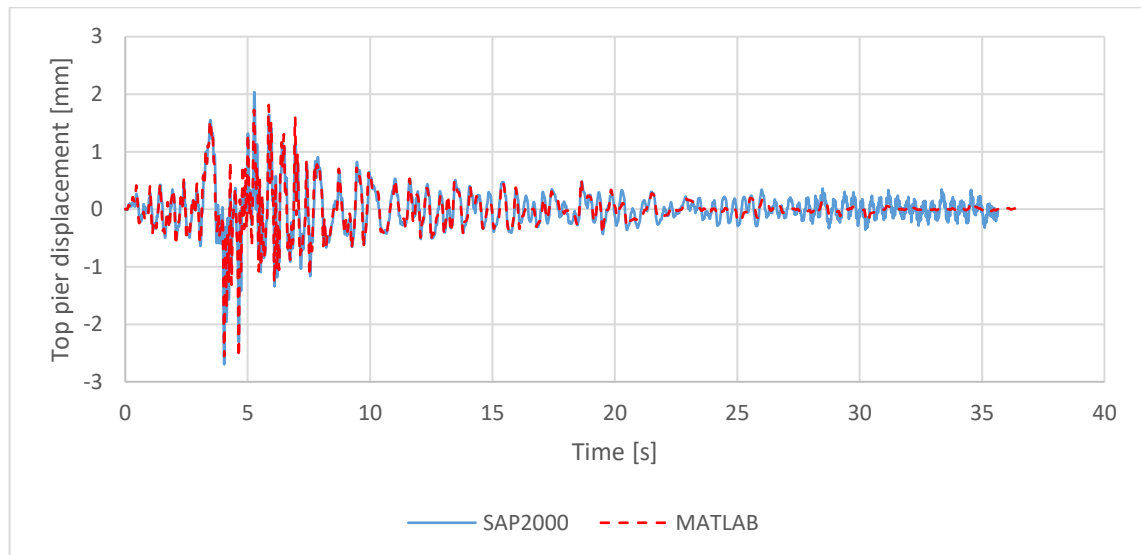


Figure 4.7 - Pier cap displacement comparison (FPS)

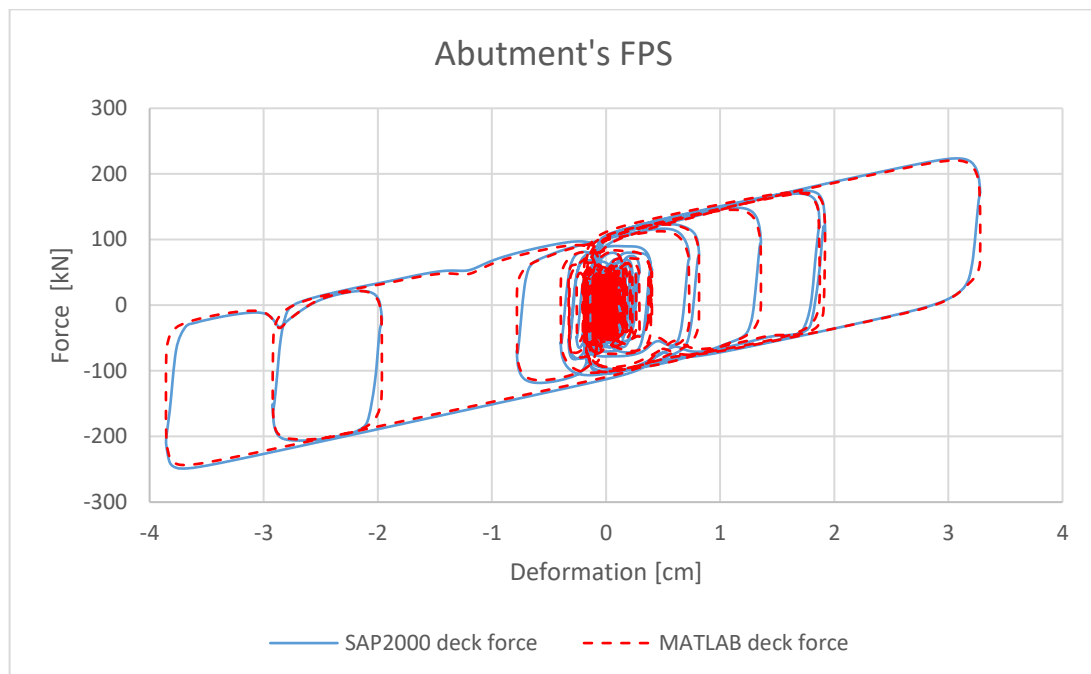


Figure 4.8 - Abutment isolator force-displacement law comparison (FPS)

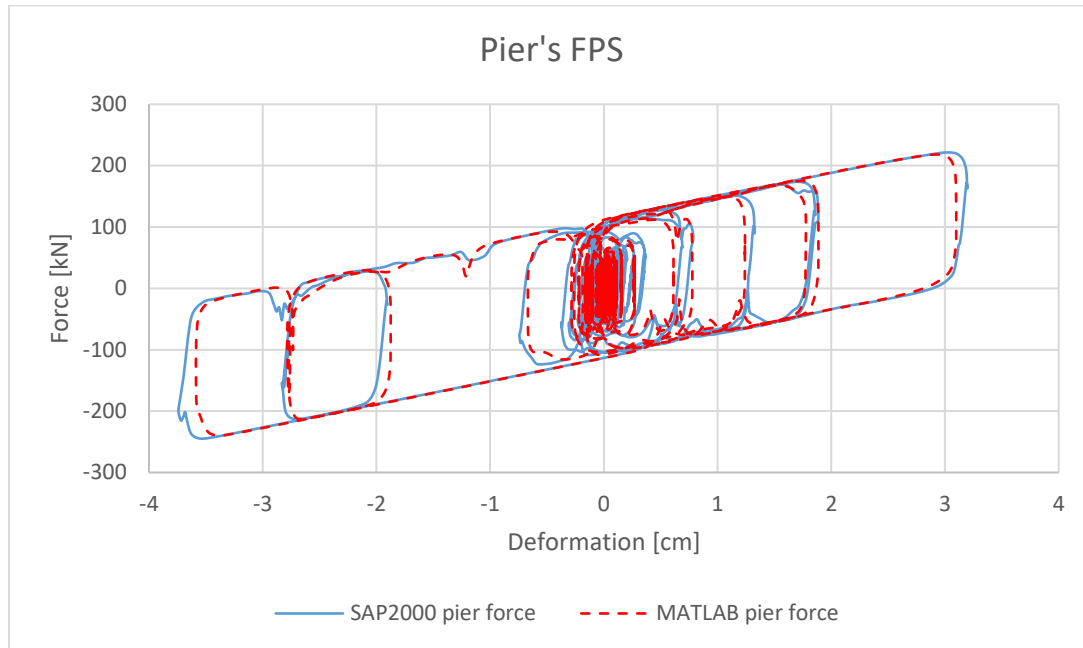


Figure 4.9 - Pier isolator force-displacement law comparison (FPS)

Deck and top pier's displacement, both respect to the ground, and the force-displacement behaviour of abutment and pier's FPS look very similar although time integration method is different for the two software. The models are then practically equivalent.

4.3 DCFPs model validation

Firstly, it is necessary to evaluate a reasonable value for λ_s . This evaluation is difficult because an excessively low value of m_d would lead to numerical problems in the solution of the system, while a high value is of course unrealistic.

A series of analysis showed that low values of λ_s can guarantee a similar behaviour between two systems, of which one isolated with FPSs and the other with equivalent DCFP systems, in the peak displacement region. Once the earthquake motion become small, while the system isolated with FPS tends to stability, the other tends to be unstable, and the smaller is λ_s , the more unstable will be the system. This may be due to numerical problems that occur during the integration of the equations. Choosing $\lambda_s = 0.005$ is a good compromise solution that allows obtaining negligible difference between peak displacements of the two models and acceptable instability during the earthquake ending phase.

The following step is to validate a MATLAB model implemented with equivalent DCFPs, verifying that the response is the same to the already tested MATLAB

model. Additional periods, coming from the slider's mass movements, are not significant due to the very small masses of the sliders.

T_i [s]	MATLAB	SAP2000
$T_{p,5}$	0.014832	0.01484
$T_{p,4}$	0.016914	0.01692
$T_{p,3}$	0.021718	0.02173
$T_{p,2}$	0.034178	0.0342
T_{is}	2.015072	2.02112
$T_{p,1}$	0.099937	0.09258
$T_{add,1}$	0.10714	0.10733
$T_{add,2}$	0.092412	0.10024

Table 4.2 - DCFPs model, modal period comparison

The same comparison is then made to the same structure modeled with two DCFPs equivalent to the one modeled with FPSs analyzed before.

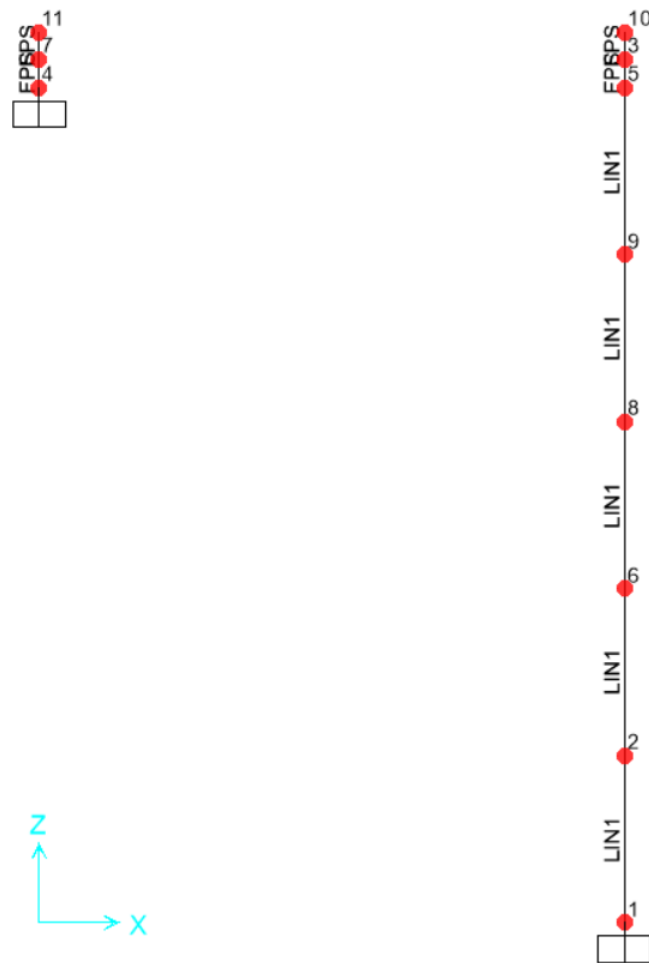


Figure 4.10 - SAP2000 DCFP model

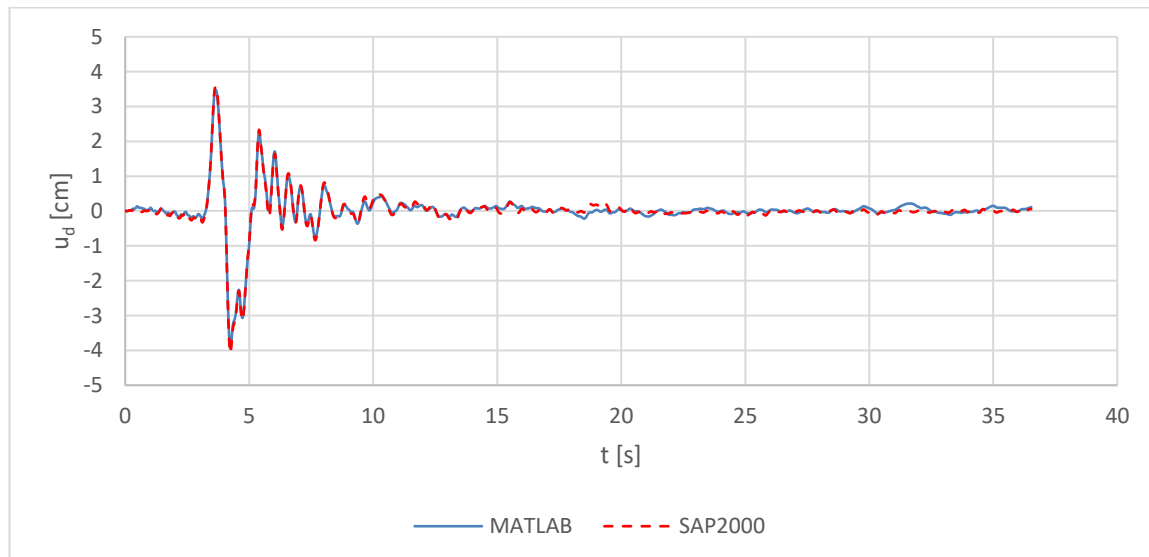


Figure 4.11 - Deck displacement comparison (DCFP)

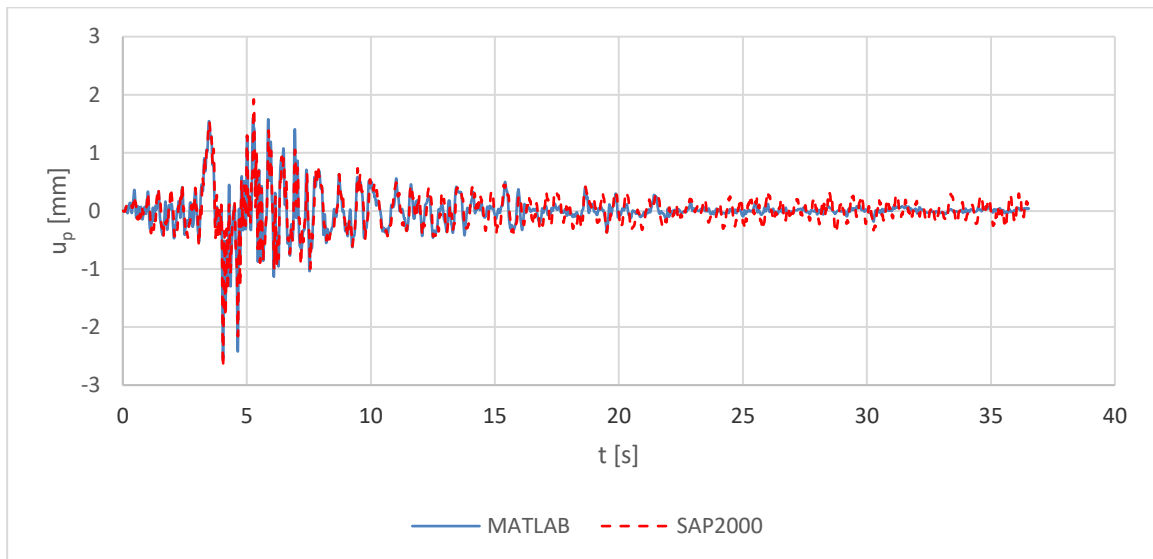


Figure 4.12 - Pier cap displacement comparison (DCFP)

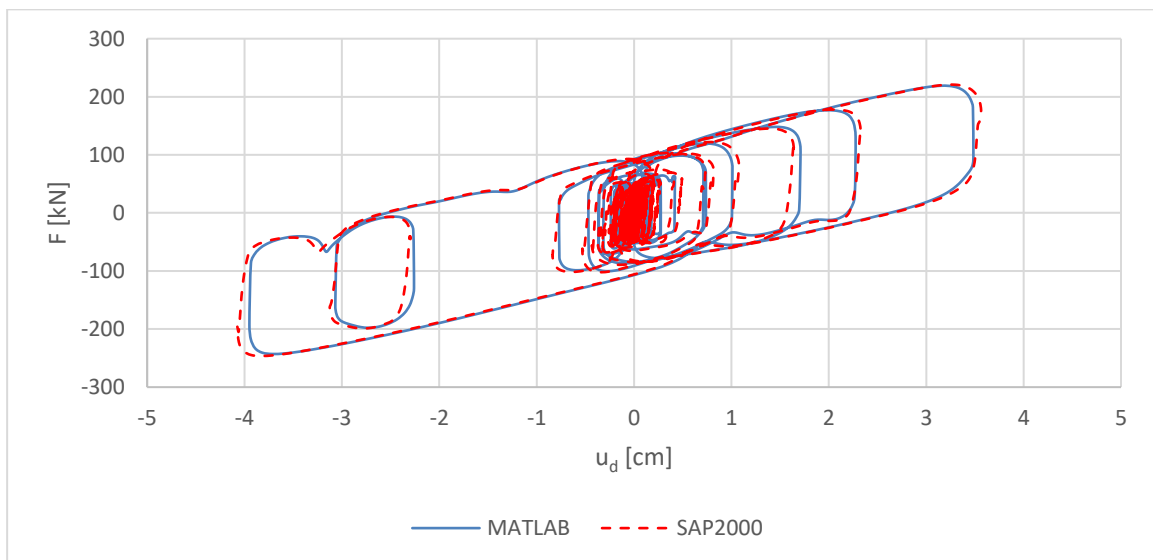


Figure 4.13 - Force-displacement law comparison (DCFP)

5 Parametrical analysis

5.1 Input parameters of the system

$T_p [s]$	$T_d [s]$	$\lambda_p [-]$
0.05	2	0.1
0.1	2.5	0.15
0.15	3	0.2
0.2	3.5	
	4	

Table 5.1 – Input parameters

The main dynamic parameters, used for the analyses, are the ones in Table 5.1. They have been collected from typical values of dynamic parameters used in literature for isolated bridges.

5.1.1 Pier main period T_p

Four different values of pier main period have been used: 0.05, 0.1, 0.15 and 0.2 s.

5.1.2 Isolation period T_d

Five different values of isolation period have been used: 2, 2.5, 3, 3.5 and 4 s. As it is easy to see with the (3.31), under the hypothesis that the two DCFP are equals, there is a quadratic proportionality between the isolation period and the sum of the radii of FPS1 and FPS2. This relation is illustrated graphically and analytically in the following figure:

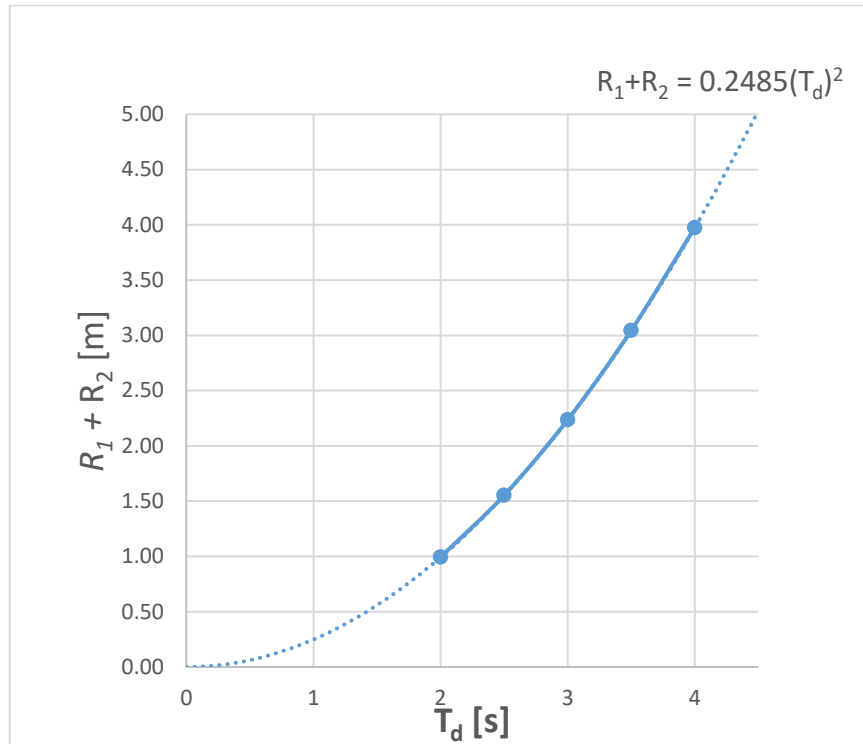


Figure 5.1 - Relation between DCFP radii and isolation period

5.1.3 Mass ratio of the pier to the deck

$$\Pi_\lambda = \frac{m_p}{m_d} = \lambda_p$$

Three different values of mass ratio have been used: 0.1, 0.15 and 0.2.

5.1.4 Seismic input

A set of 30 earthquake records, containing the horizontal main component of 19 different earthquakes, regardless of their distance from the hypocentre, their magnitude and their spectrum, has been used. The earthquake records were found on (Pacific Earthquake Engineering Research Center (PEER), 2006), (Azienda Accelerometrica Italiana (ITACA), 2016) and (Internet Site for European Strong Motion Data, 2016). The response spectra of all the earthquake records are plotted together with the medium response spectrum in Figure 5.2.

#	Year	Earthquake name	Recording station name	V_{s30} [m/s]	Fault type	M [—]	R_s [km]	PGA [g]
1	1994	Northridge	Beverly Hills—Mulhol	356	Thrust	6.7	13.3	0.52
2	1994	Northridge	Canyon Country—WLC	309	Thrust	6.7	26.5	0.48
3	1994	Northridge	LA—Hollywood Stor	316	Thrust	6.7	22.9	0.36
4	1999	Duzce, Turkey	Bolu	326	Strike-slip	7.1	41.3	0.82
5	1999	Hector Mine	Hector	685	Strike-slip	7.1	26.5	0.34
6	1979	Imperial Valley	Delta	275	Strike-slip	6.5	33.7	0.35
7	1979	Imperial Valley	El Centro Array #11	196	Strike-slip	6.5	29.4	0.38
8	1995	Kobe, Japan	Nishi-Akashi	609	Strike-slip	6.9	8.7	0.51
9	1995	Kobe, Japan	Shin-Osaka	256	Strike-slip	6.9	46.0	0.24
10	1999	Kocaeli, Turkey	Duzce	276	Strike-slip	7.5	98.2	0.36
11	1999	Kocaeli, Turkey	Arcelik	523	Strike-slip	7.5	53.7	0.22
12	1992	Landers	Yermo Fire Station	354	Strike-slip	7.3	86.0	0.24
13	1992	Landers	Coolwater	271	Strike-slip	7.3	82.1	0.42
14	1989	Loma Prieta	Capitola	289	Strike-slip	6.9	9.8	0.53
15	1989	Loma Prieta	Gilroy Array #3	350	Strike-slip	6.9	31.4	0.56
16	1990	Manjil, Iran	Abbar	724	Strike-slip	7.4	40.4	0.51
17	1987	Superstition Hills	El Centro Imp. Co.	192	Strike-slip	6.5	35.8	0.36
18	1987	Superstition Hills	Poe Road (temp)	208	Strike-slip	6.5	11.2	0.45
19	1987	Superstition Hills	Westmorland Fire Stat.	194	Strike Slip	6.5	15.1	0.21
20	1992	Cape Mendocino	Rio Dell Overpass	312	Thrust	7.0	22.7	0.55
21	1999	Chi-Chi, Taiwan	CHY101	259	Thrust	7.6	32	0.44
22	1999	Chi-Chi, Taiwan	TCU045	705	Thrust	7.6	77.5	0.51
23	1971	San Fernando	LA—Hollywood Stor	316	Thrust	6.6	39.5	0.21
24	1976	Friuli, Italy	Tolmezzo	425	Thrust	6.5	20.2	0.35
25	1980	Irpinia	Bisaccia	496		6.9	21.3	0.94
26	1979	Montenegro	ST64	1083	Thrust	6.9	21.0	0.18
27	1997	Umbria Marche	ST238	n/a	Normal	6.0	21.5	0.19
28	2000	South Iceland	ST2487	n/a	Strike-slip	6.5	13	0.16
29	2000	South Iceland (a.s.)	ST2557	n/a	Strike-slip	6.4	15.0	0.13
30	2003	Bingol	ST539	806	Strike-slip	6.3	14.0	0.30

Table 5.2 - Earthquakes used and their main characteristics.

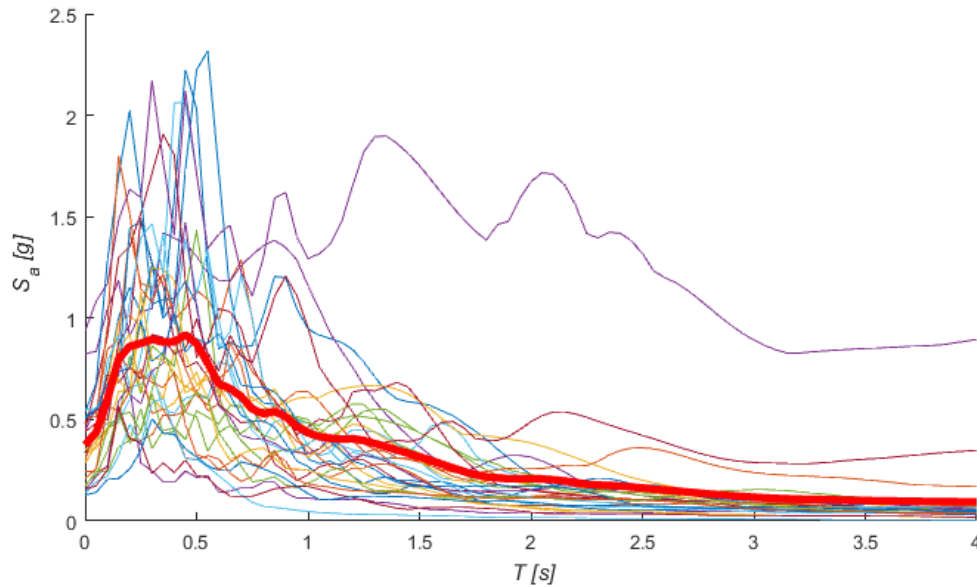


Figure 5.2 - Response spectra of the used earthquakes and average spectrum

5.1.5 Normalized friction coefficients Π_μ

$$\Pi_\mu = \mu(\dot{\psi}_a) \frac{g}{a_0} \quad (5.1a)$$

Ninety-five values of friction coefficients have been used. The first 61 normalized friction values go from 0 to 0.3, with a regular spacing of 0.005. The remaining

values, from 0.3 to 2, are spaced with a distance of 0.05, because optimal values of normalized friction are not expected to be in this range.

This parameter depends on the response of the system through the relative sliding velocity of the slider along each sliding surface. It is instead more efficient to use a parameter independent on the response, since it would not depend by the seismic action, using the maximum friction coefficient instead of the instantaneous friction coefficient to calculate the normalized friction coefficient.

$$\Pi_{\mu}^* = f_{max} \frac{g}{a_0} \quad (5.1b)$$

In this way, Π_{μ}^* is also equal to the dimensionless damping index introduced in (Tubaldi, 2014) for non-linear viscous dampers in case of nil viscous damping exponent and constant friction.

5.2 DCFP parameters

The two DCFP placed on the pier top and on the abutment have the same characteristics.

In order to simplify the problem by reducing the number of independent parameters, it is assumed that for every DCFP internal sliding surface $f_{max} = 3f_{min}$. This assumption is based on the regression of experimental results (Castaldo & Tubaldi, Influence of FPS bearing properties on the seismic performance of base-isolated structures, 2015).

The following two sets of DCFP's parameters are used:

	R_1/R_2	$f_{1,max}/f_{2,max}$	$f_{i,max}/f_{i,min}$	f_{eqv}^*
a)	2	4	3	$3f_2$
b)	2	2	3	$(5/3)f_2$

* f_{eqv} is here calculated under the hypothesis of sliding occurring on both surfaces and at the same velocity, with the (3.34).

As shown in Figure 5.1, any isolation period T_d can be obtained regardless the ratio R_1/R_2 . This implies that every T_d may be obtained with different ratios R_1/R_2 if $R_1 + R_2$ is constant. The sum $R_1 + R_2$ varies parabolically with T_d .

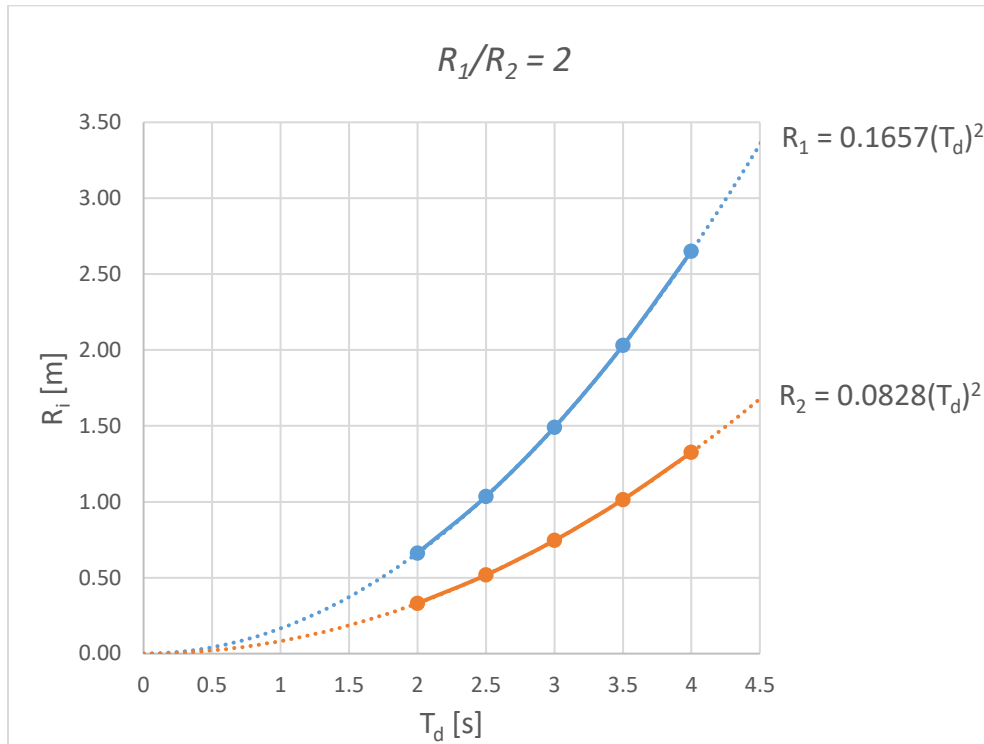


Figure 5.3 - Relation between curvature radii when $R_1/R_2 = 2$.

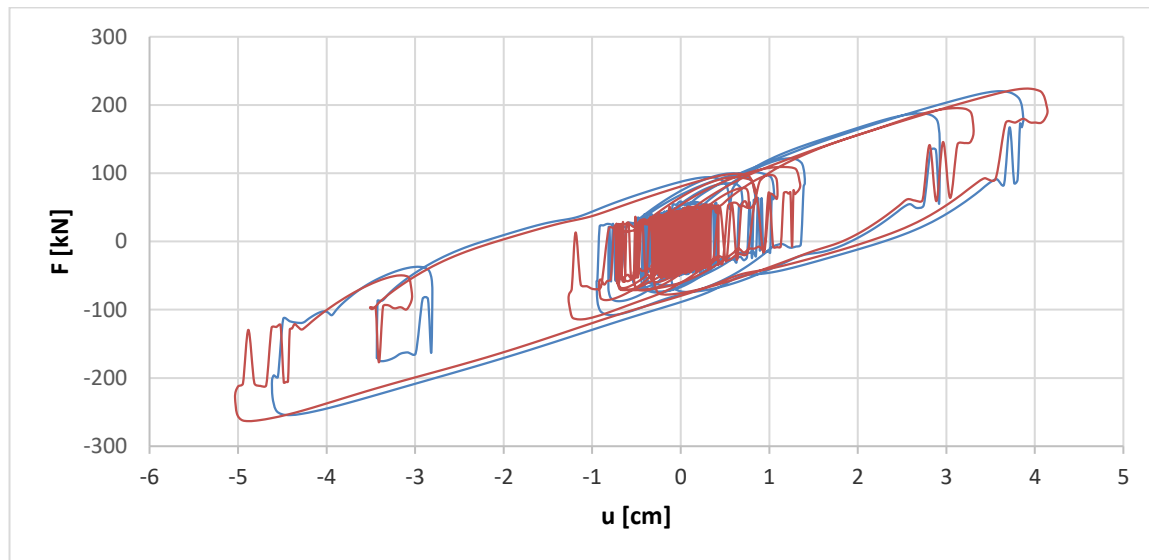


Figure 5.4 - Force-displacement behaviour of abutment DCFP under seismic excitation for $r_f = 4$ (red) and $r_f = 2$ (blue).

5.3 Dimensionless parameters

To generalize the problem and unbound it from the characteristic control parameters, it is necessary to construct dimensionless parameters starting from the original ones, manipulating them as done in (Castaldo & Tubaldi, Influence of FPS bearing properties on the seismic performance of base-isolated structures,

2015). To do so, the seismic input \ddot{u}_g is expressed as a product of a scale factor IM and a non-dimensional time function $\gamma(t)$:

$$\ddot{u}_g(t) = IM \cdot \gamma(t) = IM \cdot l(\tau) \quad (5.2)$$

$l(\tau)$ is obtained from the scalar function $\gamma(t)$ by dividing it by ω_d , so that time too become dimensionless.

Scaling of the seismic input is made by scaling the pseudo-acceleration spectra, imposing that they have unitary value (a_0) at the chosen isolation period T_d : by keeping the shape of the spectra unchanged, the earthquake records are scaled proportionally. This procedure should be done for every acceleration spectrum and for every assigned ξ_d , since it affect the acceleration spectrum; though, damping in the deck is assumed to be nil and then the spectra are not affected by it. This assumption is always on safety side, due to the fact that there is always some damping force acting in the deck, even if small. Then, for each T_d a set of 30 earthquake records is obtained. This procedure is not mandatory to perform a non-linear analysis, but as explained in (Iervolino, Cosenza, & Galasso, 2009) it is very helpful in reducing the variability of the structural response, allowing to obtain accurate results with a lower number of analyses.

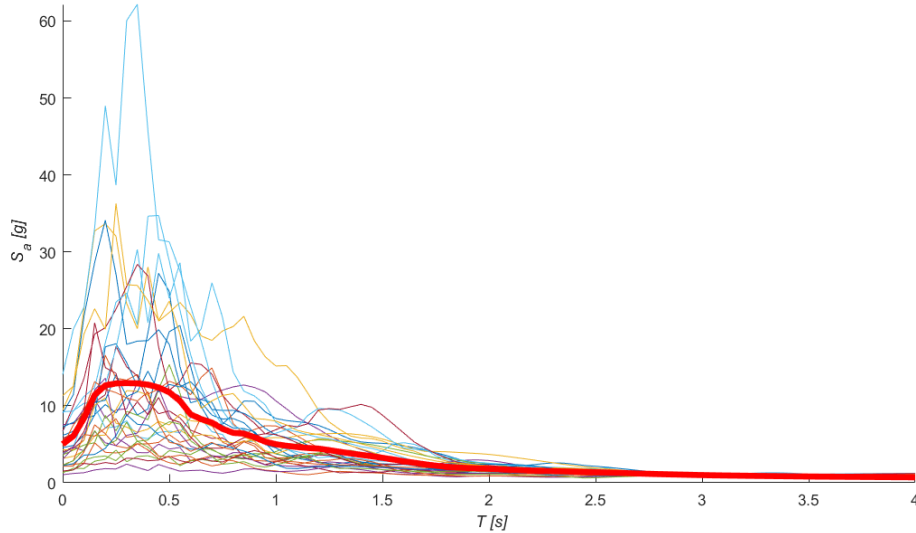


Figure 5.5 - Scaled response spectra (unitary value for $T = 3$ s)

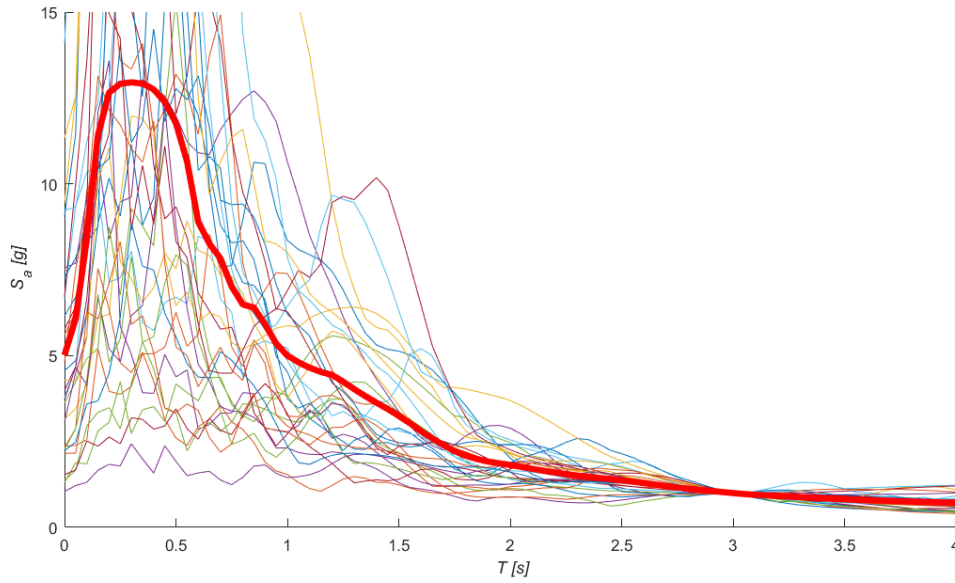


Figure 5.6 - Scaled seismic spectra (unitary value for $T = 3$ s), detail

5.3.1 Additional parameters

$$\Pi_{\omega} = \frac{\omega_p}{\omega_d} \quad (5.3)$$

This parameter measures the isolation grade of the system,

$$\Pi_{\xi_p} = \xi_p \quad \Pi_{\xi_d} = \xi_d$$

These parameters measure the damping level in the pier and in the deck respectively.

$$\xi_{eq} = \frac{2}{\pi \frac{\psi_{u_d}}{\Pi_{\mu,1}^* R_1 + \Pi_{\mu,2}^* R_2} + 1} \quad (5.4)$$

This parameter measures the damping capability of the abutment isolator. The damping capability of the pier isolator may be calculated by substituting ψ_{u_d} with ψ_{x_d} .

Once the analyses have been run, it is necessary to work on the output parameters in order to obtain dimensionless outputs, since it is the only way to obtain results that are independent from the structure dimensions. To fulfill this work's scope, only maximum response parameters in the follow are necessary, for each combination of T_d , T_p , λ_p and f . Manipulating the previous equations with the dimensionless seismic input, it is possible to obtain the non-dimensional displacements introducing a scale factor $\frac{\omega_d^2}{IM}$.

5.3.2 DCFPs deformations

$$\psi_{u,d} = \frac{u_{d,max}\omega_d^2}{S_A(T_d)} = \frac{u_{d,max}\omega_d^2}{a_0} \quad (5.5)$$

This parameter is the deck absolute displacement respect to the ground, and since the abutment DCFP is fixed to the ground and to the deck bridge, it correspond numerically with the abutment DCFP horizontal deformation.

$$\psi_{x,d} = \frac{x_{d,max}\omega_d^2}{S_A(T_d)} = \frac{x_{d,max}\omega_d^2}{a_0} \quad (5.6)$$

This one is the difference between the deck absolute displacement and the top pier absolute displacement, which is numerically equal to the pier DCFP horizontal deformation.

5.3.3 Single FPSs deformations

$$\psi_{x,i} = \frac{x_{i,max}\omega_d^2}{S_A(T_d)} = \frac{x_{i,max}\omega_d^2}{a_0}, \quad i = 6,7,8,9 \quad (5.7)$$

There are two DCFP in the system, and then it is possible to calculate the displacement of the slider respect to each surface. Indexes meaning are showed in FIGURE. x_9 is the only displacement which is not calculated as an independent one, but as a linear combination of the others.

5.3.4 Pier cap displacement

$$\psi_{u,p} = \frac{u_{p,max}\omega_d^2}{S_A(T_d)} = \frac{u_{p,max}\omega_d^2}{a_0} \quad (5.8)$$

5.3.5 DCFP forces

Two different dimensionless form are proposed for the single FPSs. The dimensionless form of the forces of the abutment FPS1 and FPS2 does not take into account the pier mass.

$$\psi_{F_{p,i}} = \frac{|F_{p,i}|_{max}}{(m_d + \sum m_{p,i})S_A(T_d)} = \frac{|F_{p,i}|_{max}}{(m_d + m_p)a_0}, \quad i = 1,2 \quad (5.9a,b)$$

$$\psi_{F_{a,i}} = \frac{|F_{a,i}|_{max}}{m_d S_A(T_d)} = \frac{|F_{a,i}|_{max}}{m_d a_0}, \quad i = 1, 2$$

5.4 Statistical hypotheses

The output parameters obtained for the 30 different seismic input are supposed to be distributed log-normally, for every combination of the others system parameters. In order to evaluate an optimal normalized friction value, it is useful to calculate the geometric mean and the geometric standard deviation of every output parameters, so that the optimums can be evaluated at different percentile.

$$GM(D) = \sqrt[N]{d_1 \cdot \dots \cdot d_N}$$

$$\beta(D) = \sigma_{\ln(D)} = \sqrt{\frac{(\ln d_1 - \ln[GM(D)])^2 + \dots + (\ln d_N - \ln[GM(D)])^2}{N - 1}} \quad (5.10a,b)$$

Due to the hypothesis of log-normal distribution, the generic response may be expressed as:

$$d_k = GM(D) e^{f(k)\beta(D)} \quad (5.11)$$

where $f(k)$ is a function of the k argument (the percentile of the log-normal distribution) that assume the values $f(50) = 0$, $f(84) = 1$ and $f(16) = -1$ (Ang & Tang, 2007).

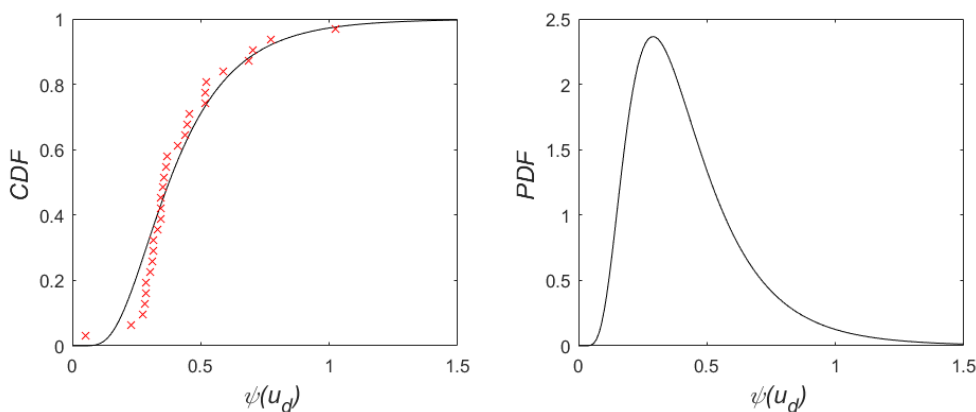


Figure 5.7 - CDF and PDF obtained from analysis results for the 30 seismic events for $T_d = 2$ s, $T_p = 0.1$ s, $l_p = 0.1$, $f = 0.3/g$, case A

5.5 Results

Results of the analyses are plotted in the following pages in terms of geometric mean GM and standard deviation β of the output parameters, for the various combination of input parameters. More specifically, each plot has on the horizontal axes the normalized friction coefficient and the isolation period. 3 different 3D surfaces show the result of the analyses, each one calculated for a different pier to deck mass ratio.

5.5.1 Case A

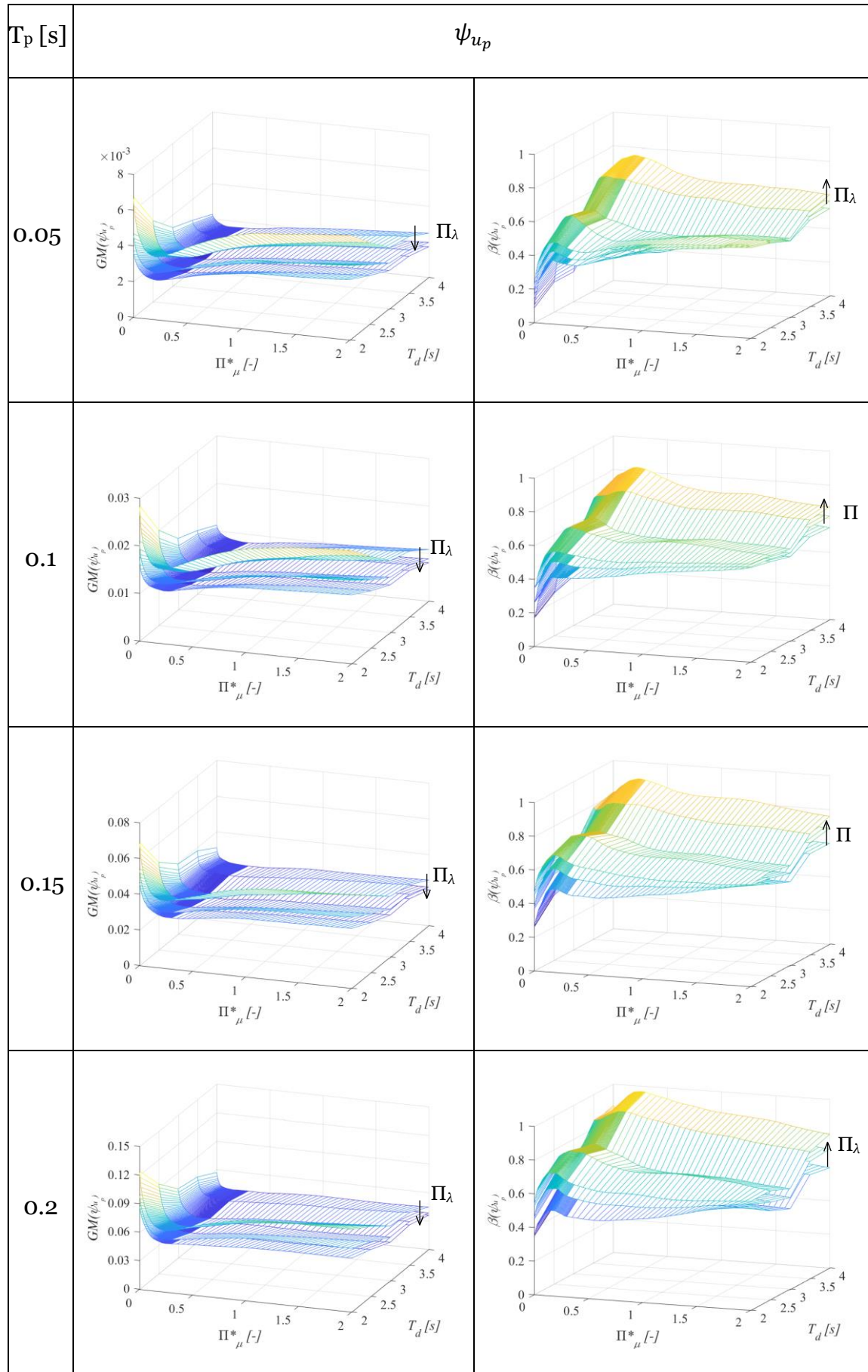


Table 5.3

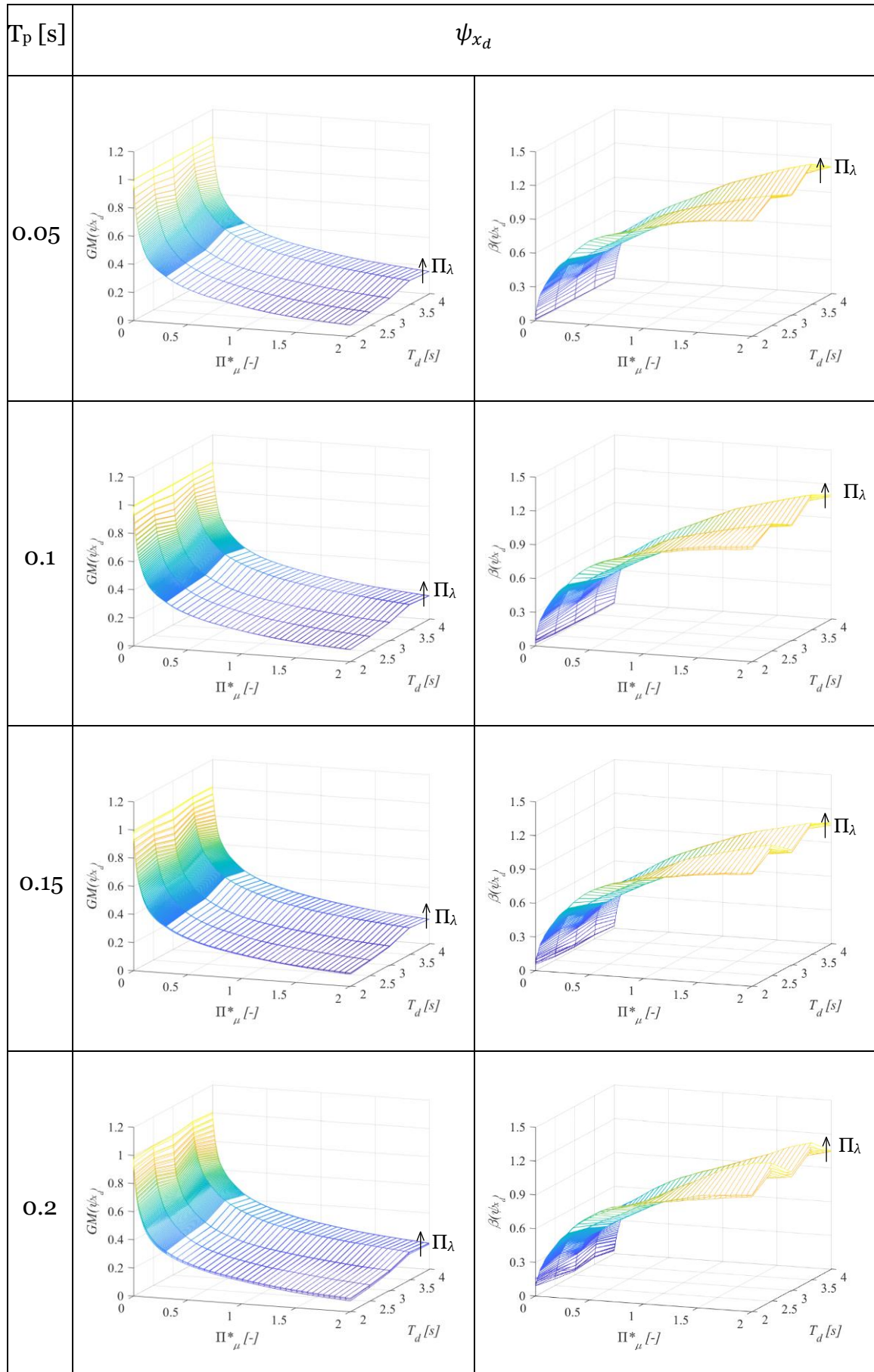


Table 5.4

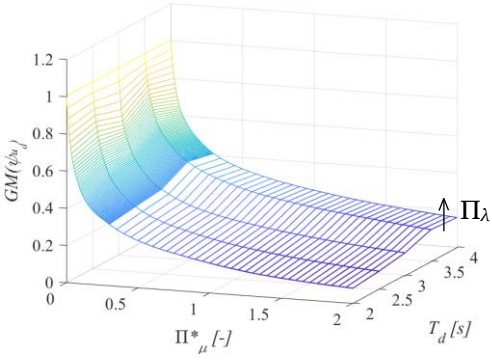
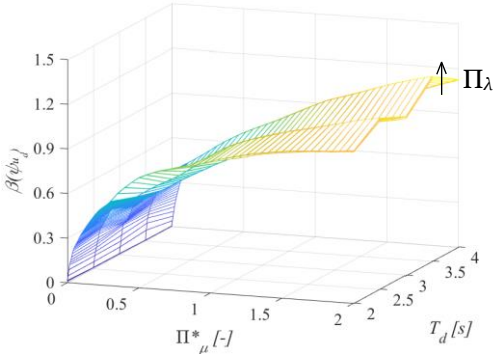
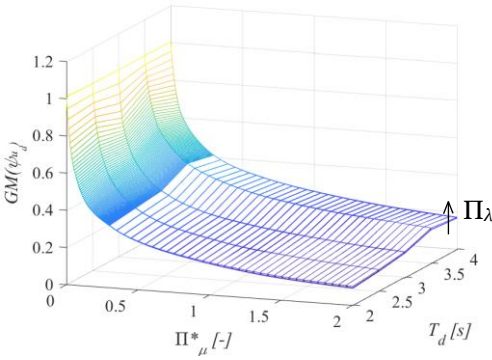
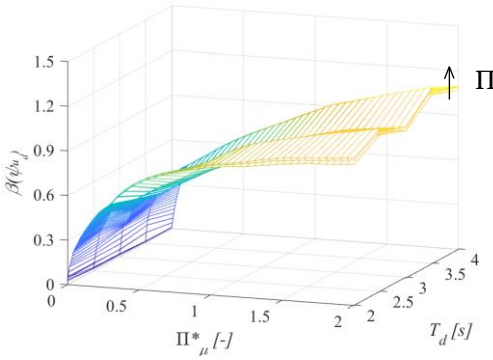
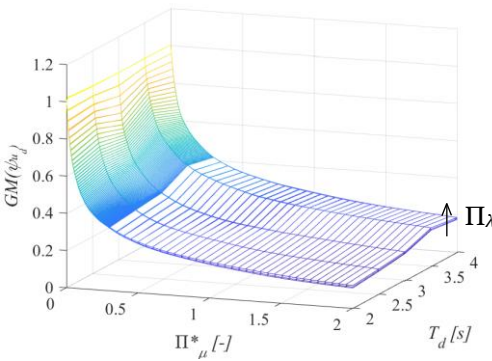
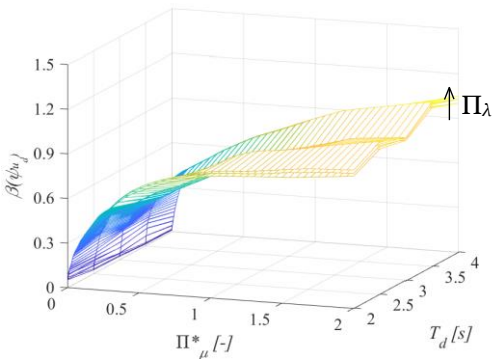
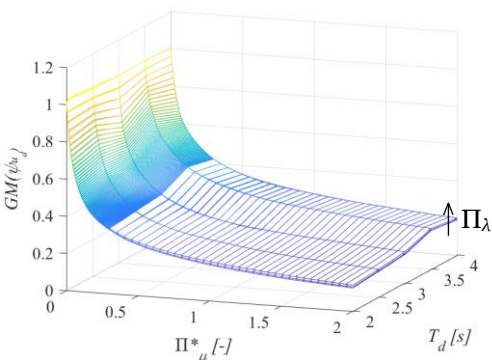
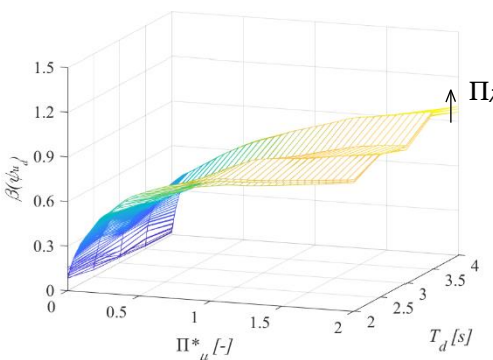
T_p [s]	ψ_{ud}	
0.05		
0.1		
0.15		
0.2		

Table 5.5

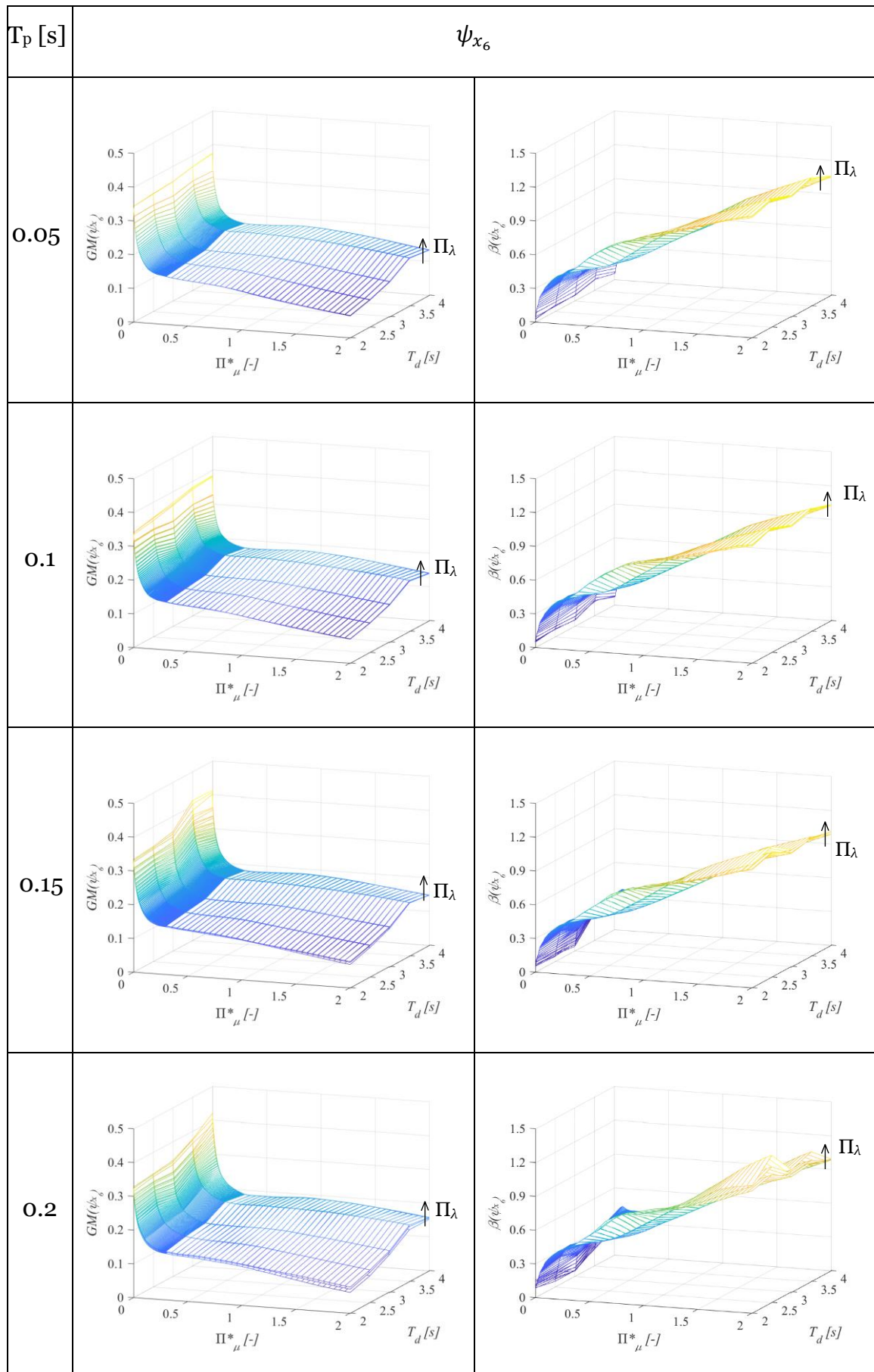


Table 5.6

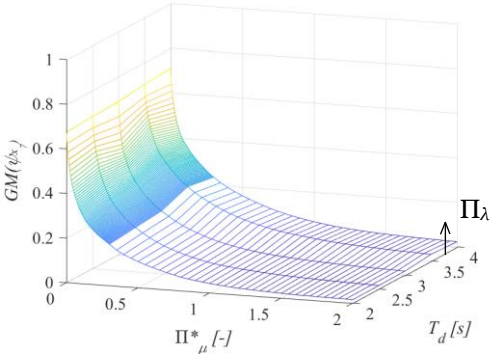
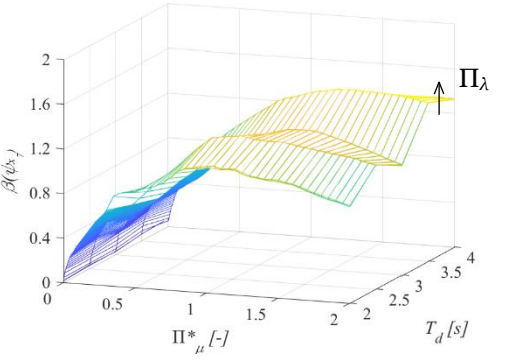
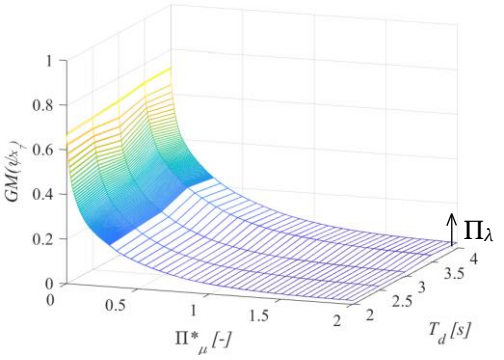
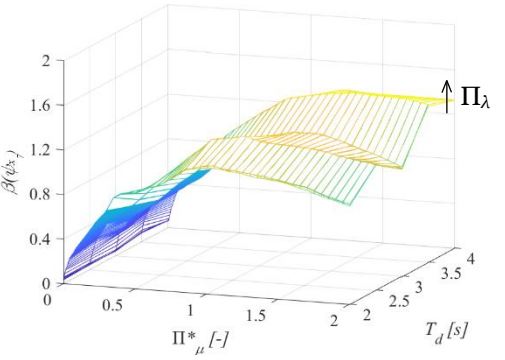
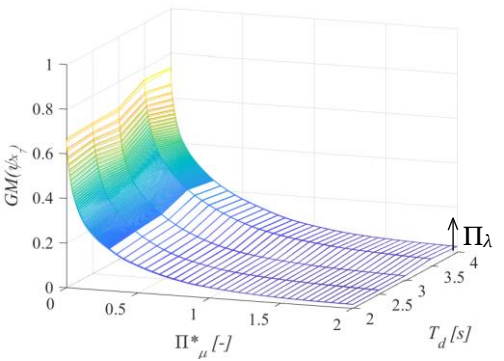
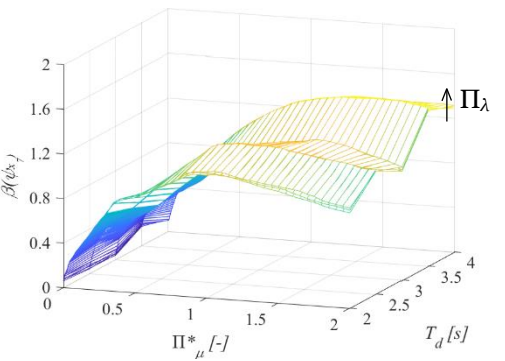
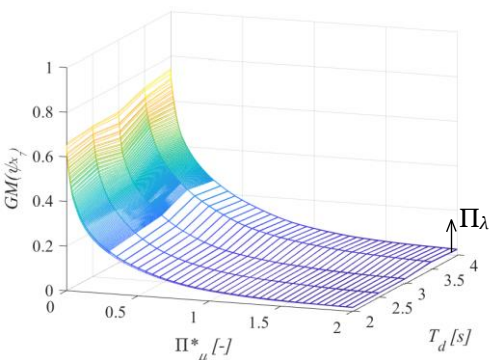
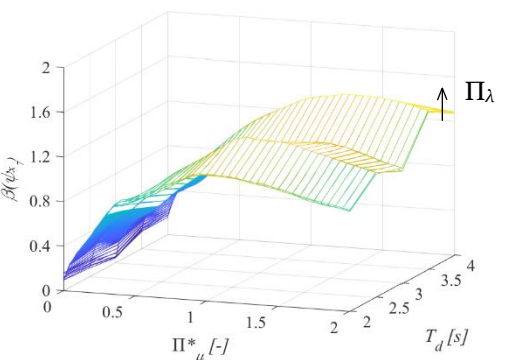
T_p [s]	ψ_{x_7}	
0.05		
0.1		
0.15		
0.2		

Table 5.7

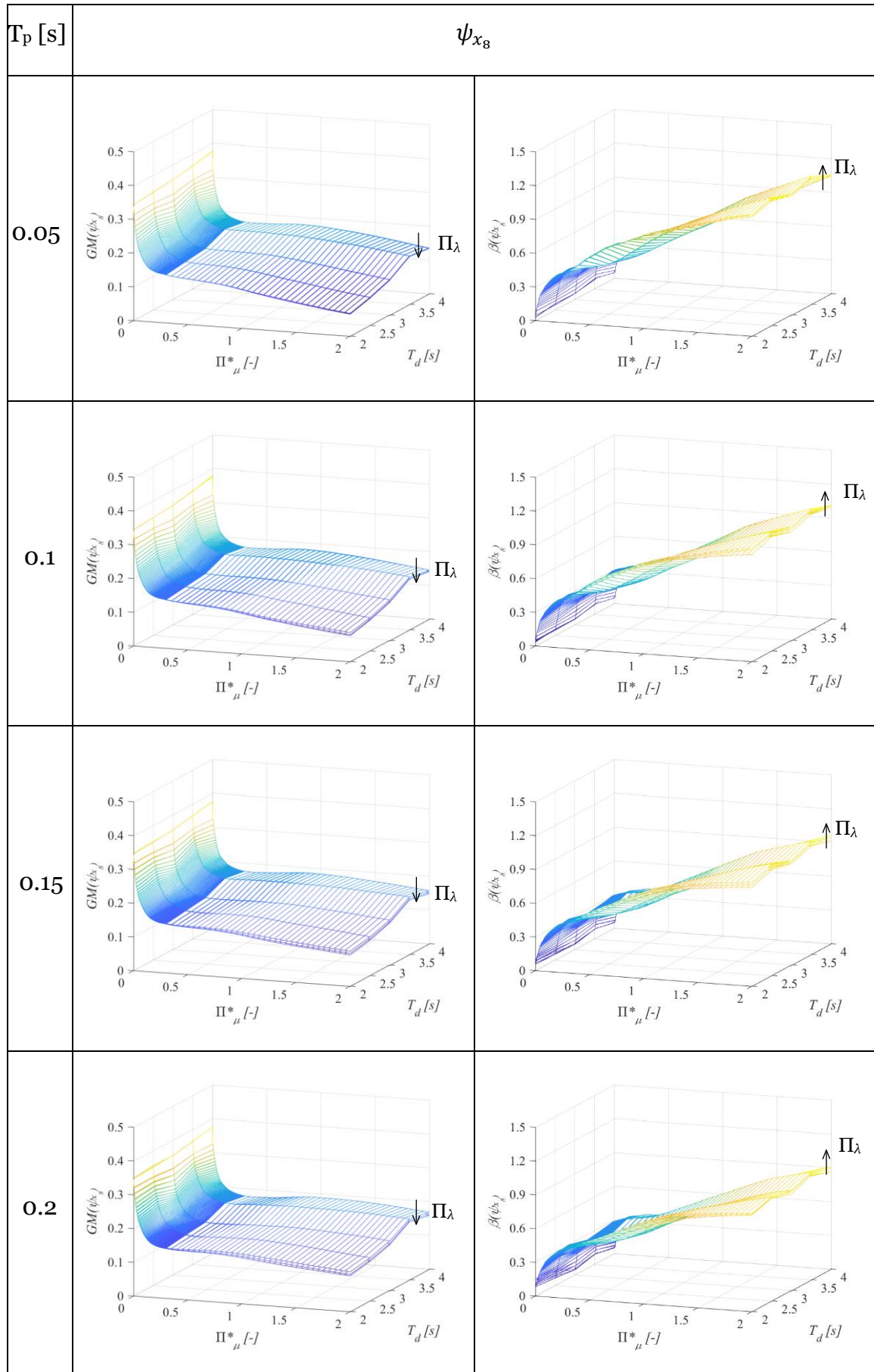


Table 5.8

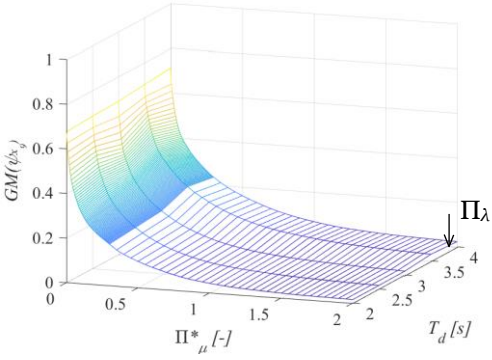
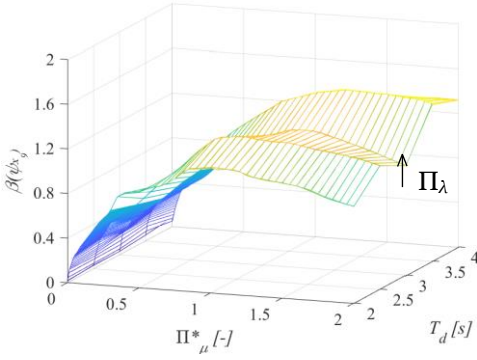
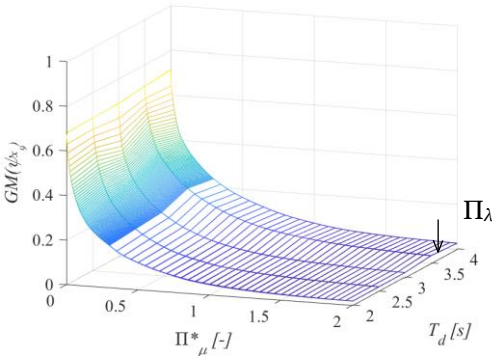
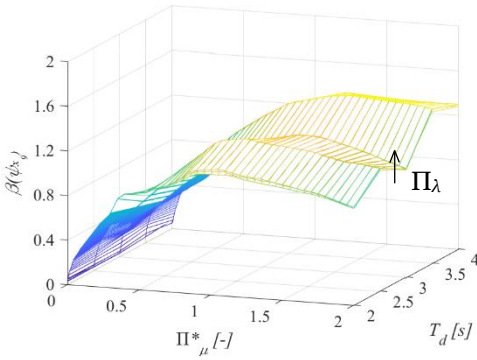
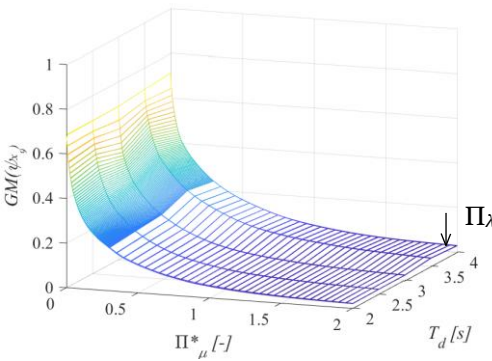
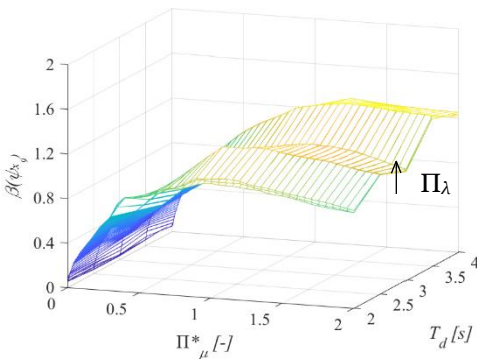
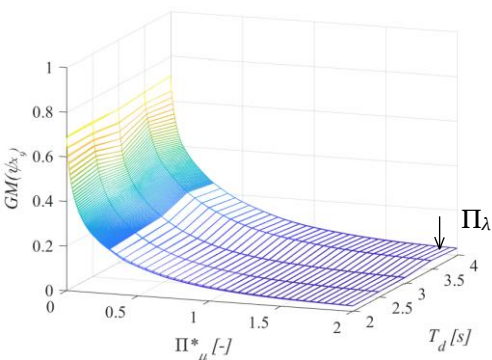
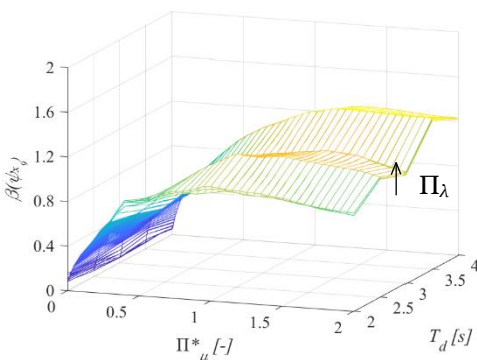
T_p [s]	ψ_{x_9}	
0.05		
0.1		
0.15		
0.2		

Table 5.9

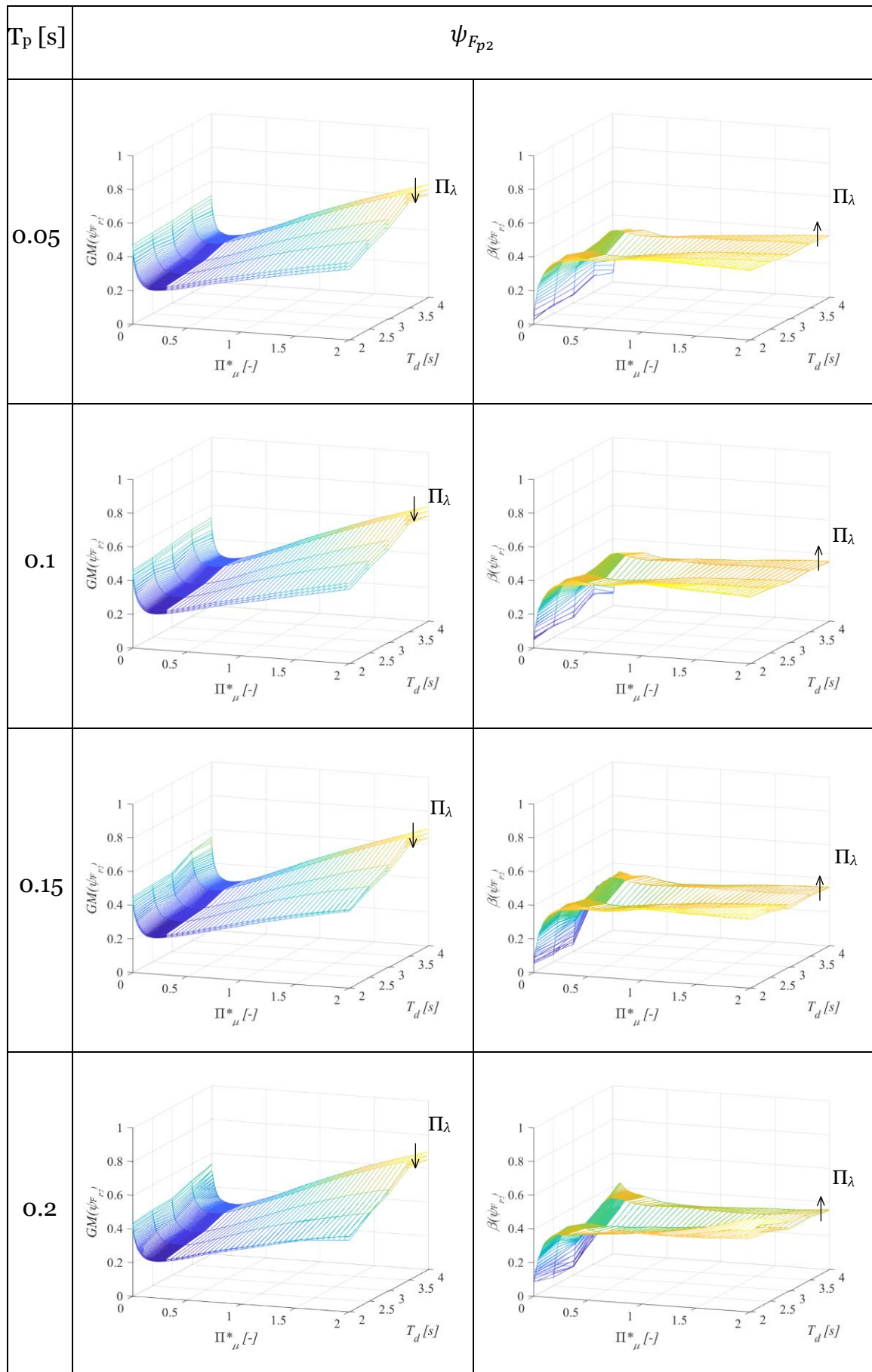


Table 5.10

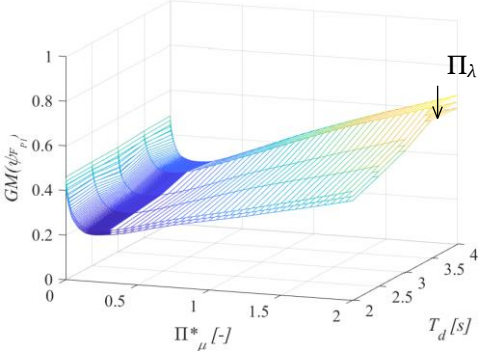
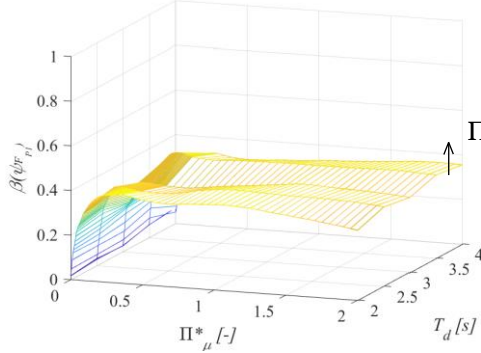
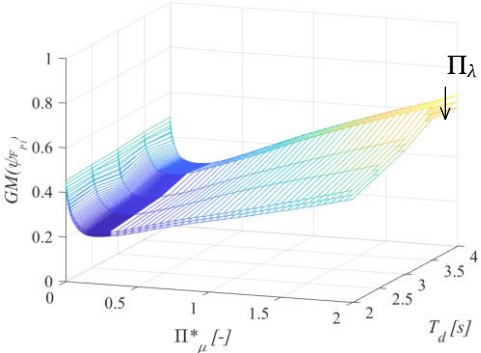
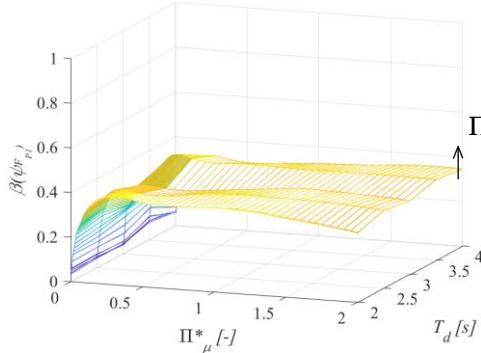
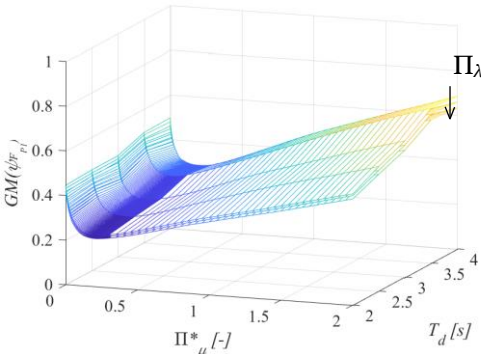
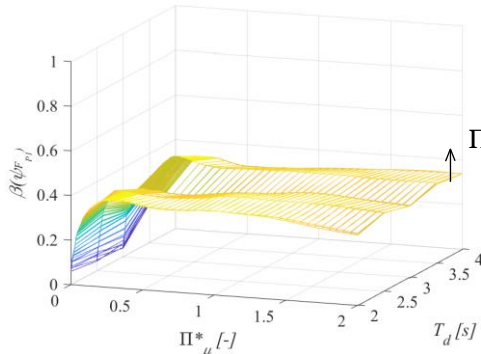
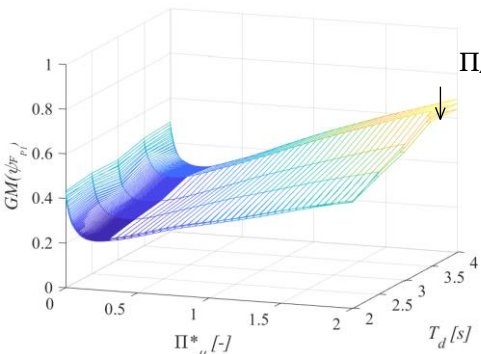
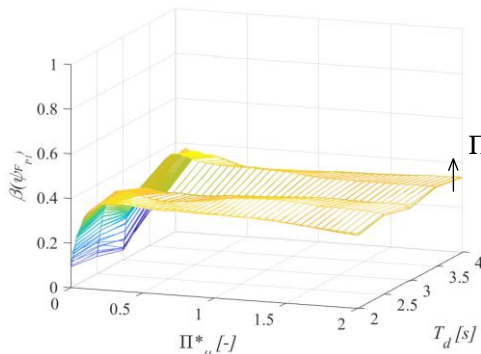
T_p [s]	ψ_{Fp1}	
0.05		
0.1		
0.15		
0.2		

Table 5.11

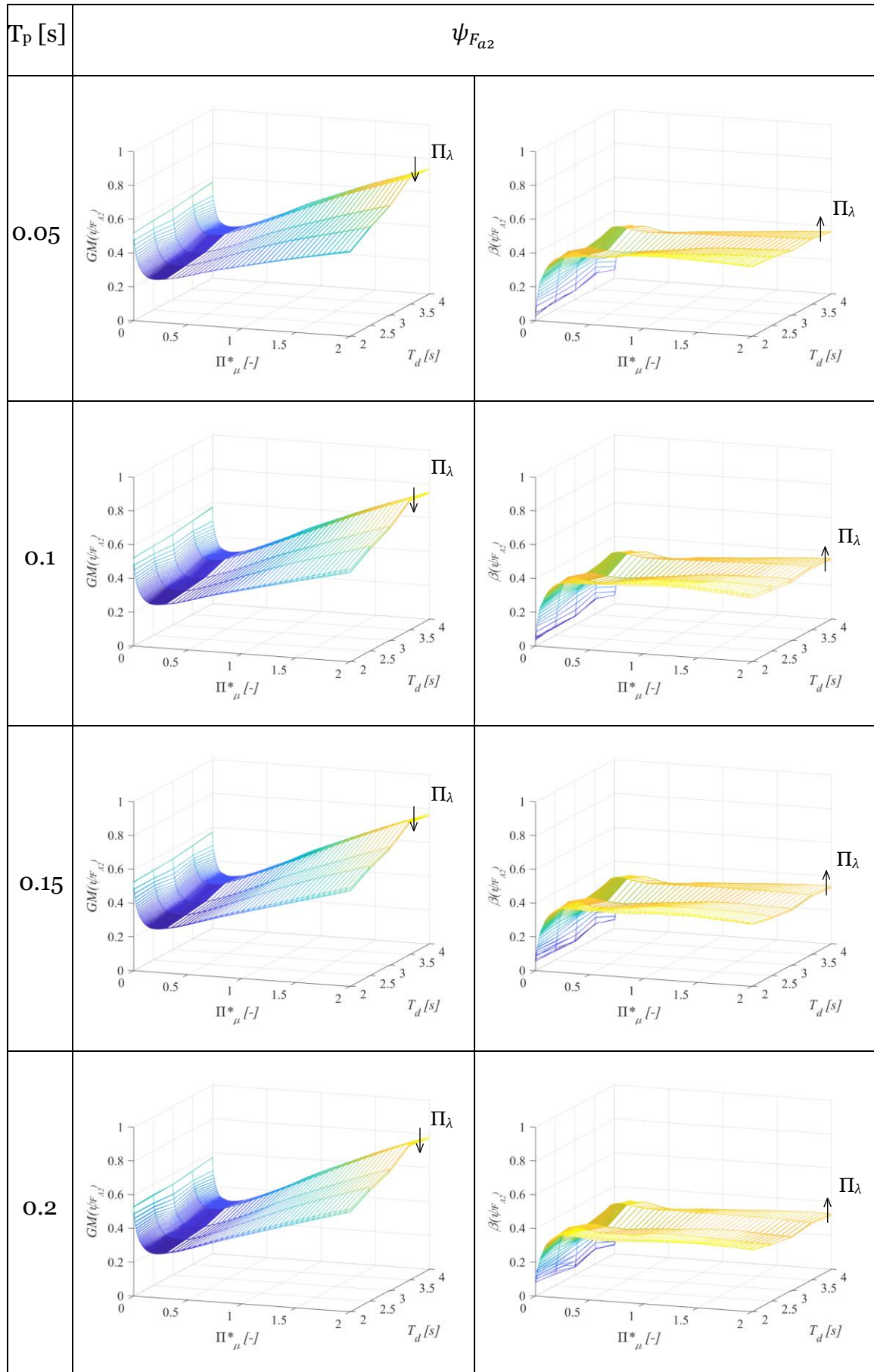


Table 5.12

T_p [s]	ψ_{Fa1}	
0.05		
0.1		
0.15		
0.2		

Table 5.13

5.5.2 Case B

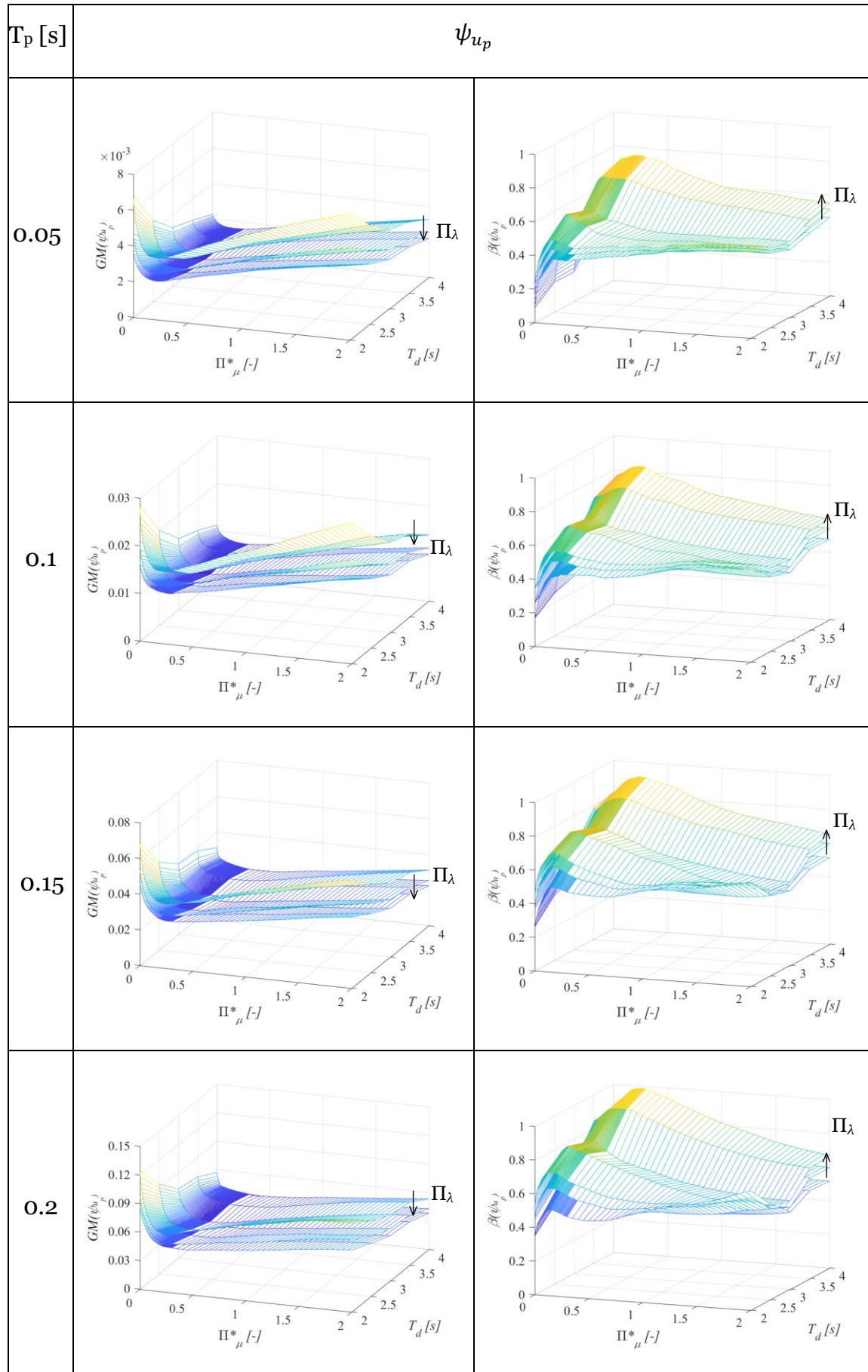


Table 5.14

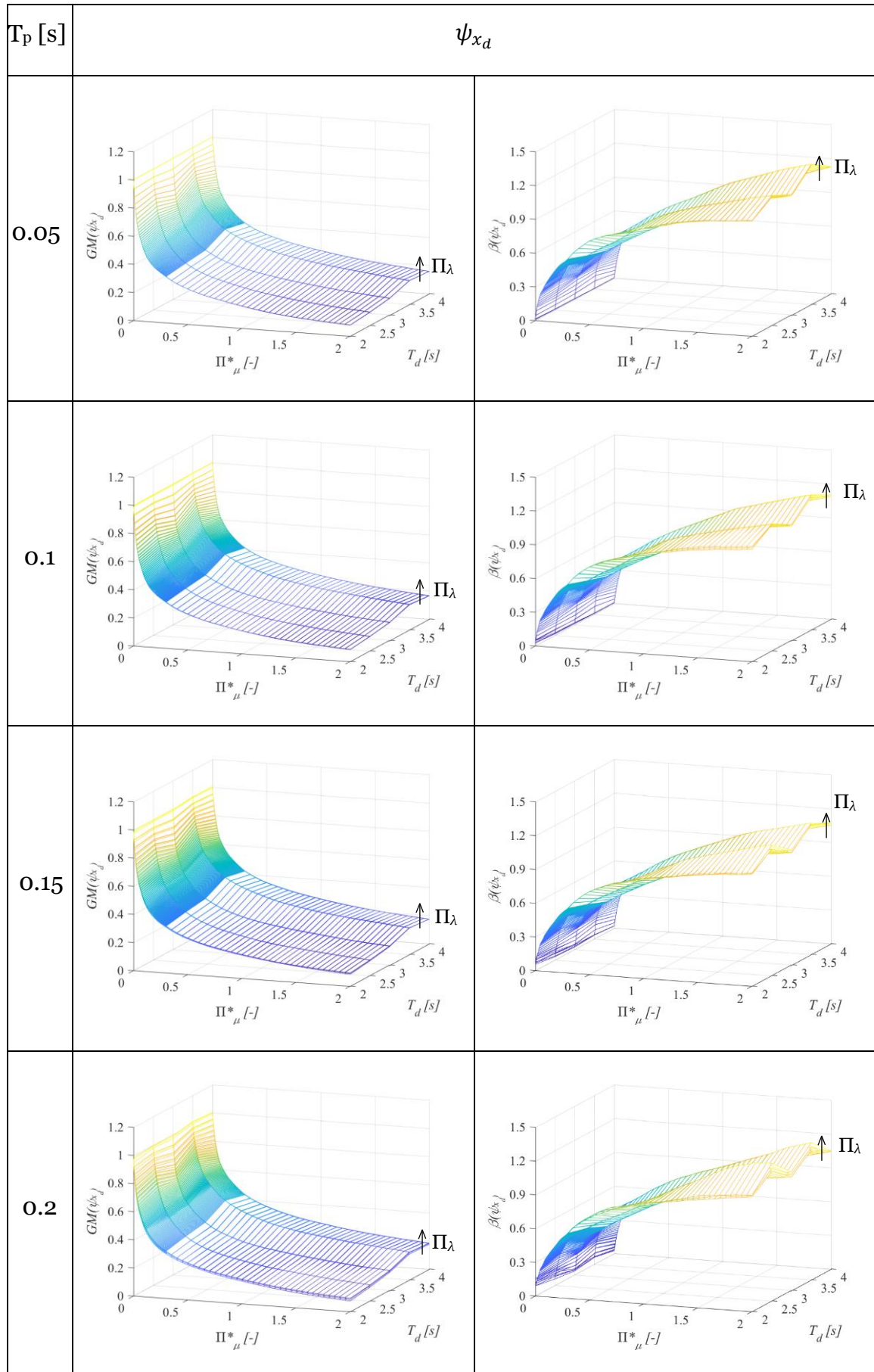


Table 5.15

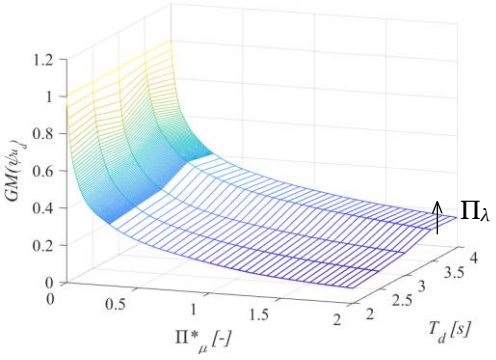
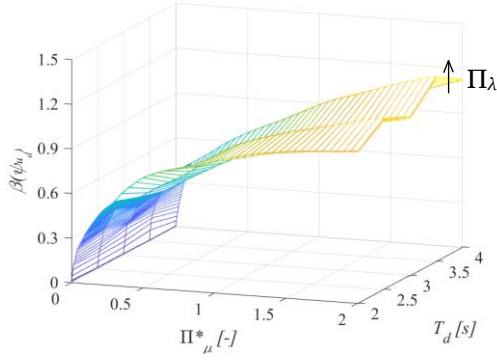
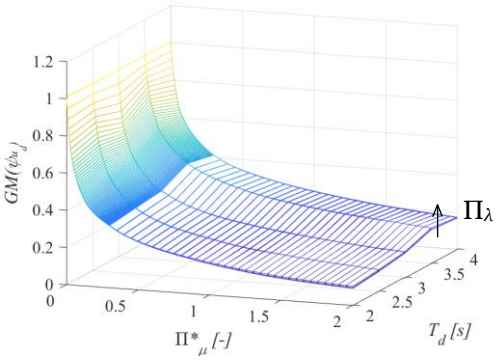
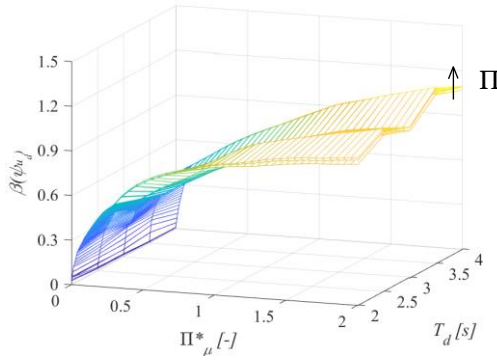
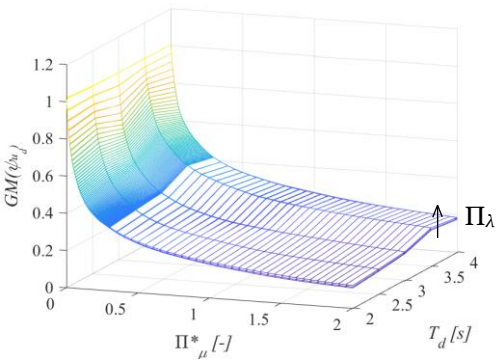
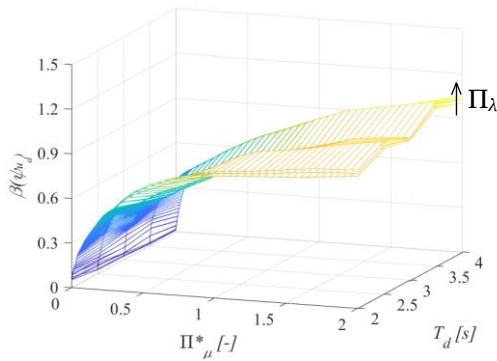
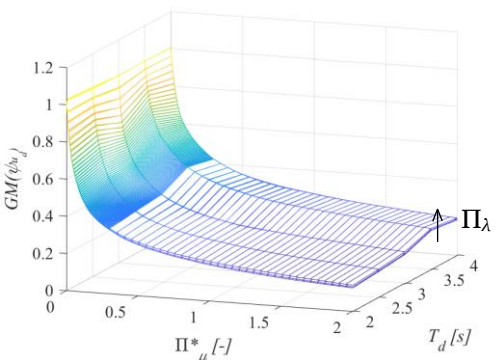
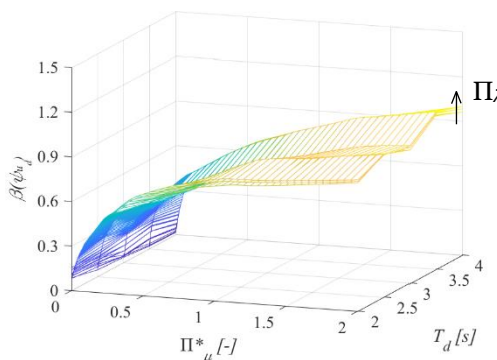
T_p [s]	ψ_{ud}	
0.05		
0.1		
0.15		
0.2		

Table 5.16

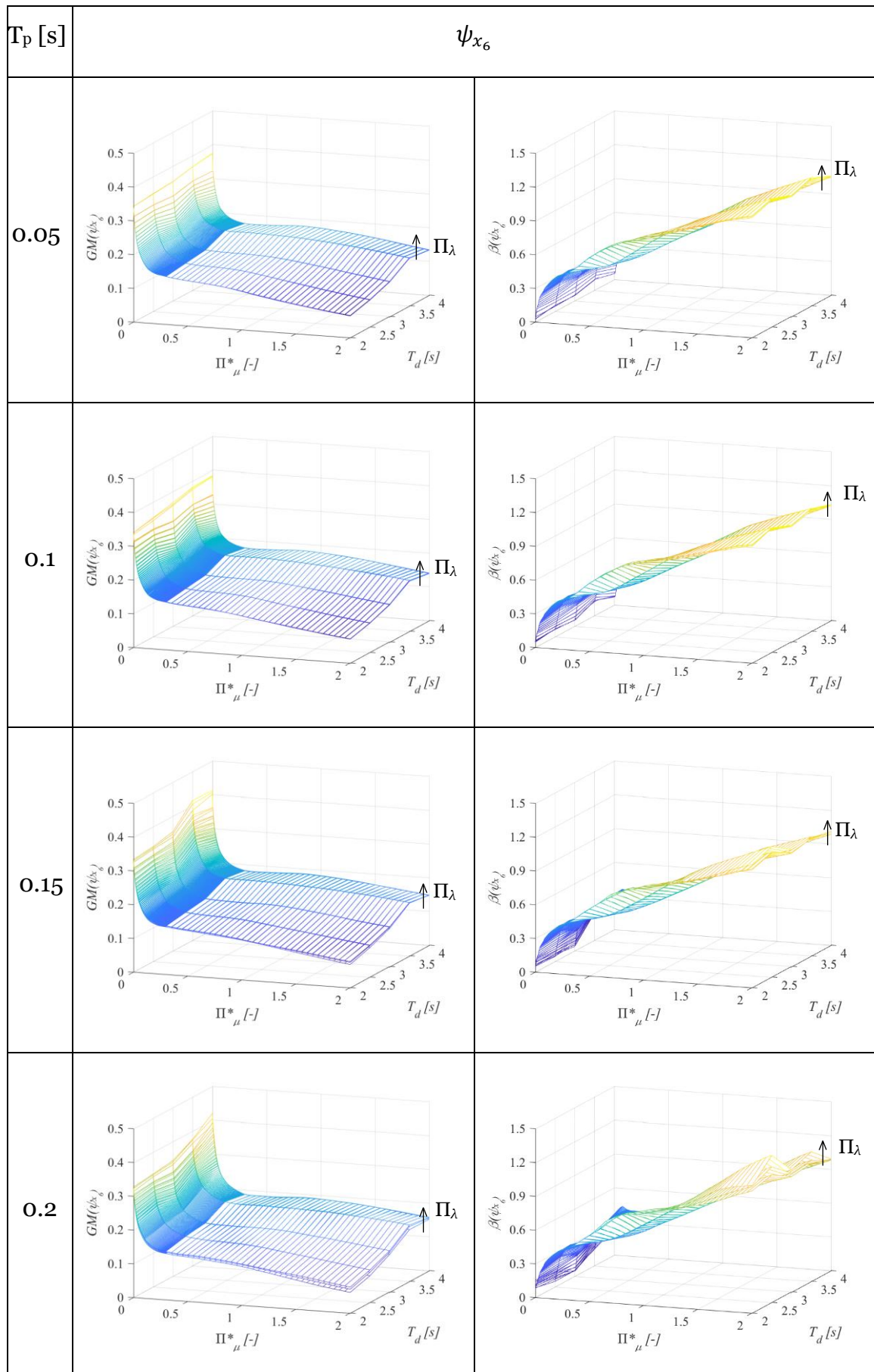


Table 5.17

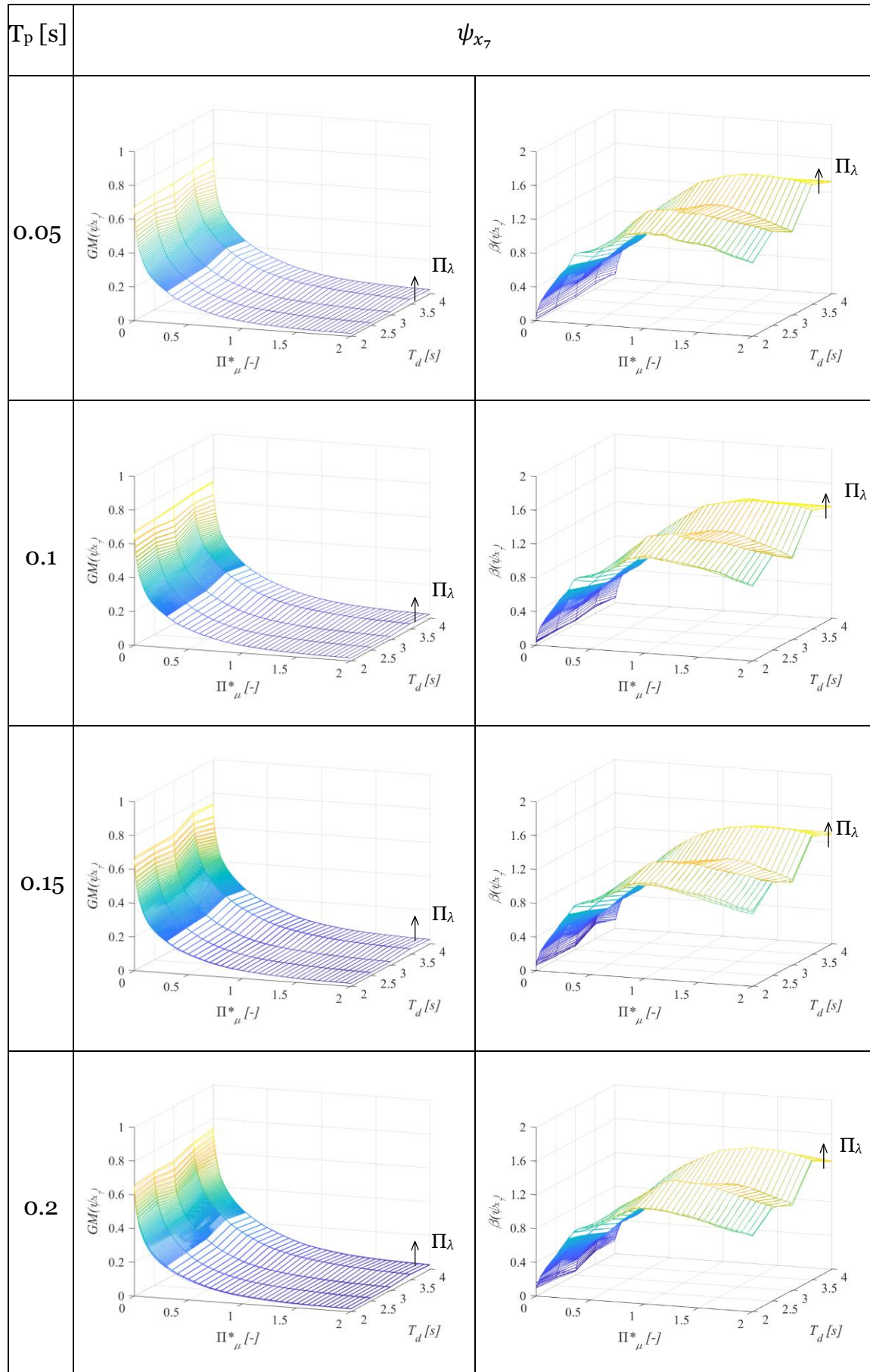


Table 5.18

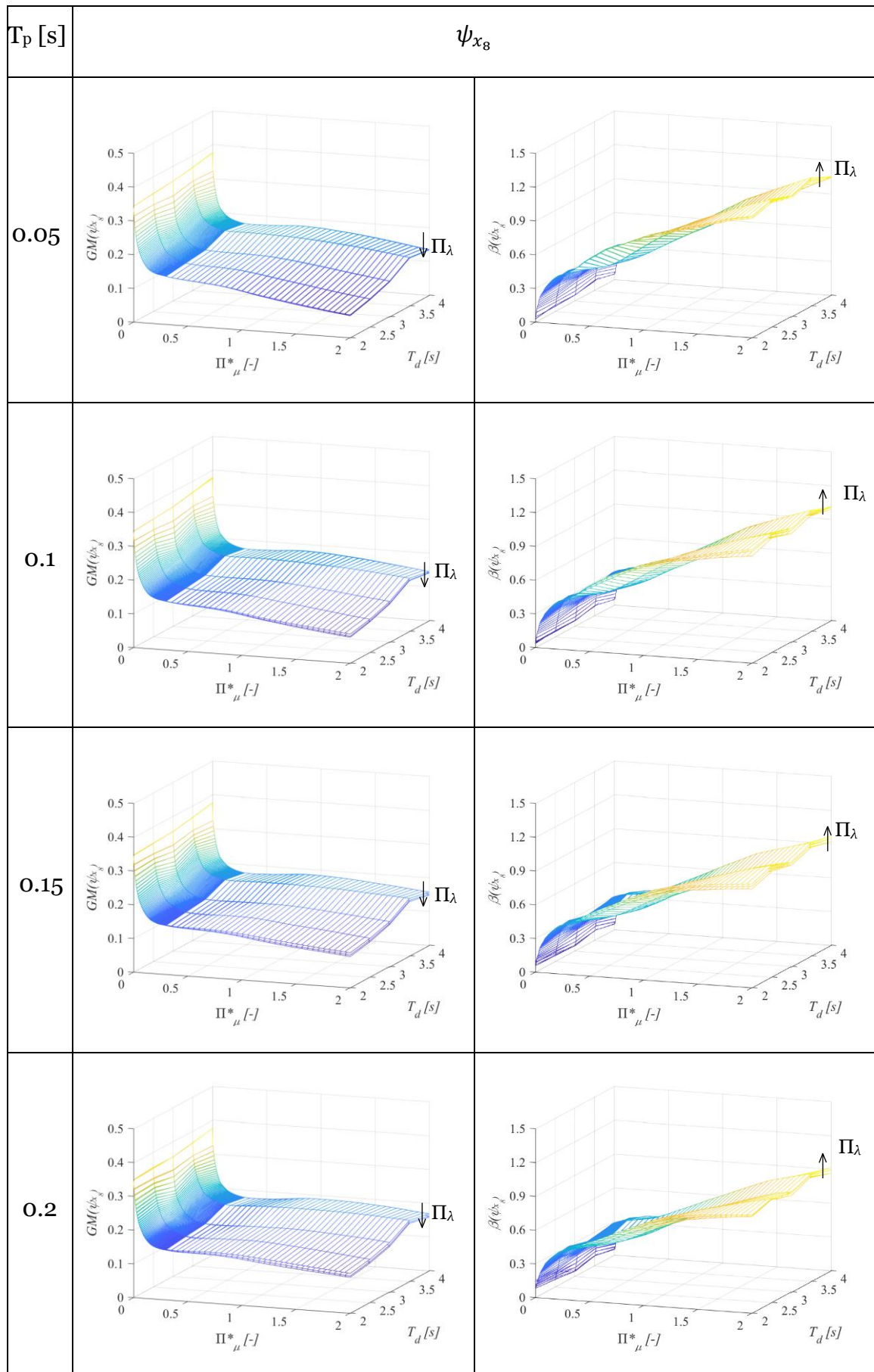


Table 5.19

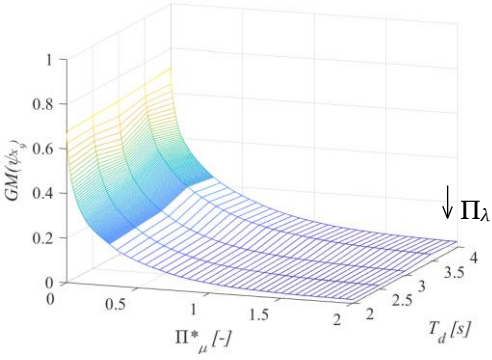
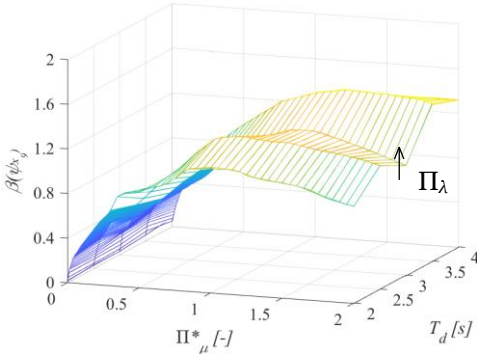
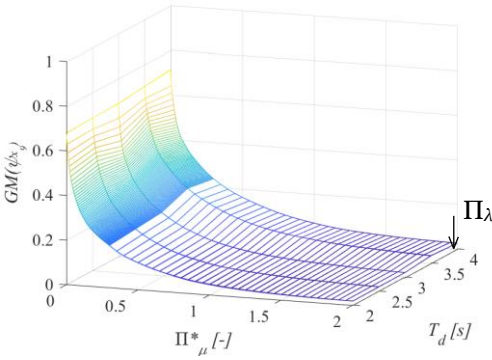
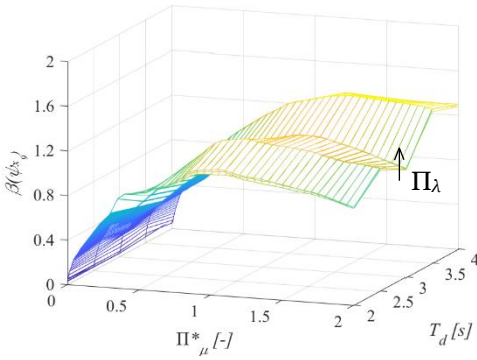
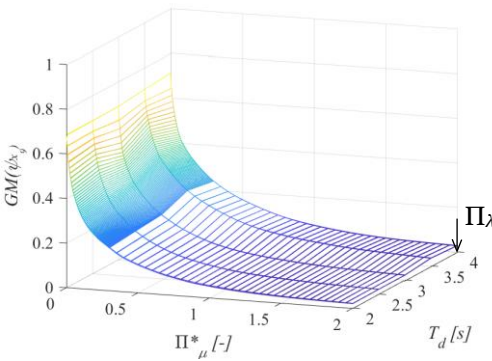
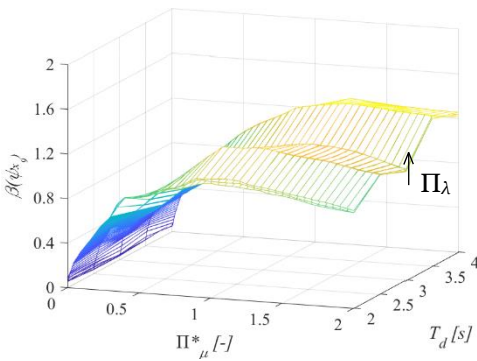
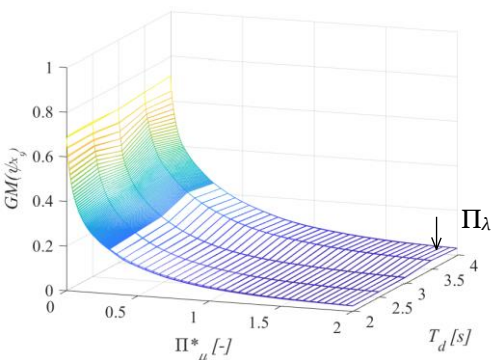
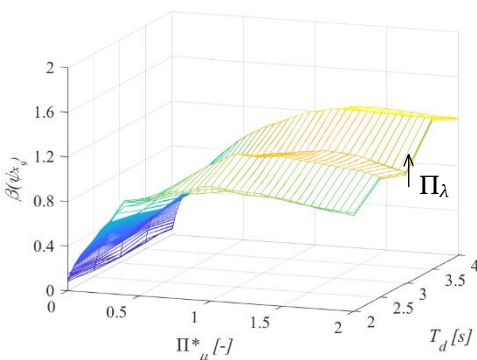
T_p [s]	ψ_{x_9}	
0.05		
0.1		
0.15		
0.2		

Table 5.20

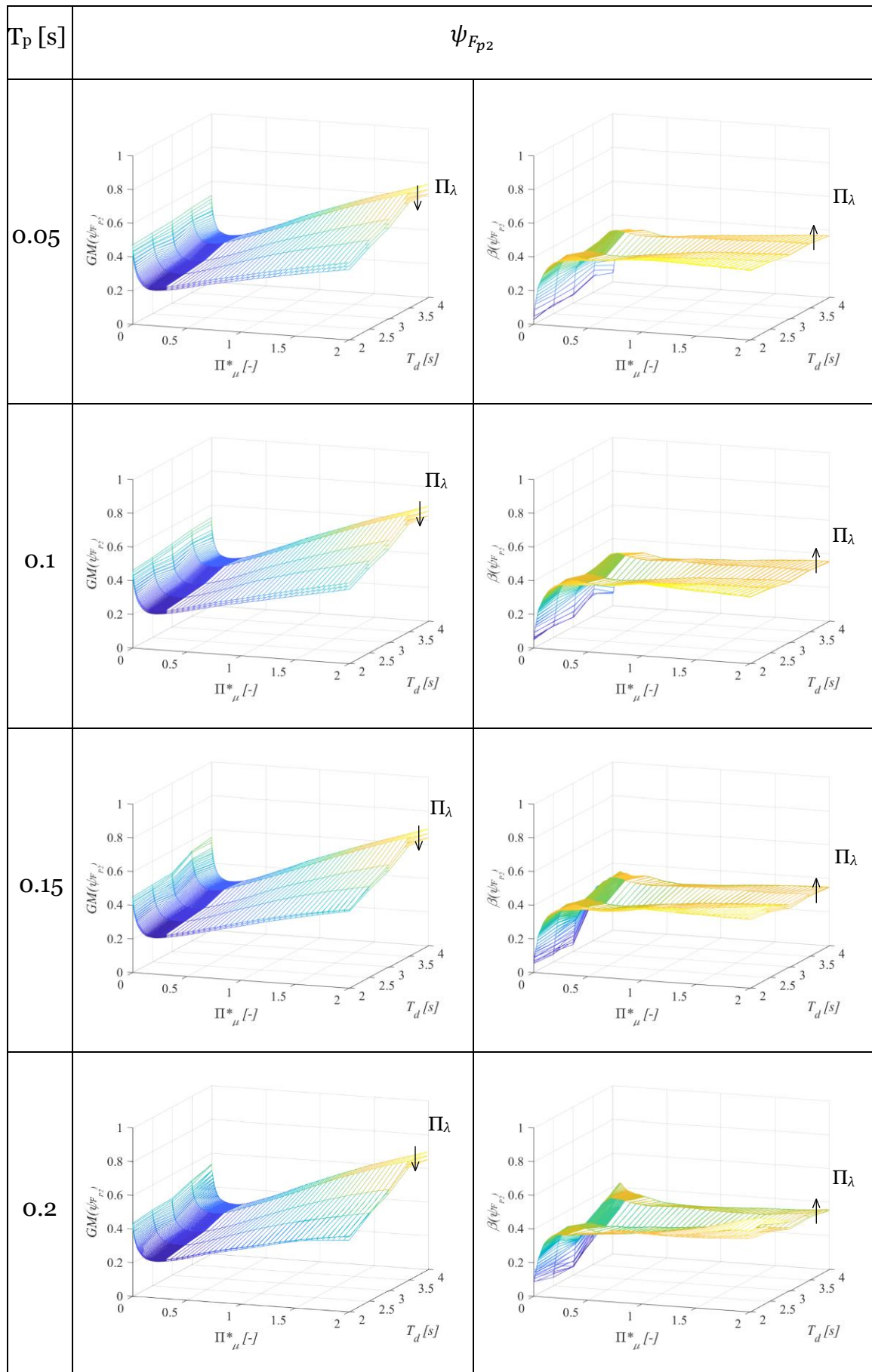


Table 5.21

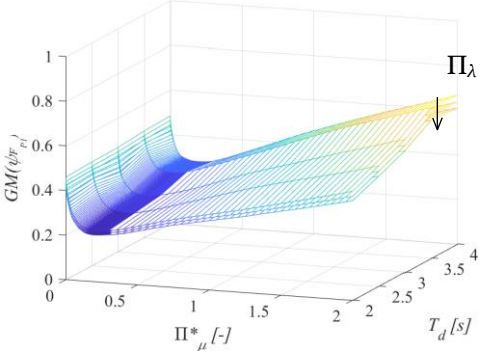
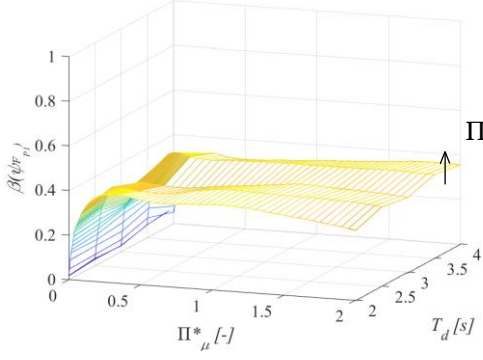
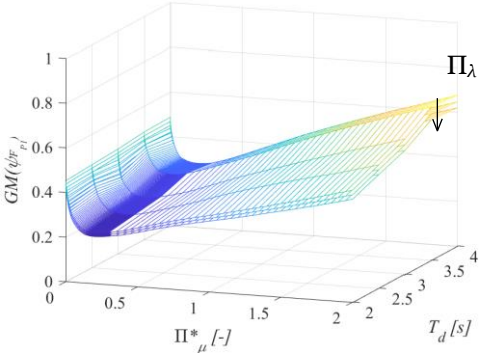
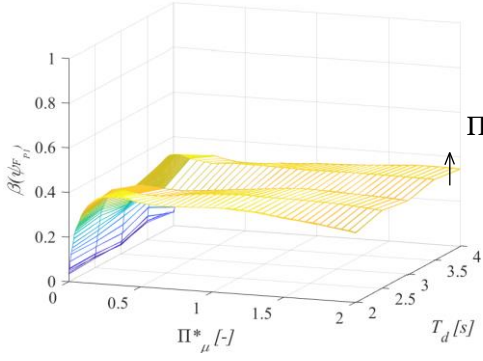
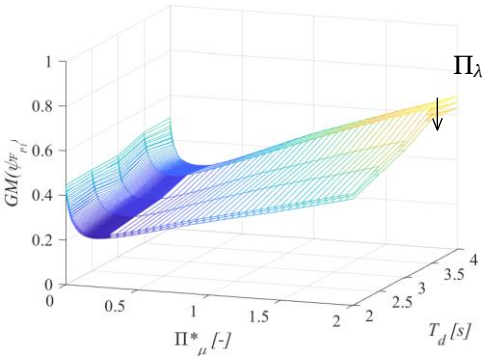
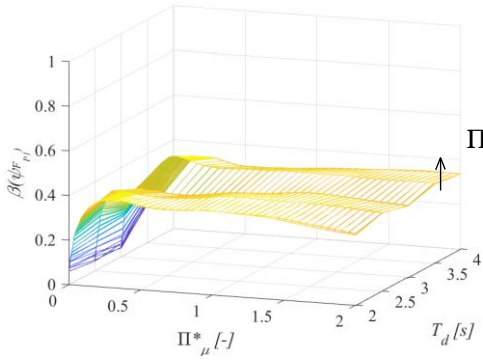
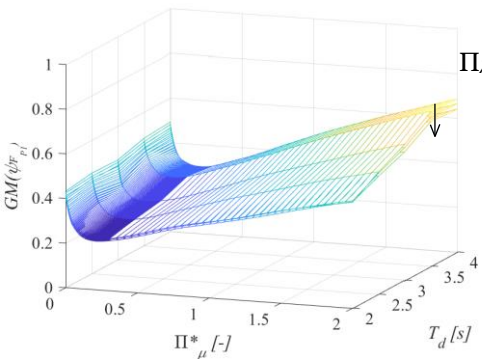
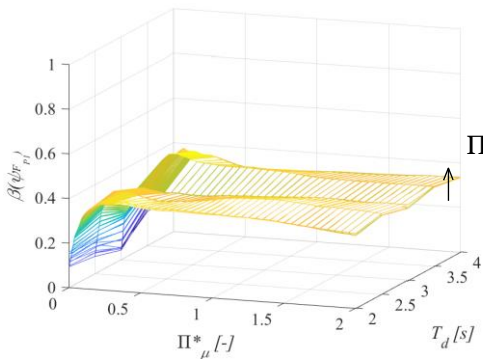
T_p [s]	ψ_{Fp1}	
0.05		
0.1		
0.15		
0.2		

Table 5.22

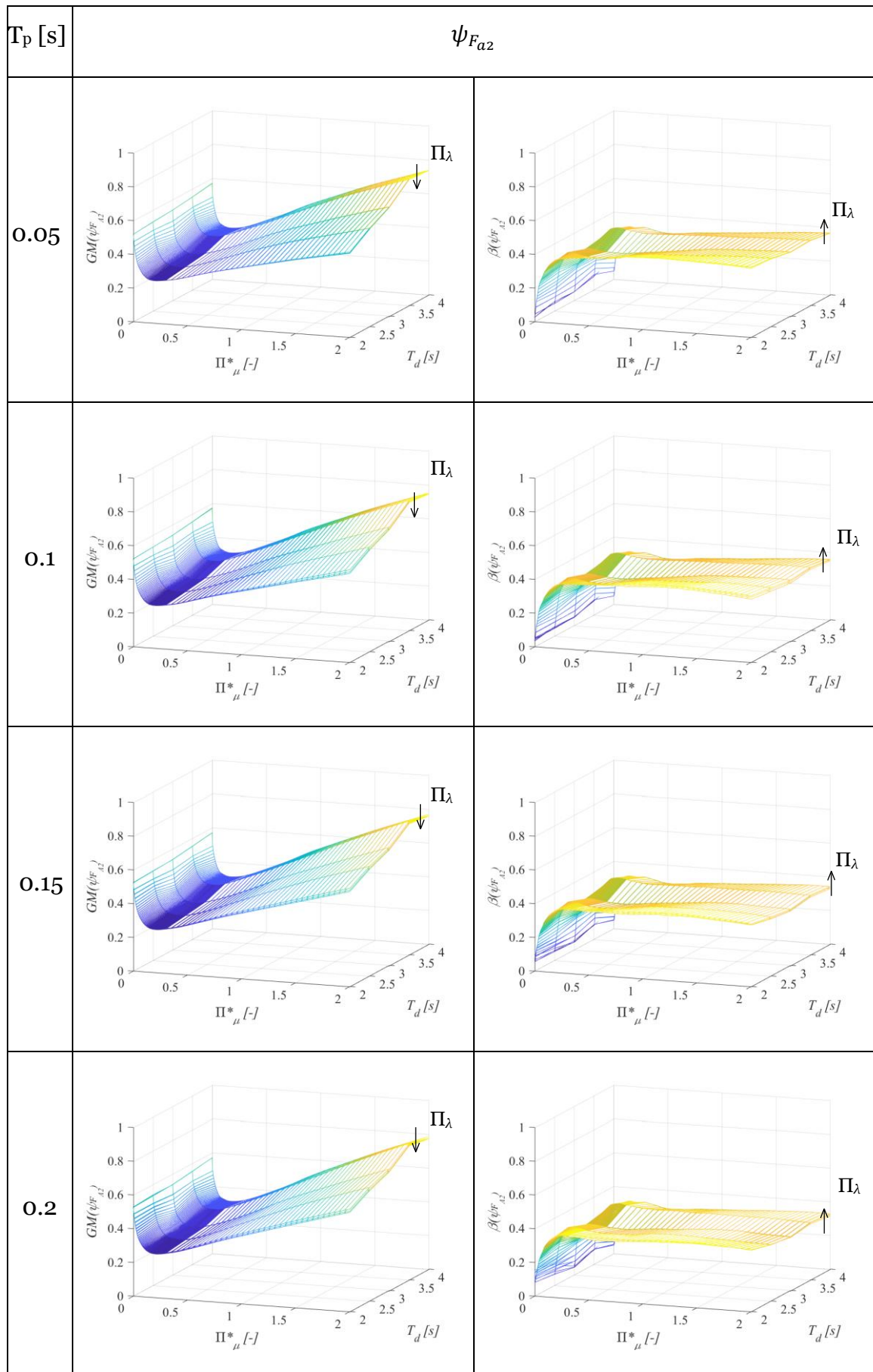


Table 5.23

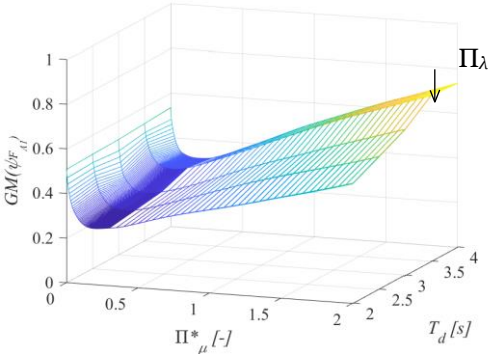
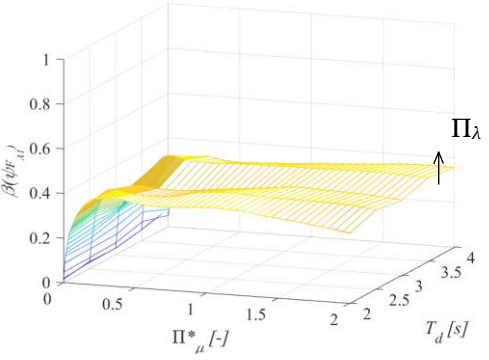
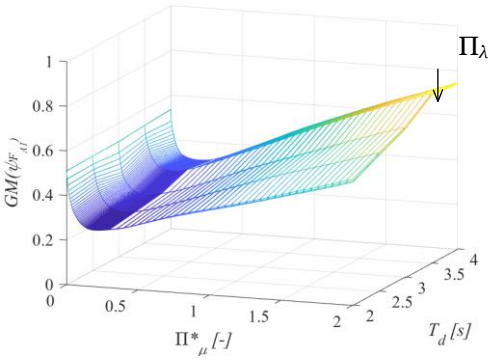
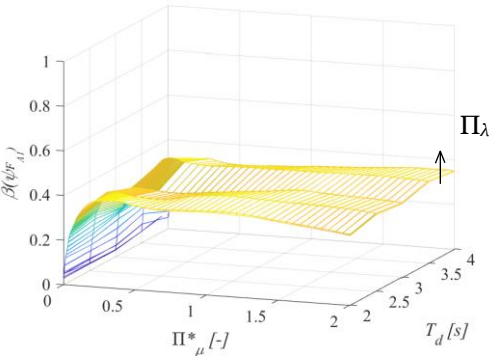
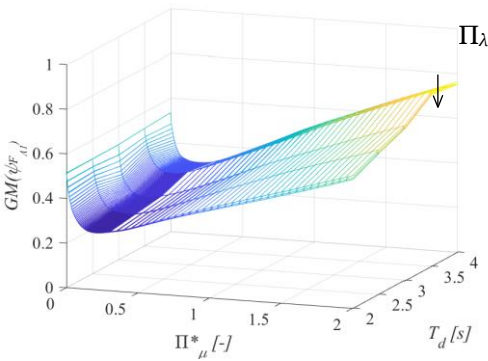
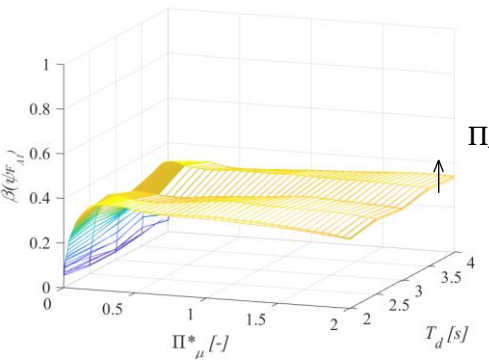
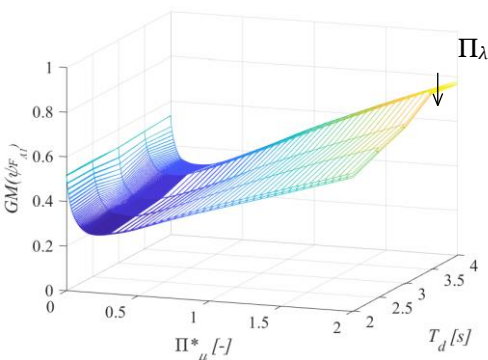
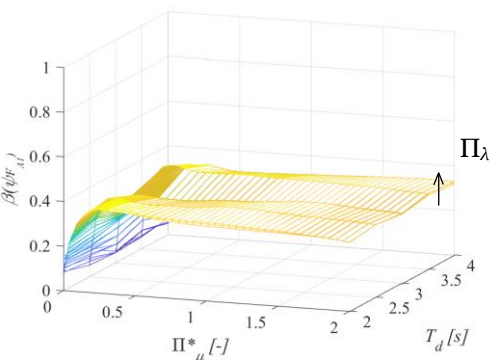
T_p [s]	ψ_{Fa1}	
0.05		
0.1		
0.15		
0.2		

Table 5.24

5.6 Optimal friction values

It must be remarked now that the seismic isolation purpose in bridges is to protect the piers from high shear forces coming from the deck: it is obvious then that the optimal friction values are the ones that give the minimum pier cap displacement.

Each one of the following plots represents the optimum value of normalized friction as function of the pier main period and the deck-pier mass ratio, for a given value of the isolation period.

Once that the value of the ψ_{u_p} distribution parameters for each Π_μ^* are known, it is possible to determine $\Pi_{\mu, optimum}^*$ for the median value, the 16th and 84th percentile of the distribution of ψ_{u_p} , having assumed that the optimal value is the one for which ψ_{u_p} is minimum.

It has to be noted that the ψ_{u_p} sometimes does not have a minimum value respect to the dimensionless friction, but keeps decreasing slowly, or very slowly, for increasing values of Π_μ^* . This occurs generally when the three parameters are the largest possible at the same time. This does not necessarily mean that there are no minimum values of ψ_{u_p} (they could be located beyond $\Pi_\mu^* = 2$), but the fact in these cases the ψ_{u_p} mesh gradient outside the range $\Pi_\mu^* = 0 \div 0.5$ is very close to 0, it is acceptable to search for the minimum only in that range. The difference between the actual minimum, if any, and the picked value, is negligible, and by doing so, unrealistically large values are excluded, making the optimal values interesting for application fields.

5.6.1 Case A

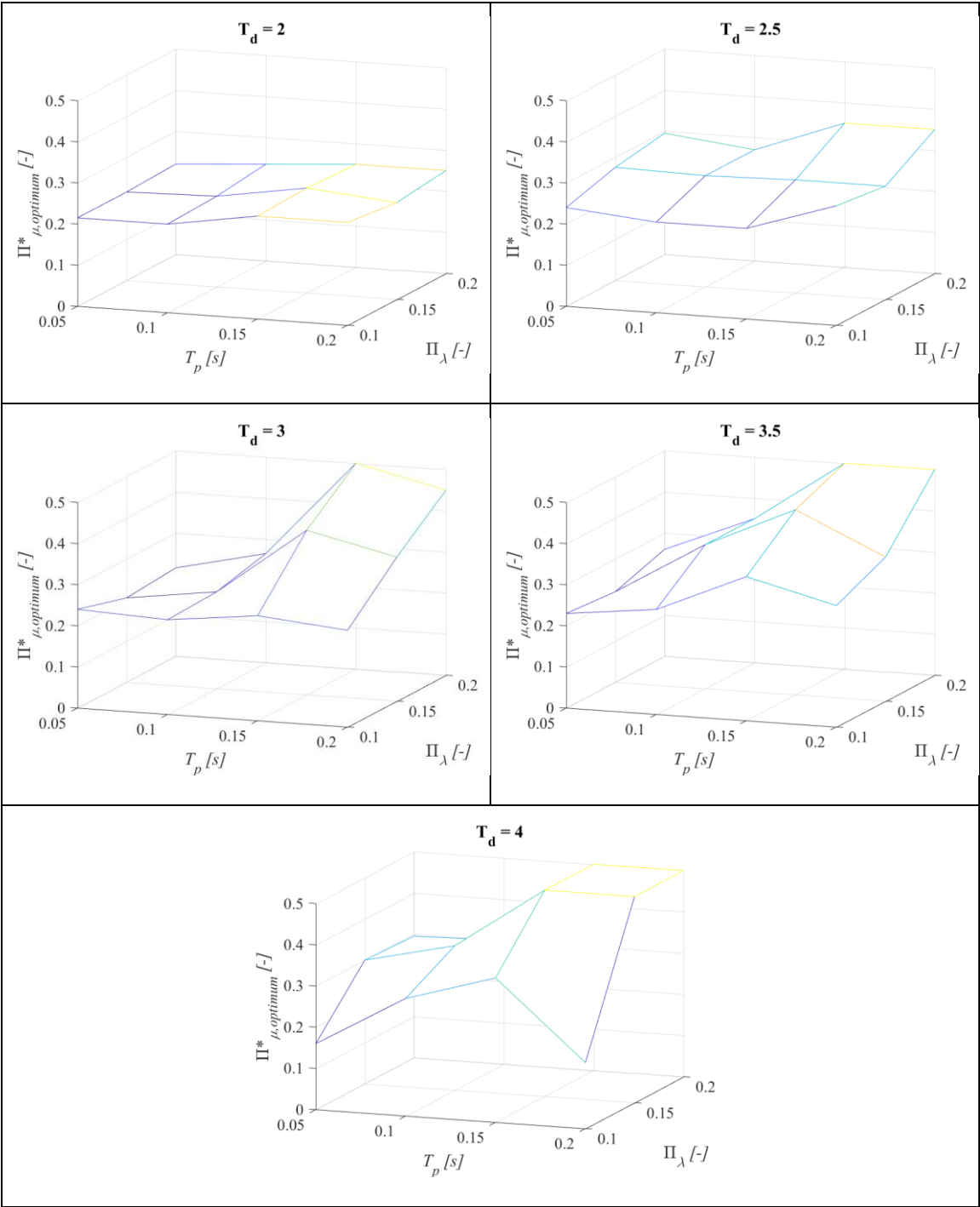


Table 5.25 - Optimal dimensionless friction: median values (case A)

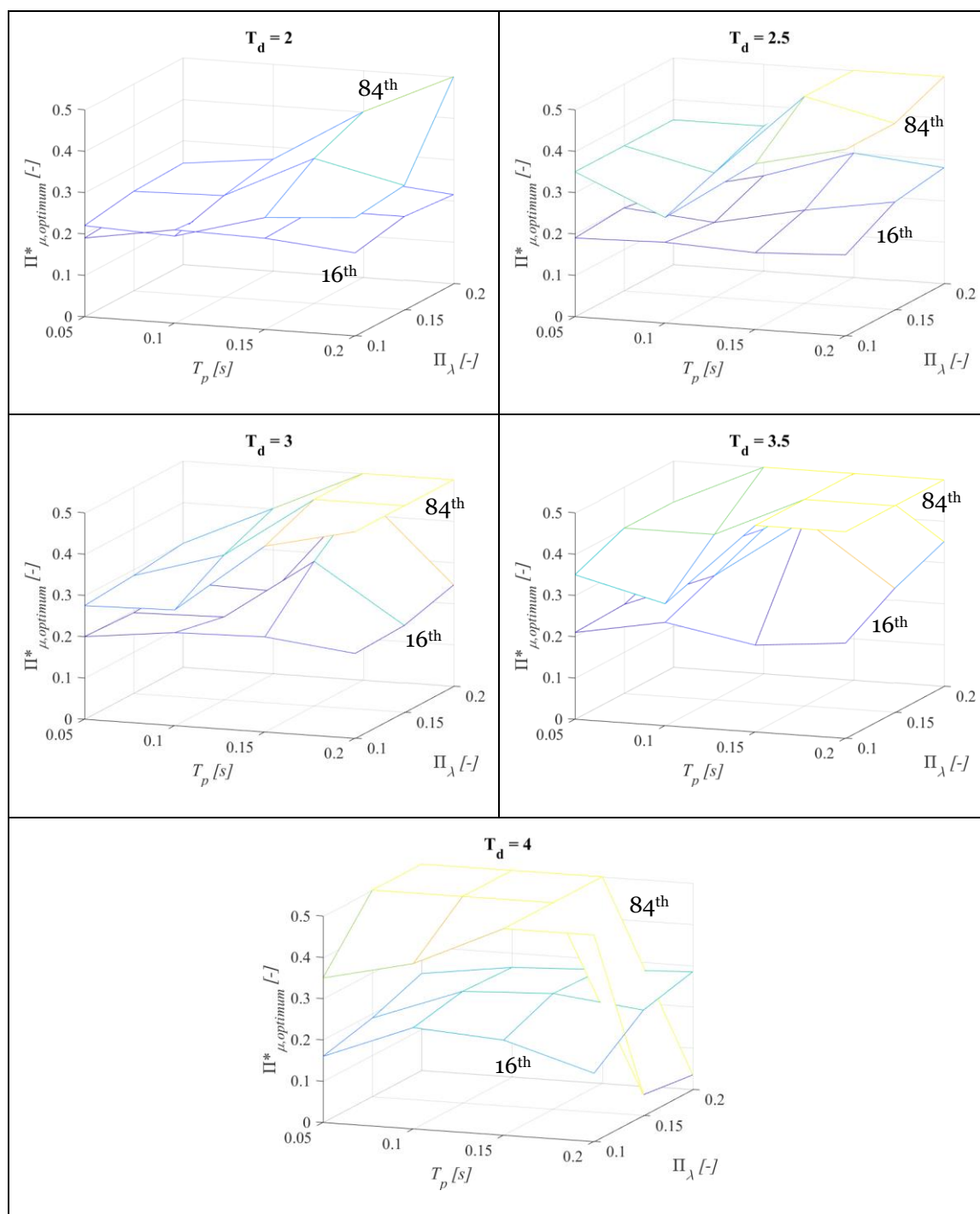


Table 5.26 - Optimal dimensionless friction: 16th and 84th percentiles (case A)

5.6.2Case B

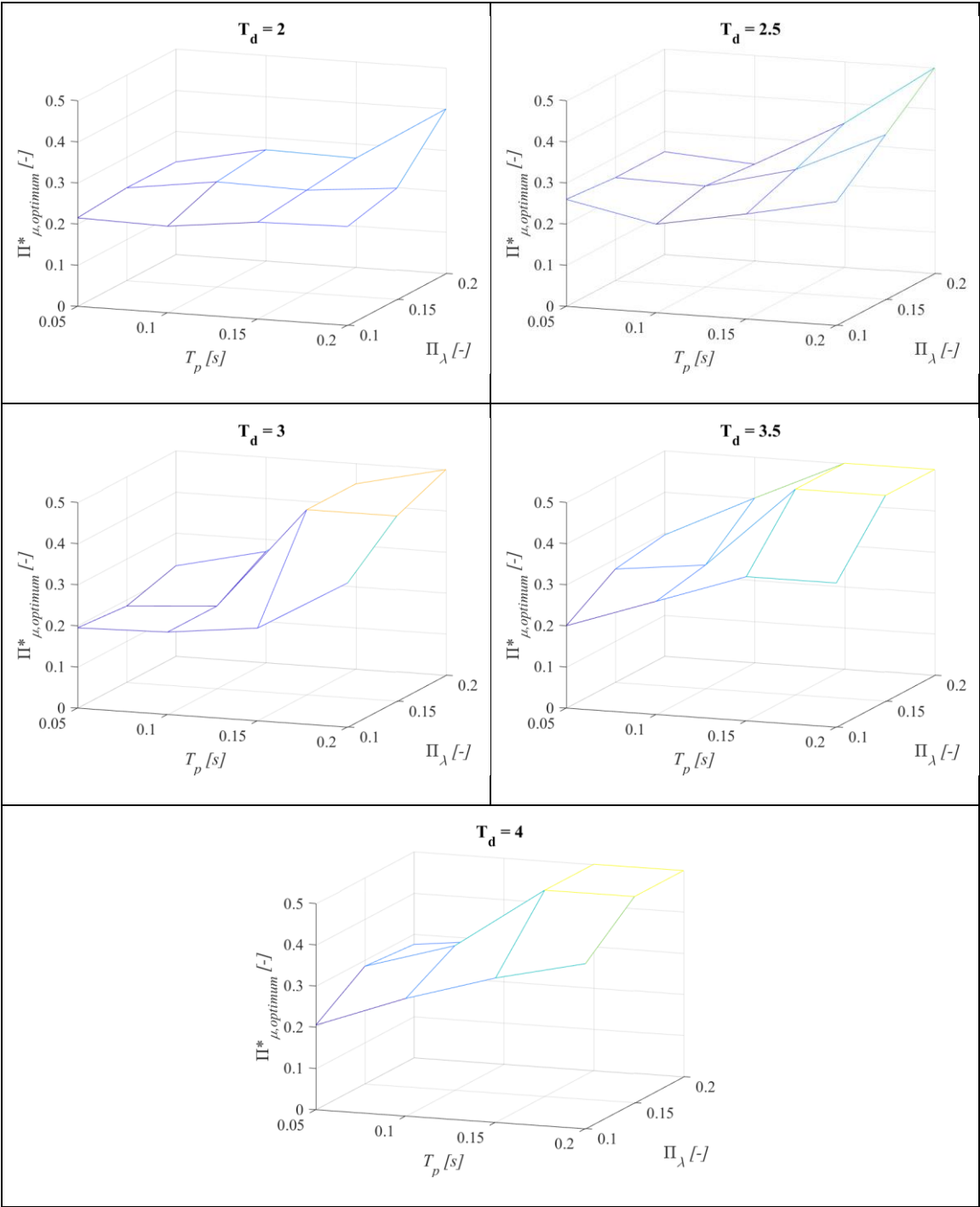


Table 5.27 - Optimal dimensionless friction: median values (case B)

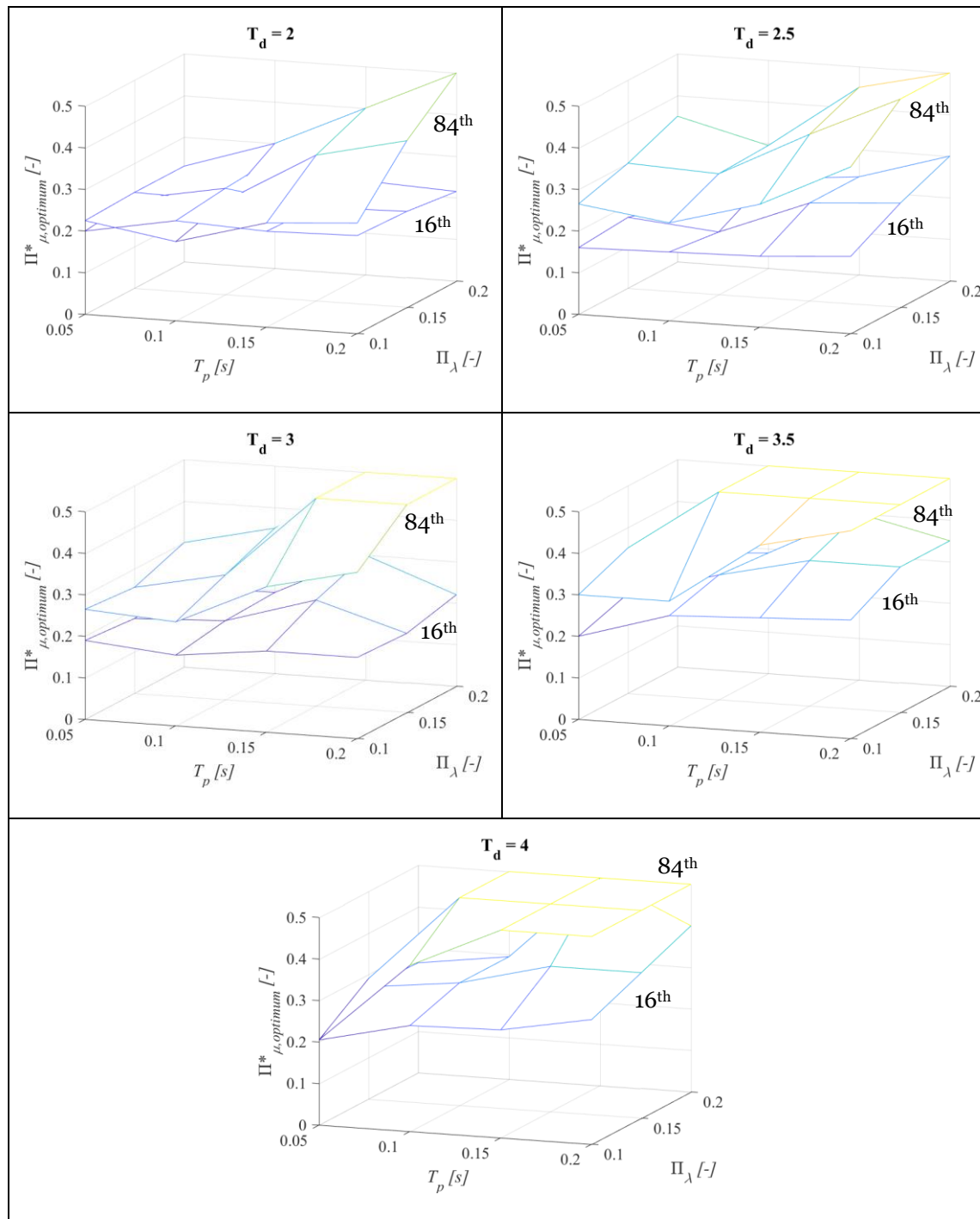


Table 5.28 - Optimal dimensionless friction: 16th and 84th percentile (case B)

5.7 Regression analyses

The optimal values of dimensionless friction found may be used to perform a regression analysis. A set of regression coefficients is then obtained, allowing to yield a closed-form expression that provides an optimal dimensionless friction coefficient for any combination of the main dynamic parameters of a bridge. This

expression may be used in either design or retrofit of an existing bridge, and its reliability is given by the R^2 coefficient.

Regression analysis has been performed in MATLAB with a quadratic regression law (10 coefficients); nevertheless, it is possible to adopt simple artifices to improve the quality of the regression analysis, such as moving a parameter to the denominator, using a square, mixed, exponential or combination of these quantity as a parameter. By doing this, the regression laws that are obtained are in practice more precise than simple quadratic ones.

It is even possible to obtain in the same way closed-form expression for the lateral deformation of both the DCFP sliders, along either the top or the bottom internal surface. This may be useful to estimate the in-plant radii of the isolator surfaces.

5.7.1 Case A

$$\begin{aligned}
 & \Pi_{\mu, opt}^*, \psi_{u_p}(50^{th}, 84^{th}) \\
 &= c_1 + c_2 \frac{T_p}{T_d} + c_3 T_p^2 + c_4 \frac{T_p}{\Pi_\lambda} + c_5 \frac{T_p^3}{T_d} + c_6 \frac{T_p}{T_d \Pi_\lambda} + c_7 \frac{T_p^3}{\Pi_\lambda} \\
 &+ c_8 \left(\frac{T_p}{T_d} \right)^2 + c_9 T_p^4 + c_{10} \left(\frac{T_p}{\Pi_\lambda} \right)^2
 \end{aligned} \tag{5.12a,b,c}$$

$$\begin{aligned}
 & \Pi_{\mu, opt}^*, \psi_{u_p}(16^{th}) \\
 &= c_1 + c_2 T_d + c_3 T_p + c_4 \Pi_\lambda + c_5 T_d T_p + c_6 T_d \Pi_\lambda + c_7 T_p \Pi_\lambda \\
 &+ c_8 T_d^2 + c_9 T_p^2 + c_{10} \Pi_\lambda^2
 \end{aligned}$$

	$\Pi_{\mu, opt}^*(50^{th})$	$\psi_{u_p}(50^{th})$	$\Pi_{\mu, opt}^*(84^{th})$	$\psi_{u_p}(84^{th})$	$\Pi_{\mu, opt}^*(16^{th})$	$\psi_{u_p}(16^{th})$
R^2	0.8301	0.9956	0.6670	0.9865	0.5167	0.9847
c_1	0.3554	0.0020	0.4128	0.0071	-0.0713	0.0198
c_2	-7.1923	-0.2496	2.4285	-0.8336	0.1261	-0.0101
c_3	34.3154	1.2284	16.0888	3.4910	1.4370	0.2009
c_4	-0.2680	-0.0047	-0.2993	-0.0117	-0.3875	-0.1440
c_5	-43.2117	-14.6796	1091.0823	-48.4532	0.0967	-0.0410
c_6	5.8144	0.2656	-7.4519	0.3327	0.3675	0.0274
c_7	-7.2993	-0.2839	7.9592	-0.8464	5.0600	-0.4292
c_8	-19.2474	5.0652	-221.9676	16.2905	-0.0280	0.0013
c_9	-269.0404	13.0834	-1509.0221	46.4419	-8.6000	0.5172
c_{10}	-0.0071	0.0012	0.1853	0.0060	-2.2500	0.2714

Table 5.29 - Regression analysis results (friction and pier cap displacement - A)

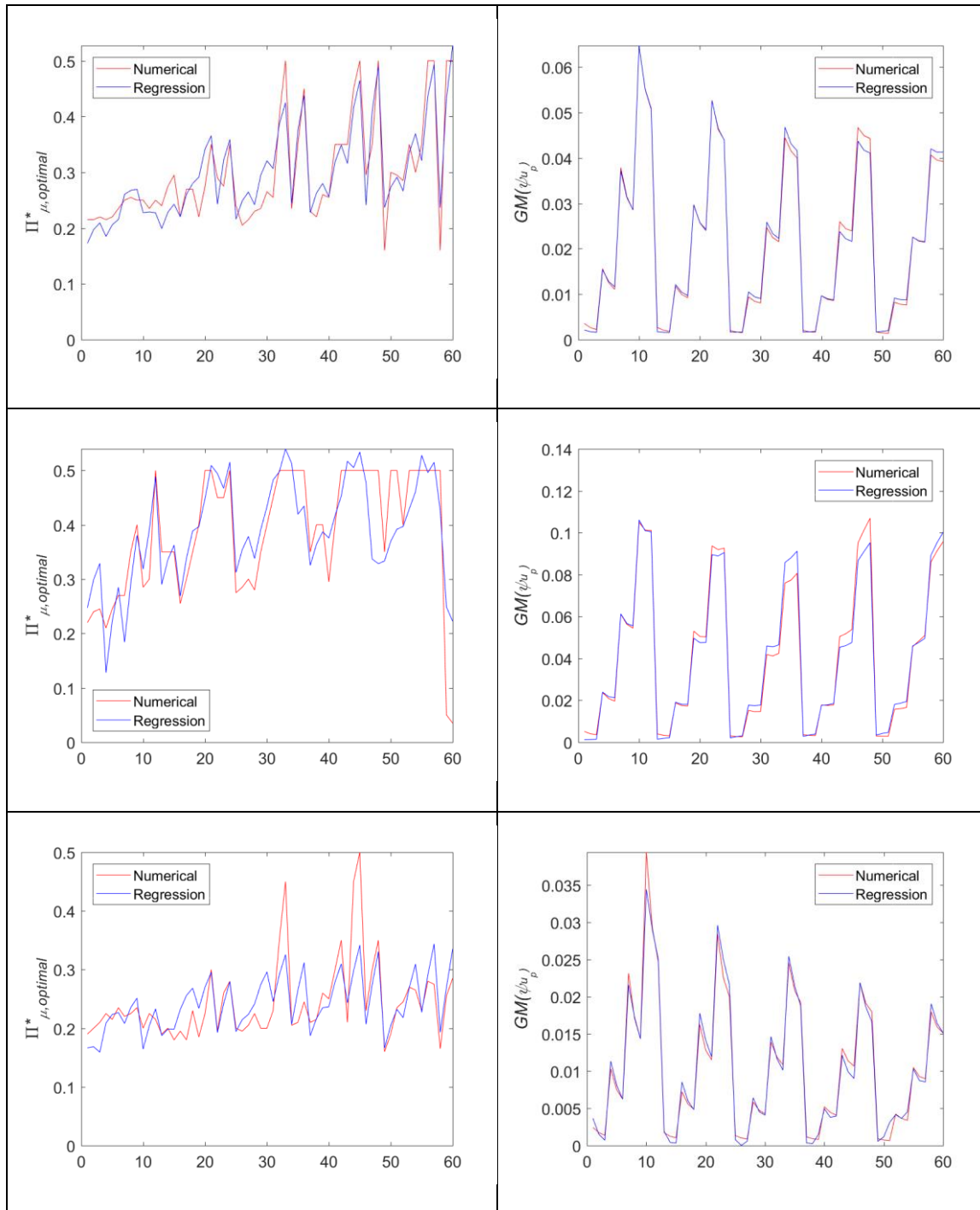


Table 5.30 - Numerical vs regression results: optimal dimensionless friction (left) and pier cap displacement (right) for the 50th, 16th and 84th percentiles (case A).

$$\begin{aligned}
\psi_{x_6}(50^{th}) = & c_1 + c_2 e^{-|T_d-3.5|} + c_3 T_d T_p + c_4 T_p \Pi_\lambda + c_5 e^{-|T_d-3.5|} T_d T_p \\
& + c_6 e^{-|T_d-3.5|} T_p \Pi_\lambda + c_7 T_d \Pi_\lambda T_p^2 + c_8 e^{-2|T_d-3.5|} \\
& + c_9 (T_d T_p)^2 + c_{10} (T_p \Pi_\lambda)^2
\end{aligned} \tag{5.13a,b}$$

$$\begin{aligned}
\psi_{x_6}(84^{th}) = & c_1 + c_2 e^{T_d^2} + c_3 T_p + c_4 \Pi_\lambda + c_5 e^{T_d^2} T_p + c_6 e^{T_d^2} \Pi_\lambda + c_7 T_p \Pi_\lambda \\
& + c_8 e^{T_d^4} + c_9 T_p^2 + c_{10} \Pi_\lambda^2
\end{aligned}$$

	$\psi_{u_p} 50^{th}$		$\psi_{u_p} 84^{th}$	
	$\psi_{x_6} 50^{th}$	$\psi_{x_6} 84^{th}$	$\psi_{x_6} 50^{th}$	$\psi_{x_6} 84^{th}$
R ²	0.8875	0.9532	0.8985	0.9125
c ₁	0.1435	0.2414	0.1764	0.2688
c ₂	0.1028	3.77E-07	1.99E-07	3.81E-07
c ₃	-0.0083	-0.0840	0.0262	-0.5691
c ₄	-0.4395	0.0418	-1.0022	-0.0011
c ₅	-0.0386	2.73E-08	-3.58E-09	5.49E-08
c ₆	0.9590	1.81E-09	1.80E-07	3.34E-08
c ₇	0.0956	1.0827	2.9297	2.3360
c ₈	-0.0326	-4.22E-14	-2.20E-14	-4.33E-14
c ₉	0.0760	0.0547	-0.0309	1.5143
c ₁₀	2.0151	-0.3461	-3.4313	-0.6028

Table 5.31 - Regression analyses results (x₆)

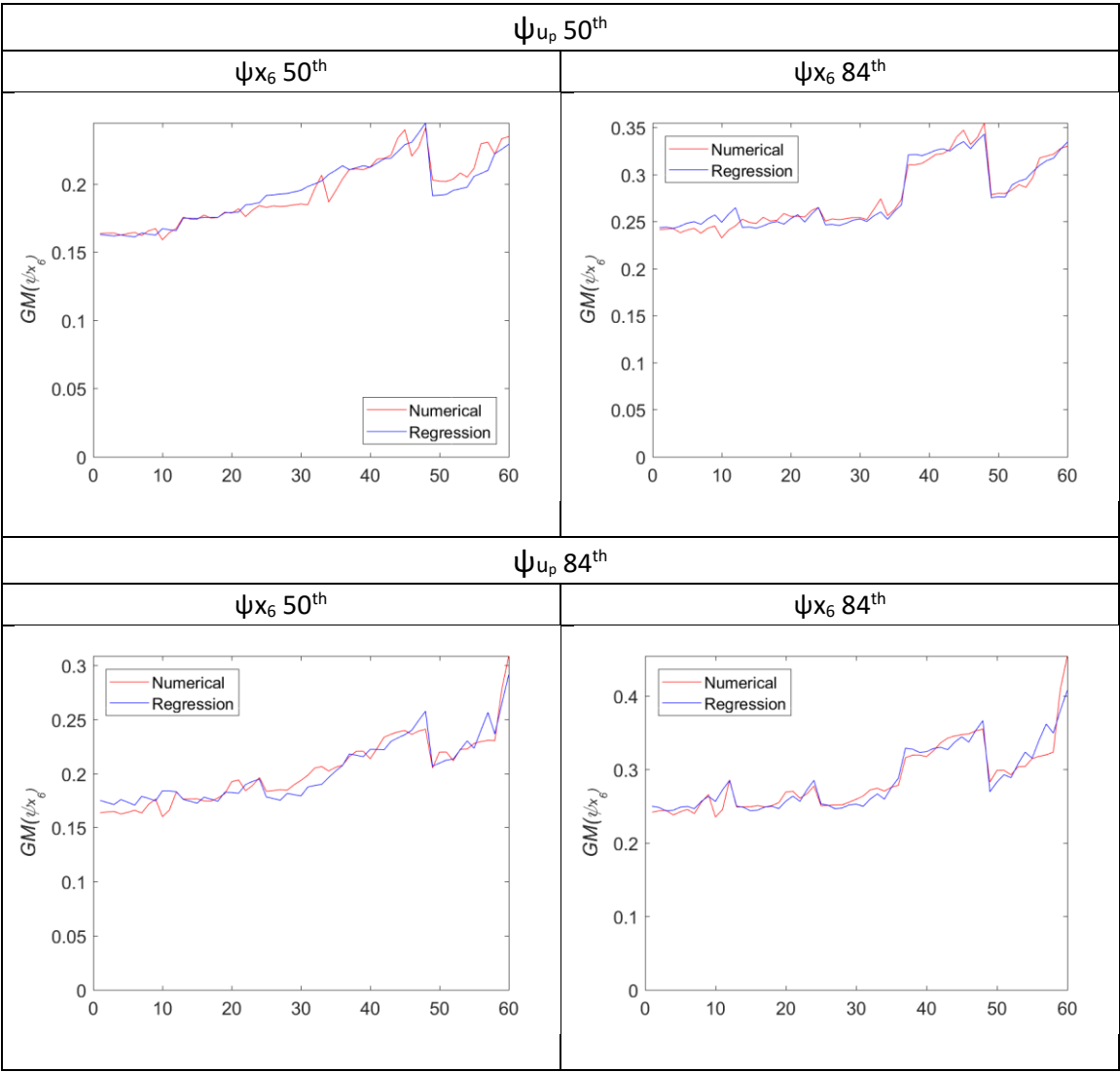


Table 5.32 - Numerical vs regression results (x_6)

$$\psi_{u_p}(50^{th})$$

$$\begin{aligned}\psi_{x_7}(50^{th}) = & c_1 + c_2 e^{|\mathbf{T}_d - 3.5|} + c_3 T_p + c_4 \Pi_\lambda + c_5 e^{|\mathbf{T}_d - 3.5|} T_p \\ & + c_6 e^{|\mathbf{T}_d - 3.5|} \Pi_\lambda + c_7 T_p \Pi_\lambda + c_8 e^{2|\mathbf{T}_d - 3.5|} + c_9 T_p^2 \\ & + c_{10} \Pi_\lambda^2\end{aligned}$$

$$\begin{aligned}\psi_{x_7}(84^{th}) = & c_1 + c_2 e^{-|\mathbf{T}_d - 3.5|} + c_3 T_p + c_4 \Pi_\lambda + c_5 e^{-|\mathbf{T}_d - 3.5|} T_p \\ & + c_6 e^{-|\mathbf{T}_d - 3.5|} \Pi_\lambda + c_7 T_p \Pi_\lambda + c_8 e^{-2|\mathbf{T}_d - 3.5|} + c_9 T_p^2 \\ & + c_{10} \Pi_\lambda^2\end{aligned}$$

$$\psi_{u_p}(84^{th})$$

(5.14a,b,c,d)

$$\begin{aligned}\psi_{x_7}(50^{th}) = & c_1 + c_2 e^{T_d^2} + c_3 \frac{1}{T_p^3} + c_4 \frac{1}{\Pi_\lambda^3} + c_5 \frac{e^{T_d^2}}{T_p^3} + c_6 \frac{e^{T_d^2}}{\Pi_\lambda^3} + c_7 \frac{1}{T_p^3 \Pi_\lambda^3} \\ & + c_8 e^{2e^{T_d^2}} + c_9 \frac{1}{T_p^6} + c_{10} \frac{1}{\Pi_\lambda^6}\end{aligned}$$

$$\begin{aligned}\psi_{x_7}(84^{th}) = & c_1 + c_2 e^{-|\mathbf{T}_d - 3.5|} + c_3 T_p^2 + c_4 \Pi_\lambda^2 + c_5 e^{-|\mathbf{T}_d - 3.5|} T_p^2 \\ & + c_6 e^{-|\mathbf{T}_d - 3.5|} \Pi_\lambda^2 + c_7 T_p^2 \Pi_\lambda^2 + c_8 e^{-2|\mathbf{T}_d - 3.5|} + c_9 T_p^4 \\ & + c_{10} \Pi_\lambda^4\end{aligned}$$

	$\psi_{u_p} 50^{th}$		$\psi_{u_p} 84^{th}$	
	$\psi_{x_7} 50^{th}$	$\psi_{x_7} 84^{th}$	$\psi_{x_7} 50^{th}$	$\psi_{x_7} 84^{th}$
R^2	0.6282	0.7477	0.2707	0.3433
c_1	0.5260	0.5073	0.1658	0.4720
c_2	-0.0838	-0.1469	1.40E-07	-0.2664
c_3	-0.8212	-0.7425	6.04E-06	-7.1669
c_4	-1.3596	-0.4856	5.86E-05	0.1094
c_5	0.0852	0.0046	-1.81E-12	2.6138
c_6	0.1795	-0.4674	-1.21E-11	0.3707
c_7	-3.1848	-2.3226	4.93E-09	78.3303
c_8	0.0069	0.2969	-1.39E-14	0.2839
c_9	3.4411	4.1279	-4.41E-10	104.9726
c_{10}	3.1415	2.4227	-3.99E-08	-32.0527

Table 5.33 - Regression analysis results ($x_7 - A$)

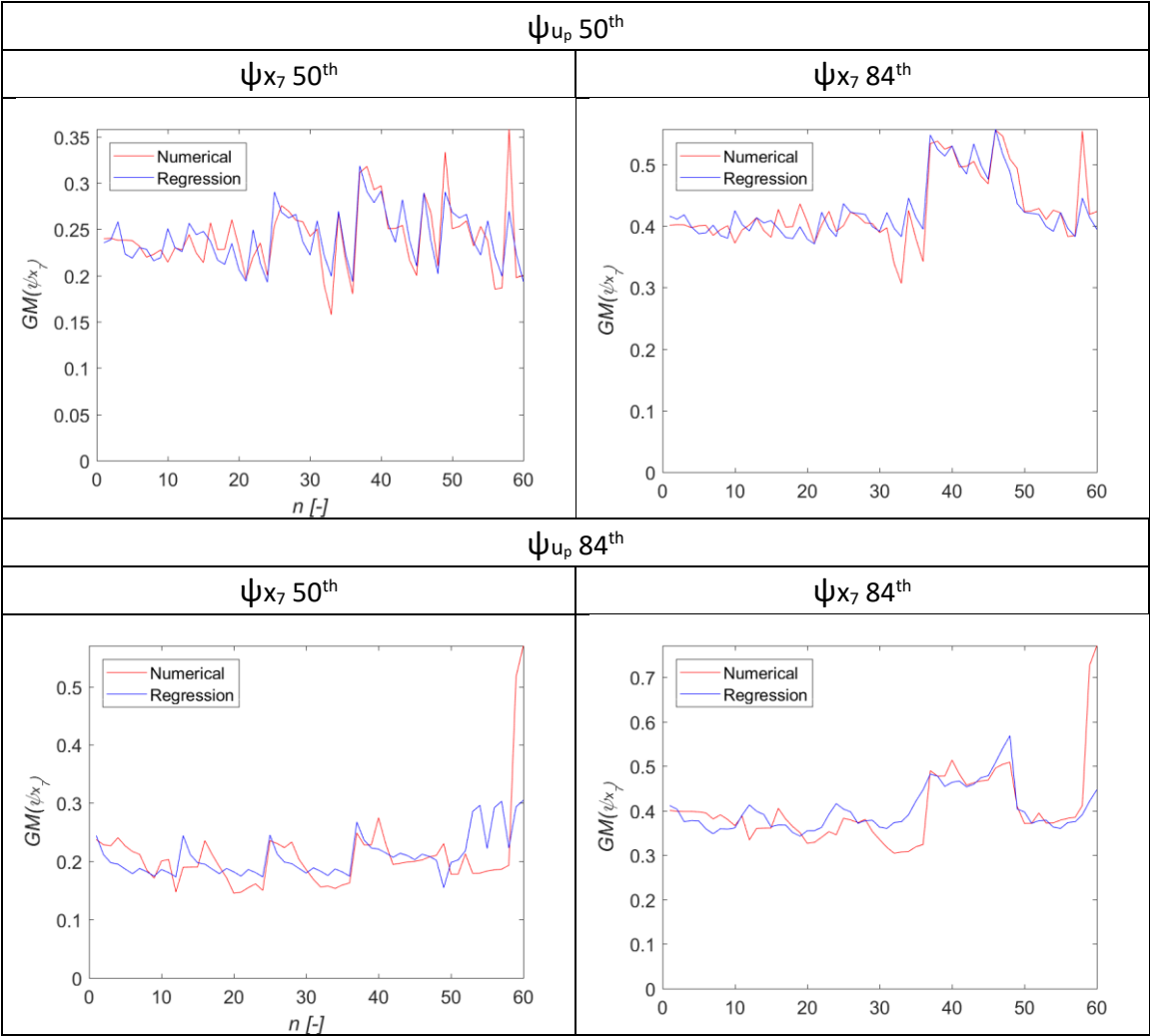


Table 5.34 - Numerical vs regression results ($x_7 - A$)

$$\begin{aligned}
\psi_{x_8}(50^{th}) = & c_1 + c_2 e^{-|T_d - 3.5|} + c_3 T_d T_p + c_4 T_p \Pi_\lambda + c_5 e^{-|T_d - 3.5|} T_d T_p \\
& + c_6 e^{-|T_d - 3.5|} T_p \Pi_\lambda + c_7 T_d \Pi_\lambda T_p^2 + c_8 e^{-2|T_d - 3.5|} \\
& + c_9 (T_d T_p)^2 + c_{10} (T_p \Pi_\lambda)^2 \\
\psi_{x_8}(84^{th}) = & c_1 + c_2 e^{T_d^2} + c_3 T_p + c_4 \Pi_\lambda + c_5 e^{T_d^2} T_p + c_6 e^{T_d^2} \Pi_\lambda + c_7 T_p \Pi_\lambda \\
& + c_8 e^{T_d^4} + c_9 T_p^2 + c_{10} \Pi_\lambda^2
\end{aligned} \tag{5.15a,b}$$

	$\psi_{u_p} 50^{th}$		$\psi_{u_p} 84^{th}$	
	$\psi_{x_8} 50^{th}$	$\psi_{x_8} 84^{th}$	$\psi_{x_8} 50^{th}$	$\psi_{x_8} 84^{th}$
R^2	0.8936	0.9676	0.8702	0.9729
c_1	0.1496	0.2446	0.1366	0.2381
c_2	0.0729	3.29E-07	1.24E-01	3.44E-07
c_3	0.0402	0.0106	-0.0222	0.0234
c_4	-0.8274	0.0106	0.5235	0.0387
c_5	-0.0490	7.51E-09	-6.37E-03	-2.44E-09
c_6	0.8223	7.61E-09	-1.17	4.87E-09
c_7	1.2576	0.6435	2.5328	0.3451
c_8	-0.0107	-3.68E-14	-3.37E-02	-3.82E-14
c_9	-0.0009	-0.1880	0.0369	0.2172
c_{10}	-3.2141	-0.2231	-19.6498	-0.0708

Table 5.35 - Regression analysis results ($x_8 - A$)

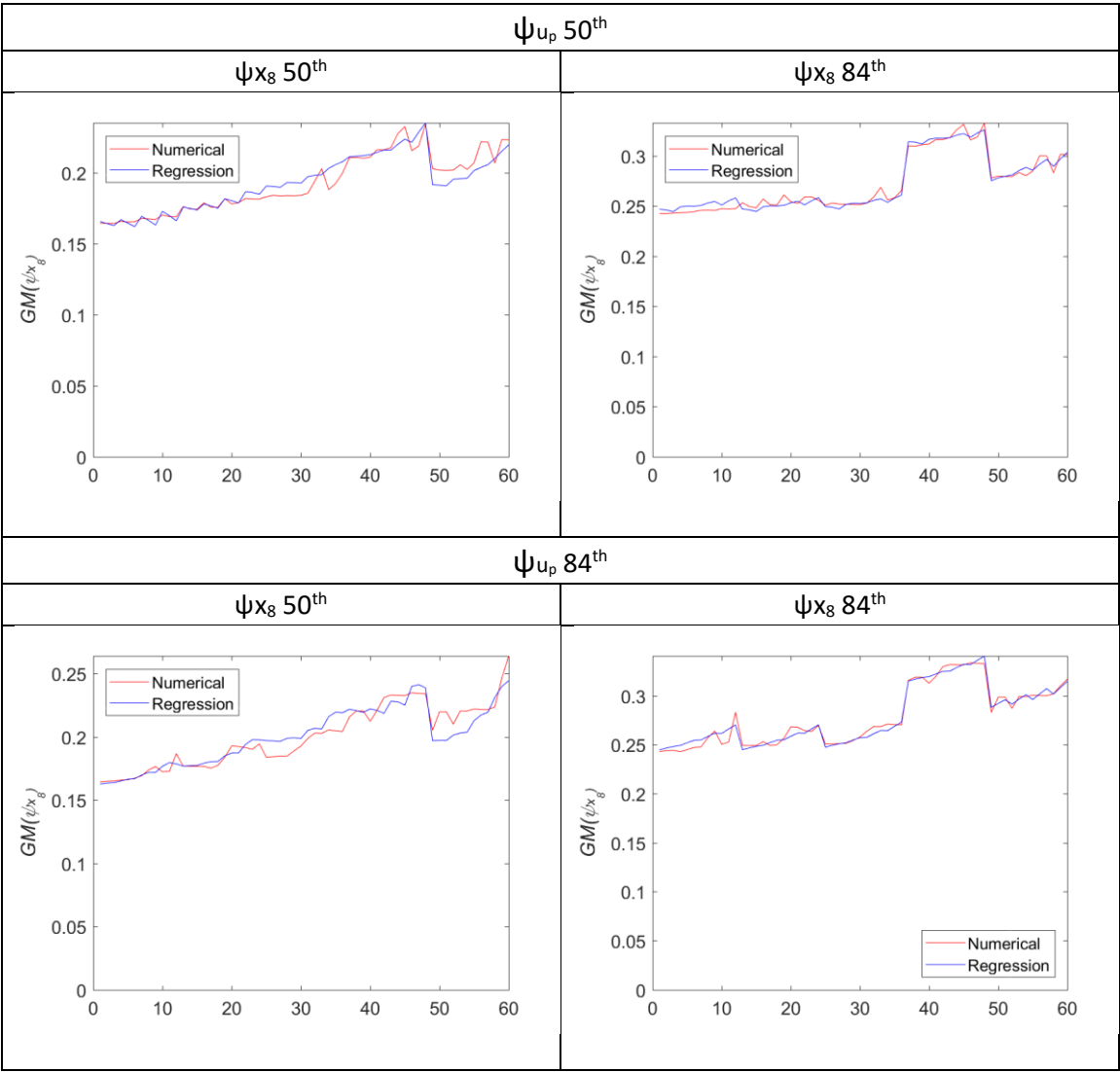


Table 5.36 - Numerical vs regression results ($x_8 - A$)

$$\begin{aligned}\psi_{x_9}(50^{th}) = & c_1 + c_2 e^{|T_d-3.5|} + c_3 T_p + c_4 \Pi_\lambda + c_5 e^{|T_d-3.5|} T_p \\ & + c_6 e^{|T_d-3.5|} \Pi_\lambda + c_7 T_p \Pi_\lambda + c_8 e^{2|T_d-3.5|} + c_9 T_p^2 + c_{10} \Pi_\lambda^2\end{aligned}$$

$$\begin{aligned}\psi_{x_9}(84^{th}) = & c_1 + c_2 e^{-|T_d-3.5|} + c_3 T_p + c_4 \Pi_\lambda + c_5 e^{-|T_d-3.5|} T_p \\ & + c_6 e^{-|T_d-3.5|} \Pi_\lambda + c_7 T_p \Pi_\lambda + c_8 e^{-|T_d-3.5|} + c_9 T_p^2 \\ & + c_{10} \Pi_\lambda^2\end{aligned}$$

$$\begin{aligned}\psi_{x_9}(50^{th}) = & c_1 + c_2 e^{T_d^2} + c_3 \frac{1}{T_p^3} + c_4 \frac{1}{\Pi_\lambda^3} + c_5 \frac{e^{T_d^2}}{T_p^3} + c_6 \frac{e^{T_d^2}}{\Pi_\lambda^3} + c_7 \frac{1}{T_p^3 \Pi_\lambda^3} \\ & + c_8 e^{2e^{T_d^2}} + c_9 \frac{1}{T_p^6} + c_{10} \frac{1}{\Pi_\lambda^6}\end{aligned} \quad (5.16a,b,c,d)$$

$$\begin{aligned}\psi_{x_9}(84^{th}) = & c_1 + c_2 e^{-|T_d-3.5|} + c_3 T_p^2 + c_4 \Pi_\lambda^2 + c_5 e^{-|T_d-3.5|} T_p^2 \\ & + c_6 e^{-|T_d-3.5|} \Pi_\lambda^2 + c_7 T_p^2 \Pi_\lambda^2 + c_8 e^{-2|T_d-3.5|} + c_9 T_p^4 \\ & + c_{10} \Pi_\lambda^4\end{aligned}$$

	$\psi_{u_p} 50^{th}$		$\psi_{u_p} 84^{th}$	
	$\psi_{x_9} 50^{th}$	$\psi_{x_9} 84^{th}$	$\psi_{x_9} 50^{th}$	$\psi_{x_9} 84^{th}$
R ²	0.6695	0.7979	0.2511	0.4108
c ₁	0.5257	0.5012	0.1623	0.4915
c ₂	-0.0837	-0.1748	1.12E-07	-0.3422
c ₃	-0.7969	-0.1106	1.09E-05	-4.6812
c ₄	-1.3638	-0.6003	7.76E-05	-0.7852
c ₅	0.1294	-0.4043	-1.56E-12	0.7167
c ₆	0.1605	-0.3460	-1.12E-11	0.4505
c ₇	-3.6389	-3.0737	3.49E-09	48.5384
c ₈	0.0069	0.3269	-1.10E-14	0.3537
c ₉	3.1554	2.4258	-9.80E-10	70.9599
c ₁₀	3.3661	2.7045	-4.80E-08	-11.8726

Table 5.37 - Regression analysis results ($x_9 - A$)

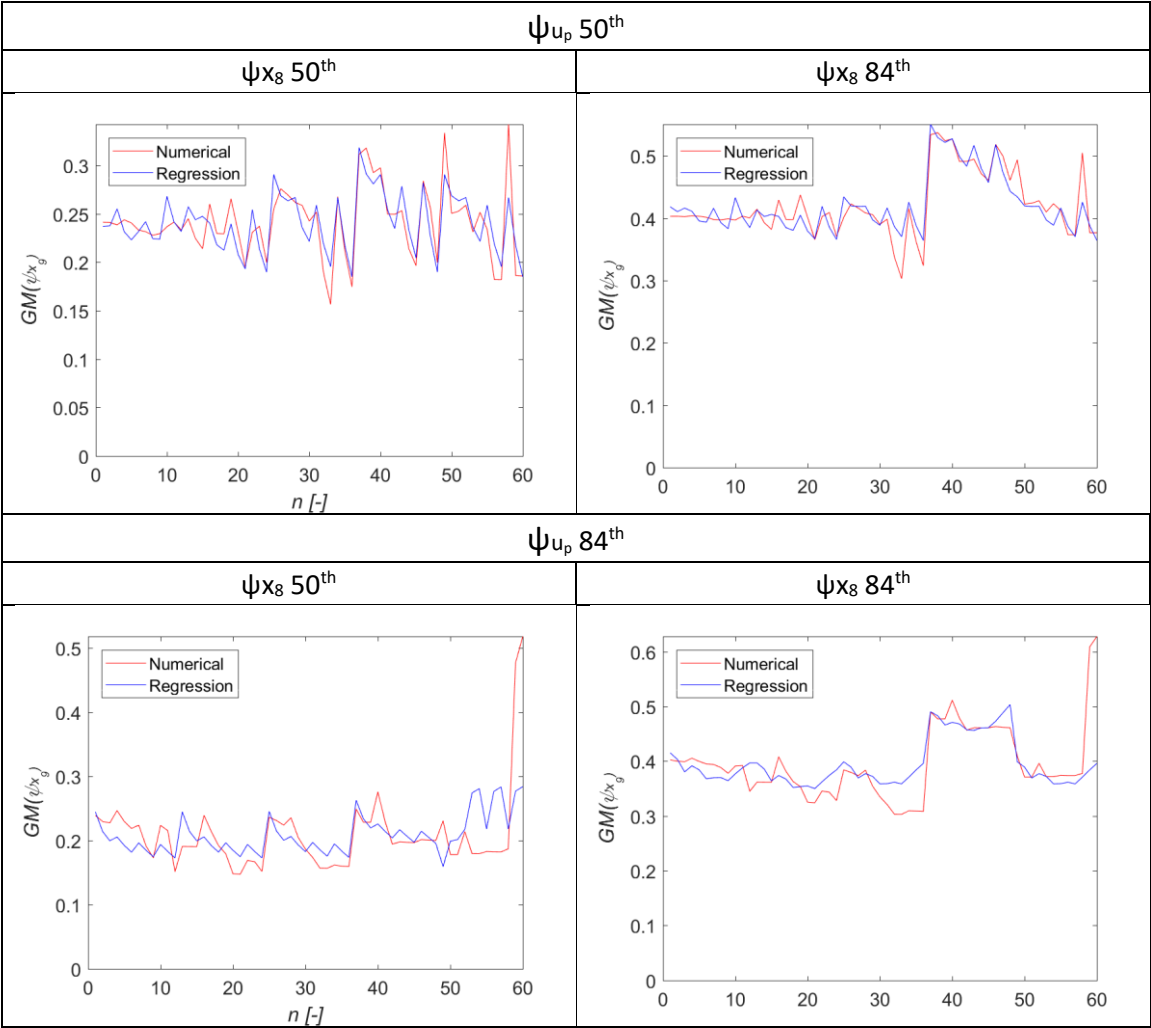


Table 5.38 - Numerical vs regression results ($x_9 - A$)

5.7.2 Case B

$$\begin{aligned}
 & \Pi_{\mu, opt}^*, \psi_{u_p}(50^{th}, 84^{th}) \\
 &= c_1 + c_2 \frac{T_p}{T_d} + c_3 T_p^2 + c_4 \frac{T_p}{\Pi_\lambda} + c_5 \frac{T_p^3}{T_d} + c_6 \frac{T_p}{T_d \Pi_\lambda} + c_7 \frac{T_p^3}{\Pi_\lambda} \\
 &+ c_8 \left(\frac{T_p}{T_d} \right)^2 + c_9 T_p^4 + c_{10} \left(\frac{T_p}{\Pi_\lambda} \right)^2
 \end{aligned} \tag{5.12a,b,c}$$

$$\begin{aligned}
 & \Pi_{\mu, opt}^*, \psi_{u_p}(16^{th}) \\
 &= c_1 + c_2 T_d + c_3 T_p + c_4 \Pi_\lambda + c_5 T_d T_p + c_6 T_d \Pi_\lambda + c_7 T_p \Pi_\lambda \\
 &+ c_8 T_d^2 + c_9 T_p^2 + c_{10} \Pi_\lambda^2
 \end{aligned}$$

	$\Pi_{\mu, opt}^*(50^{th})$	$\psi_{u_p}(50^{th})$	$\Pi_{\mu, opt}^*(84^{th})$	$\psi_{u_p}(84^{th})$	$\Pi_{\mu, opt}^*(16^{th})$	$\psi_{u_p}(16^{th})$
R ²	0.8679	0.9959	0.9343	0.9878	0.7546	0.9868
c ₁	0.2970	0.0015	0.8020	0.0030	0.6540	0.0179
c ₂	-3.8311	-0.1854	-36.3781	-0.4745	-0.3485	-0.0091
c ₃	23.8690	1.0721	113.6140	2.5302	0.0620	0.1901
c ₄	-0.1246	-0.0046	-0.9110	-0.0053	-0.6125	-0.1339
c ₅	95.0531	-12.6499	-1662.1089	-26.4703	0.2920	-0.0389
c ₆	0.5780	0.2645	13.6590	0.2040	0.4875	0.0252
c ₇	1.6006	-0.2837	-43.7227	-0.2384	3.5600	-0.4182
c ₈	-29.0111	4.0219	432.9784	10.4017	0.0488	0.0012
c ₉	-347.0422	11.9866	1265.6092	17.8517	-4.0000	0.4890
c ₁₀	-0.0444	0.0012	0.3588	0.0014	-2.5000	0.2577

Table 5.39 - Regression analysis results (friction and pier cap displacement - B)

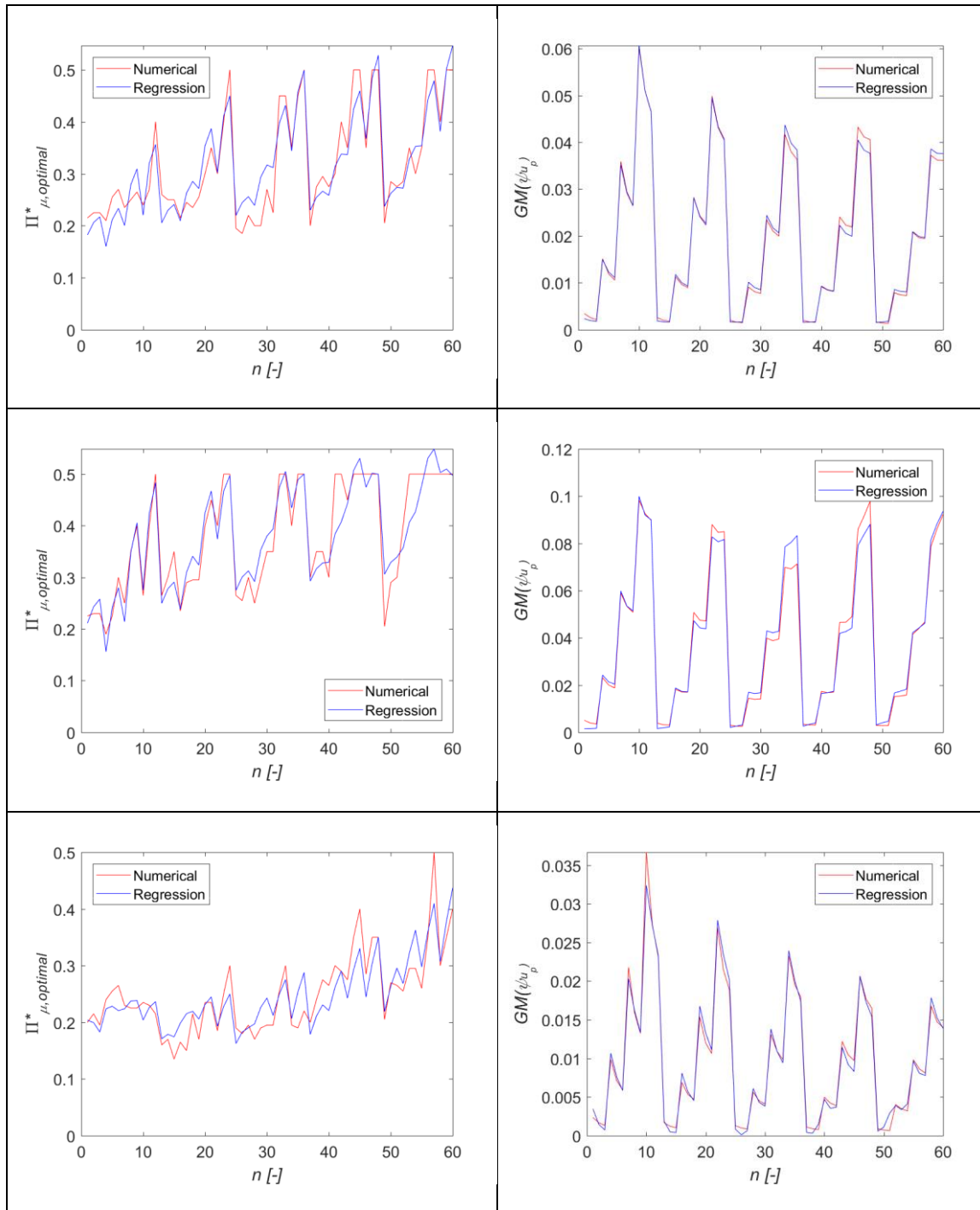


Table 5.40 - Numerical vs regression results: optimal dimensionless friction (left) and top pier displacement (right) for the 50th, 16th and 84th percentiles (case B).

$$\begin{aligned}
\psi_{x_6}(50^{th}) = & c_1 + c_2 e^{-|T_d-3.5|} + c_3 T_d T_p + c_4 T_p \Pi_\lambda + c_5 e^{-|T_d-3.5|} T_d T_p \\
& + c_6 e^{-|T_d-3.5|} T_p \Pi_\lambda + c_7 T_d \Pi_\lambda T_p^2 + c_8 e^{-2|T_d-3.5|} \\
& + c_9 (T_d T_p)^2 + c_{10} (T_p \Pi_\lambda)^2
\end{aligned} \quad (5.13a,b)$$

$$\begin{aligned}
\psi_{x_6}(84^{th}) = & c_1 + c_2 e^{T_d^2} + c_3 T_p + c_4 \Pi_\lambda + c_5 e^{T_d^2} T_p + c_6 e^{T_d^2} \Pi_\lambda + c_7 T_p \Pi_\lambda \\
& + c_8 e^{T_d^4} + c_9 T_p^2 + c_{10} \Pi_\lambda^2
\end{aligned}$$

	$\psi_{u_p} 50^{th}$		$\psi_{u_p} 84^{th}$	
	$\psi_{x_6} 50^{th}$	$\psi_{x_6} 84^{th}$	$\psi_{x_6} 50^{th}$	$\psi_{x_6} 84^{th}$
R^2	0.8839	0.8949	0.8578	0.9059
c_1	0.1868	0.2443	0.1741	0.3121
c_2	-0.0366	0.0001	-0.0358	0.0001
c_3	0.0090	-0.3761	0.0415	-1.1314
c_4	-1.0319	-0.2122	-0.4696	-0.7330
c_5	-0.0319	0.0001	-0.0249	0.0002
c_6	0.5124	0.0000	0.1142	0.0002
c_7	3.2297	1.8090	-0.7002	4.9518
c_8	0.0095	0.0000	0.0113	-3.08E-08
c_9	-0.0405	0.5057	0.0073	1.9708
c_{10}	-22.0727	0.1132	7.5457	0.8264

Table 5.41 - Regression analysis results ($x_6 - B$)

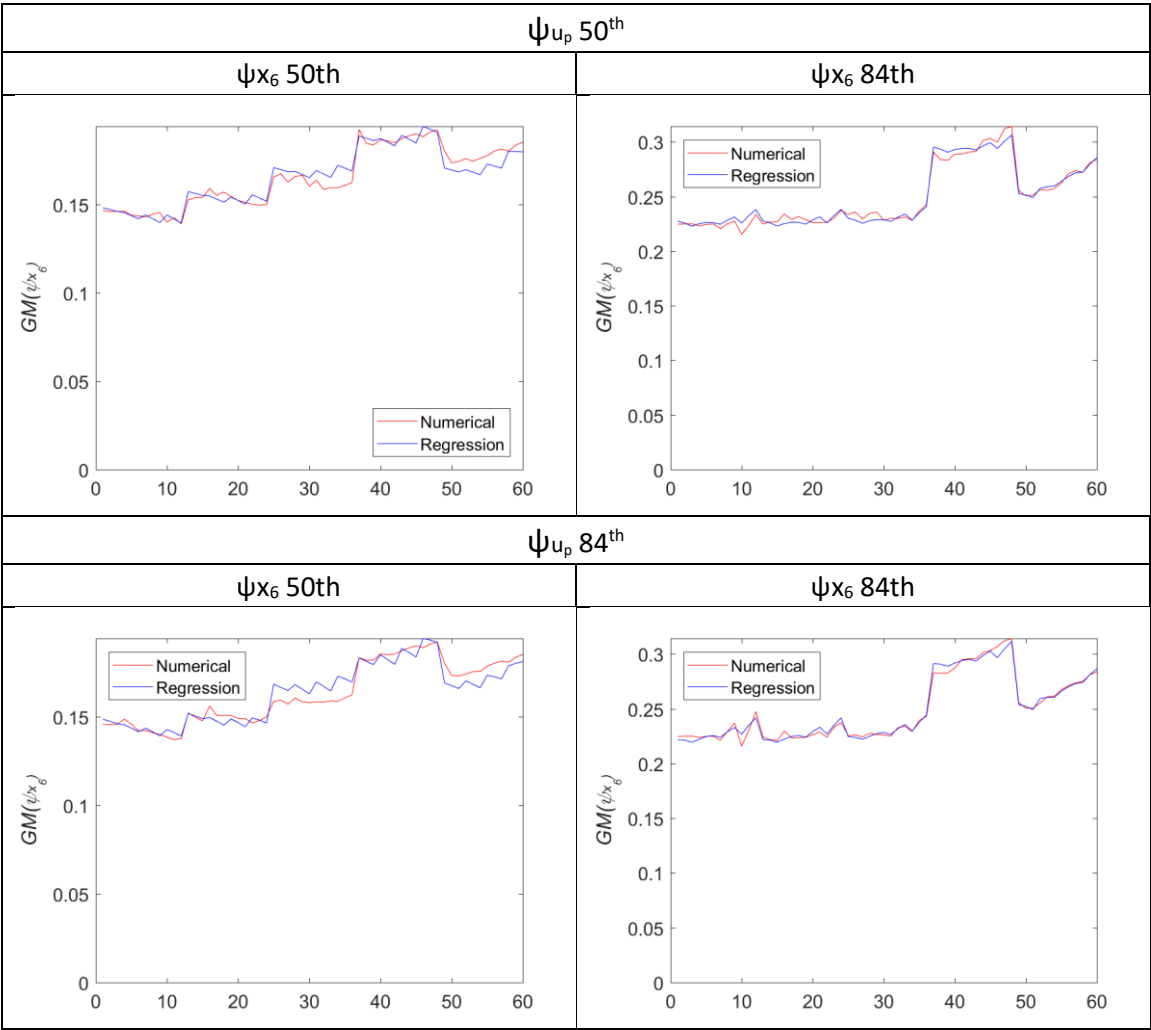


Table 5.42 - Numerical vs regression results ($x_6 - B$)

$$\psi_{u_p}(50^{th})$$

$$\begin{aligned}\psi_{x_7}(50^{th}) = & c_1 + c_2 e^{|T_d-3.5|} + c_3 T_p + c_4 \Pi_\lambda + c_5 e^{|T_d-3.5|} T_p \\ & + c_6 e^{|T_d-3.5|} \Pi_\lambda + c_7 T_p \Pi_\lambda + c_8 e^{2|T_d-3.5|} + c_9 T_p^2 \\ & + c_{10} \Pi_\lambda^2\end{aligned}$$

$$\begin{aligned}\psi_{x_7}(84^{th}) = & c_1 + c_2 e^{-|T_d-3.5|} + c_3 T_p + c_4 \Pi_\lambda + c_5 e^{-|T_d-3.5|} T_p \\ & + c_6 e^{-|T_d-3.5|} \Pi_\lambda + c_7 T_p \Pi_\lambda + c_8 e^{-2|T_d-3.5|} + c_9 T_p^2 \\ & + c_{10} \Pi_\lambda^2\end{aligned}$$

$$\psi_{u_p}(84^{th})$$

(5.14a,b,c,d)

$$\begin{aligned}\psi_{x_7}(50^{th}) = & c_1 + c_2 e^{T_d^2} + c_3 \frac{1}{T_p^3} + c_4 \frac{1}{\Pi_\lambda^3} + c_5 \frac{e^{T_d^2}}{T_p^3} + c_6 \frac{e^{T_d^2}}{\Pi_\lambda^3} + c_7 \frac{1}{T_p^3 \Pi_\lambda^3} \\ & + c_8 e^{2e^{T_d^2}} + c_9 \frac{1}{T_p^6} + c_{10} \frac{1}{\Pi_\lambda^6}\end{aligned}$$

$$\begin{aligned}\psi_{x_7}(84^{th}) = & c_1 + c_2 e^{-|T_d-3.5|} + c_3 T_p^2 + c_4 \Pi_\lambda^2 + c_5 e^{-|T_d-3.5|} T_p^2 \\ & + c_6 e^{-|T_d-3.5|} \Pi_\lambda^2 + c_7 T_p^2 \Pi_\lambda^2 + c_8 e^{-2|T_d-3.5|} + c_9 T_p^4 \\ & + c_{10} \Pi_\lambda^4\end{aligned}$$

	$\psi_{u_p} 50^{th}$		$\psi_{u_p} 84^{th}$	
	$\psi_{x_7} 50^{th}$	$\psi_{x_7} 84^{th}$	$\psi_{x_7} 50^{th}$	$\psi_{x_7} 84^{th}$
R ²	0.8310	0.6942	0.9119	0.8258
C ₁	0.0518	0.4221	0.0869	0.2949
C ₂	0.1252	0.0002	0.1149	0.0002
C ₃	0.9319	0.0802	1.0576	1.2582
C ₄	-0.2166	-0.4345	-0.3264	0.4392
C ₅	-0.2504	-0.0001	-0.3950	-0.0004
C ₆	-0.2219	-0.0001	-0.1870	-0.0002
C ₇	-4.0345	-3.2003	-3.8865	-7.5395
C ₈	-0.0097	0.0000	-0.0097	0.0000
C ₉	-0.5728	0.3283	-0.2859	-2.1791
C ₁₀	2.9996	1.7735	2.4295	-0.0348

Table 5.43 - Regression analysis results (x₇ - B)

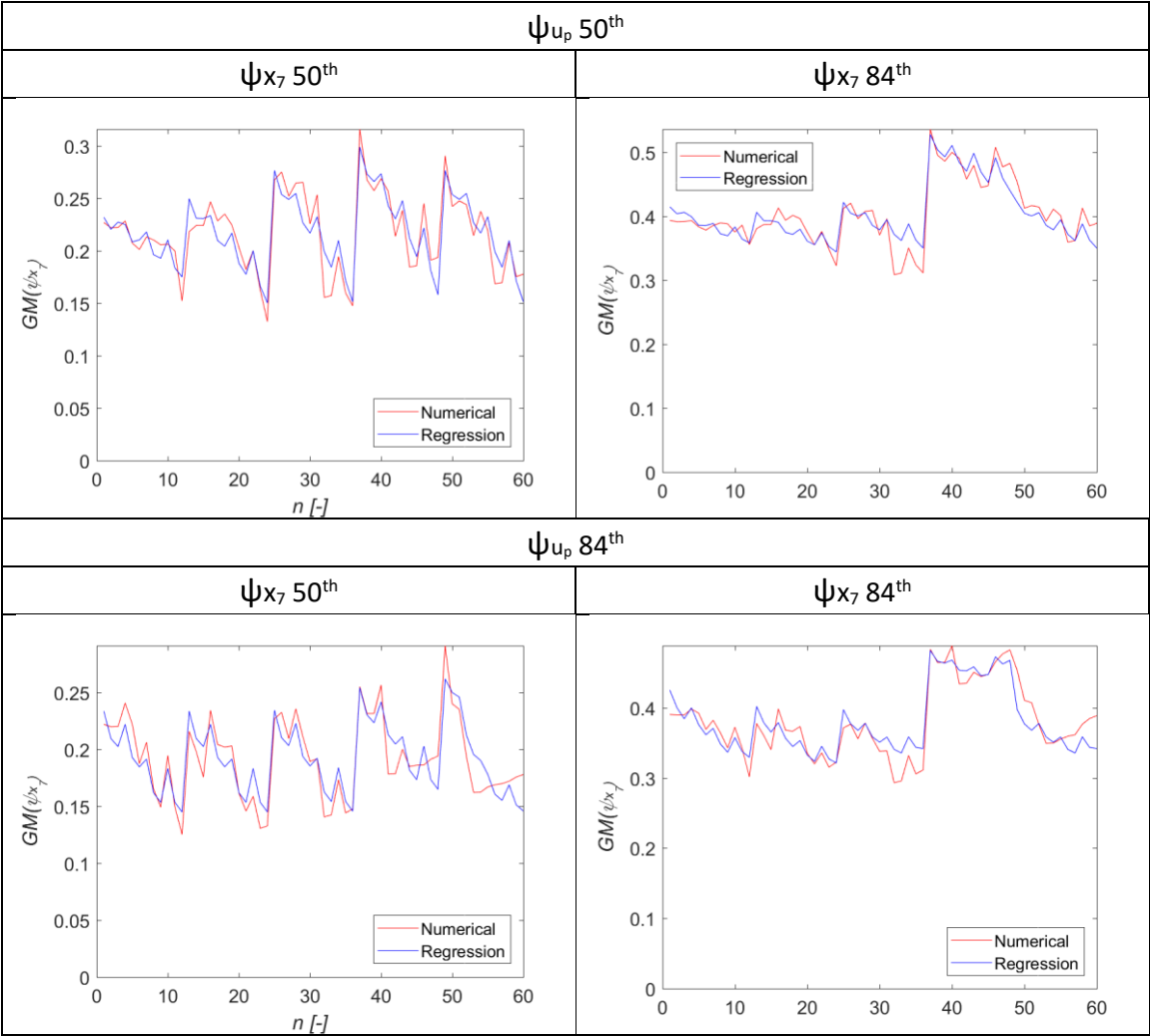


Table 5.44 - Numerical vs regression results ($x_7 - B$)

$$\begin{aligned}
\psi_{x_8}(50^{th}) = & c_1 + c_2 e^{-|T_d-3.5|} + c_3 T_d T_p + c_4 T_p \Pi_\lambda + c_5 e^{-|T_d-3.5|} T_d T_p \\
& + c_6 e^{-|T_d-3.5|} T_p \Pi_\lambda + c_7 T_d \Pi_\lambda T_p^2 + c_8 e^{-2|T_d-3.5|} \\
& + c_9 (T_d T_p)^2 + c_{10} (T_p \Pi_\lambda)^2 \\
\psi_{x_8}(84^{th}) = & c_1 + c_2 e^{T_d^2} + c_3 T_p + c_4 \Pi_\lambda + c_5 e^{T_d^2} T_p + c_6 e^{T_d^2} \Pi_\lambda + c_7 T_p \Pi_\lambda \\
& + c_8 e^{T_d^4} + c_9 T_p^2 + c_{10} \Pi_\lambda^2
\end{aligned} \tag{5.15a,b}$$

	$\psi_{u_p} 50^{th}$		$\psi_{u_p} 84^{th}$	
	$\psi_{x_8} 50th$	$\psi_{x_8} 84th$	$\psi_{x_8} 50th$	$\psi_{x_8} 84th$
R^2	0.8735	0.8518	0.8412	0.8936
c_1	0.1870	0.2498	0.1758	0.3066
c_2	-0.0389	0.0001	-0.0382	0.0001
c_3	0.0126	-0.2692	0.0366	-0.9477
c_4	-1.1507	-0.2895	-0.6615	-0.6966
c_5	-0.0096	0.0000	-0.0051	0.0002
c_6	0.3731	0.0000	0.0676	0.0002
c_7	3.0525	1.2568	-0.1259	4.0965
c_8	0.0101	0.0000	0.0116	-2.72E-08
c_9	-0.0492	0.4353	-0.0006	1.7268
c_{10}	-18.3014	0.4369	4.5647	0.8535

Table 5.45 - Regression analysis results ($x_8 - B$)

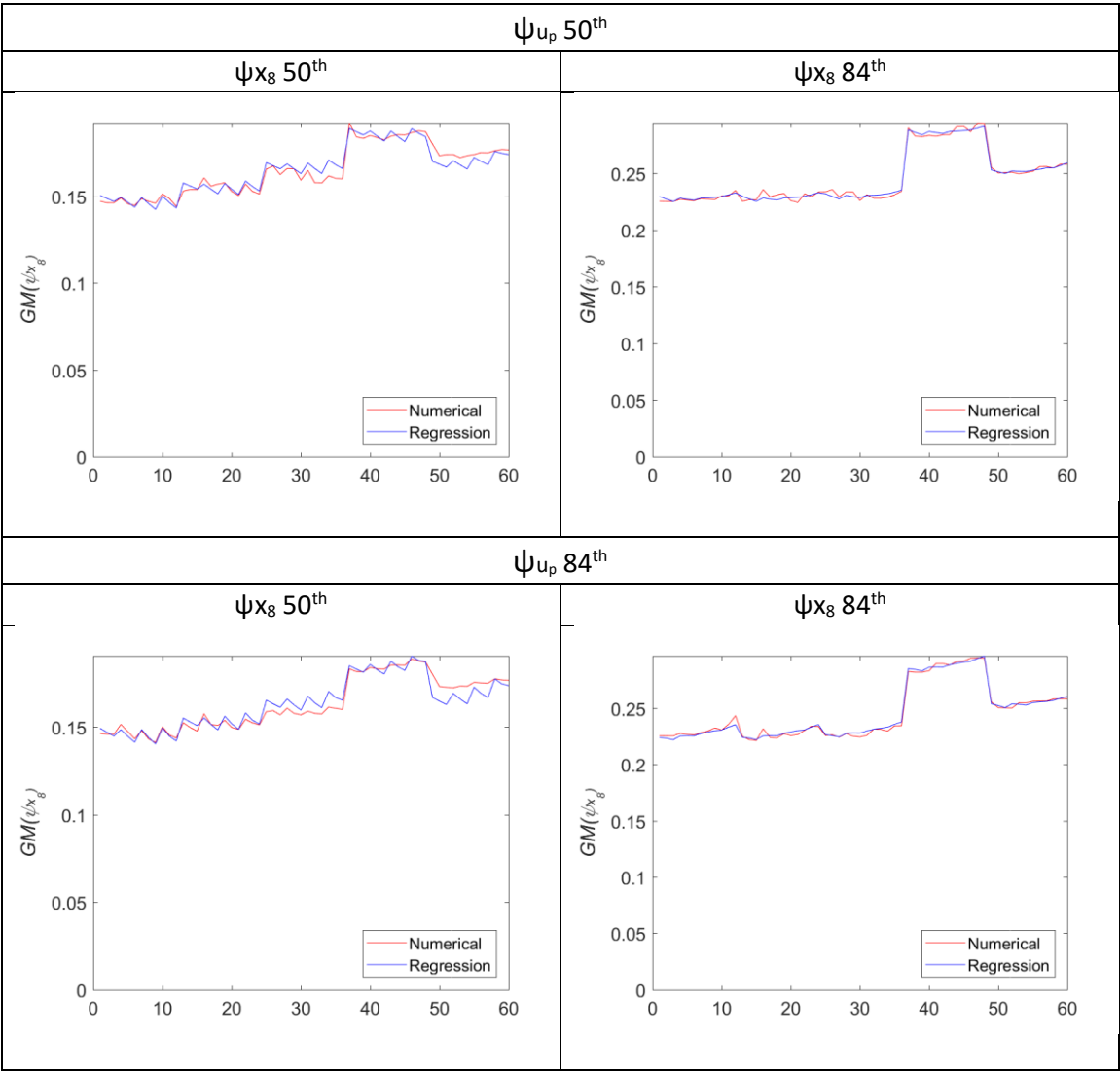


Table 5.46 - Numerical vs regression results ($x_8 - B$)

$$\begin{aligned}\psi_{x_9}(50^{th}) = & c_1 + c_2 e^{|T_d-3.5|} + c_3 T_p + c_4 \Pi_\lambda + c_5 e^{|T_d-3.5|} T_p \\ & + c_6 e^{|T_d-3.5|} \Pi_\lambda + c_7 T_p \Pi_\lambda + c_8 e^{2|T_d-3.5|} + c_9 T_p^2 + c_{10} \Pi_\lambda^2\end{aligned}$$

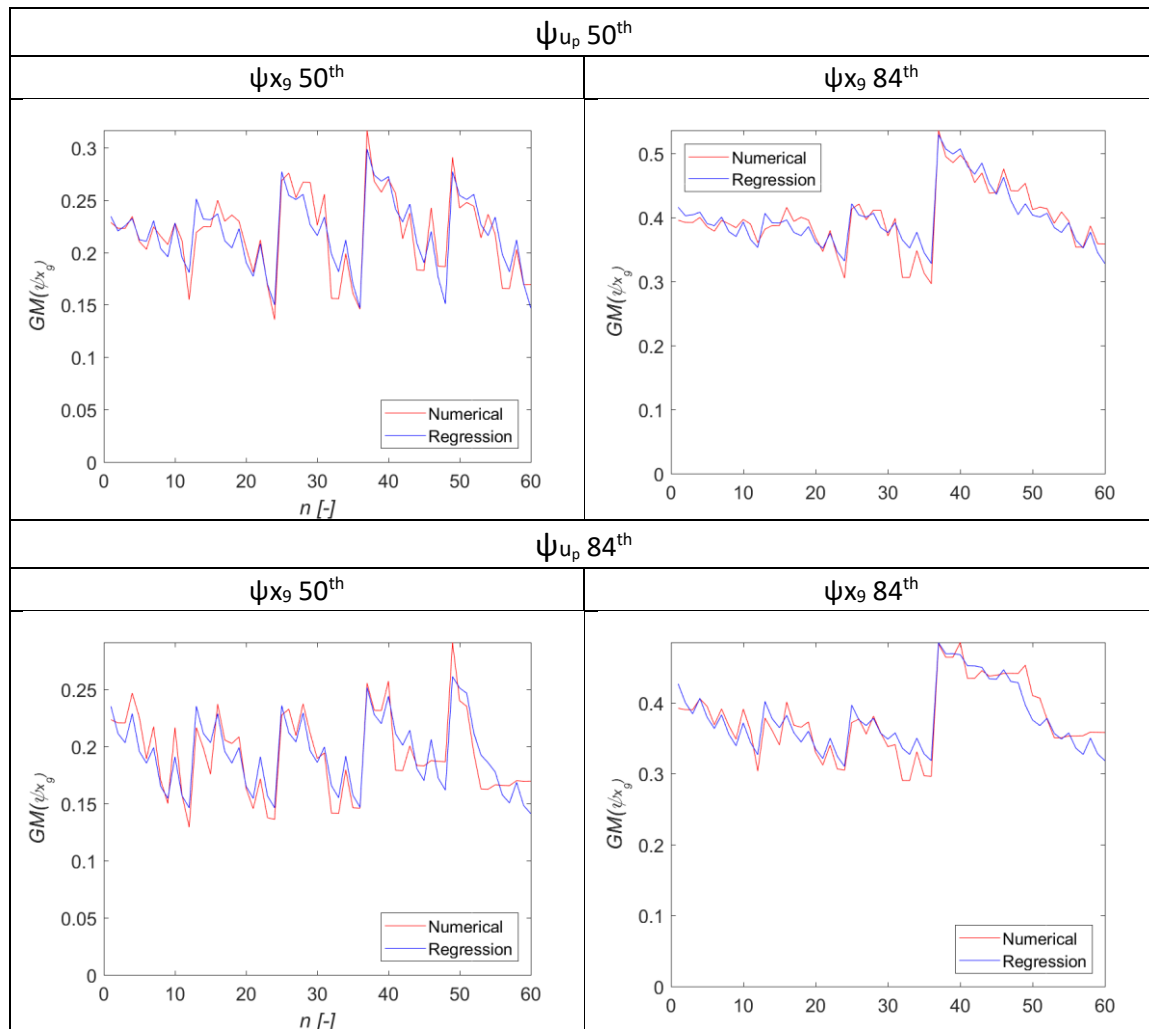
$$\begin{aligned}\psi_{x_9}(84^{th}) = & c_1 + c_2 e^{-|T_d-3.5|} + c_3 T_p + c_4 \Pi_\lambda + c_5 e^{-|T_d-3.5|} T_p \\ & + c_6 e^{-|T_d-3.5|} \Pi_\lambda + c_7 T_p \Pi_\lambda + c_8 e^{-|T_d-3.5|} + c_9 T_p^2 \\ & + c_{10} \Pi_\lambda^2\end{aligned}$$

$$\begin{aligned}\psi_{x_9}(50^{th}) = & c_1 + c_2 e^{T_d^2} + c_3 \frac{1}{T_p^3} + c_4 \frac{1}{\Pi_\lambda^3} + c_5 \frac{e^{T_d^2}}{T_p^3} + c_6 \frac{e^{T_d^2}}{\Pi_\lambda^3} + c_7 \frac{1}{T_p^3 \Pi_\lambda^3} \\ & + c_8 e^{2e^{T_d^2}} + c_9 \frac{1}{T_p^6} + c_{10} \frac{1}{\Pi_\lambda^6}\end{aligned} \quad (5.16a,b,c,d)$$

$$\begin{aligned}\psi_{x_9}(84^{th}) = & c_1 + c_2 e^{-|T_d-3.5|} + c_3 T_p^2 + c_4 \Pi_\lambda^2 + c_5 e^{-|T_d-3.5|} T_p^2 \\ & + c_6 e^{-|T_d-3.5|} \Pi_\lambda^2 + c_7 T_p^2 \Pi_\lambda^2 + c_8 e^{-2|T_d-3.5|} + c_9 T_p^4 \\ & + c_{10} \Pi_\lambda^4\end{aligned}$$

	$\psi_{u_p} 50^{th}$		$\psi_{u_p} 84^{th}$	
	$\psi_{x_9} 50^{th}$	$\psi_{x_9} 84^{th}$	$\psi_{x_9} 50^{th}$	$\psi_{x_9} 84^{th}$
R^2	0.8357	0.7073	0.9113	0.8221
c_1	0.0741	0.4272	0.1194	0.3039
c_2	0.1149	0.0001	0.0991	0.0002
c_3	1.1110	0.3136	1.1438	1.3015
c_4	-0.3644	-0.5277	-0.4704	0.3966
c_5	-0.2997	-0.0001	-0.4168	-0.0004
c_6	-0.1795	-0.0001	-0.1477	-0.0002
c_7	-4.3840	-3.6971	-4.3072	-7.7978
c_8	-0.0086	0.0000	-0.0079	0.0000
c_9	-0.4299	-0.4489	0.0305	-2.2513
c_{10}	3.1085	2.0340	2.5881	0.0120

Table 5.47 - Regression analysis results ($x_9 - B$)

Table 5.48 - Numerical vs regression results ($x_9 - B$)

6 Conclusions

Numerical investigations have been carried out on 5700 different systems by varying the main dynamic parameters and for two different cases. 30 different time history seismic input have been used, for a total amount of simulation performed is 342.000: performing all of them required about 1000 hours (40 days ca.) The analyses led to results sometimes hard to interpret due to both the non-linearity and the randomness of the seismic input, especially in the regression analyses. The results of the analyses are summarized as follows:

- The GM and the β of the output parameters increase with Π_λ . This is generally true, excepts for some output parameters which show an opposite trend: the ψ_{u_p} , ψ_{x_8} , ψ_{x_9} and the forces. This means that the displacement of the pier's top, the deformation of the DCFP placed on the abutment (along both surfaces) and the forces transmitted by both the DCFP decrease with Π_λ .
- $GM(\psi_{u_d})$ and $GM(\psi_{x_d})$ increase with Π_μ , T_p and, as expected, T_d , even if they seem to stabilize for high period such as $T_d = 3.5$ or 4 s. $\beta(\psi_{u_d})$ and $\beta(\psi_{x_d})$ decrease with Π_μ and T_p , and is trend becomes regular for Π_μ slightly larger than 0. They are not correlated to T_d , since they oscillate with it.
- $GM(\psi_{x_6})$ and $GM(\psi_{x_8})$ show an absolute maximum for Π_μ , and then a relative minimum and a relative maximum. They also increase with T_p and with T_d , stabilizing for high values of the latter (3.5 – 4 s). $\beta(\psi_{x_6})$ and $\beta(\psi_{x_8})$,
- $GM(\psi_{x_7})$ and $GM(\psi_{x_9})$ show an hyperbolical behaviour for Π_μ , decreasing monotonically with it. They also increase with T_p and with T_d , stabilizing for high values of the latter (3.5 – 4 s). $\beta(\psi_{x_7})$ and $\beta(\psi_{x_9})$, increase with Π_μ until they reach a very high maximum, approximately around $\Pi_\mu = 1.5$. Also, they decrease with T_p and increase with T_d ,
- All the measured forces show a minimum for Π_μ between 0.2 – 0.3, and increase slightly with T_p and T_d .

6.1 Optimal friction values

The optimal dimensionless friction values, obtained as the ones that gives the minimum top pier displacement, depends on the percentile of the displacement considered for the pier's top displacement.

- 16th percentile: the optimal friction is essentially stable, between 0.2 and 0.3, for small T_d (2 s, 2.5 s) even though it is generally increasing with T_p , T_d and Π_λ . It reaches a peak at $T_p = 0.15$ s, $\Pi_\lambda = 0.2$ in both Cases.
- 50th percentile: in the Case A, the optimal friction is stable only for $T_d = 2$ s. For higher values, it increases with T_p and T_d but not regularly, showing sometimes slope inversion along a direction. This may cause several problems during the regression analysis. In the Case B $\Pi_{\mu, \text{opt}}$ increases anyway with T_p , T_d and Π_λ , but the mesh is sufficiently regular to obtain better regression analysis results, as it will be discussed later. A plateau with $\Pi_{\mu, \text{opt}}$ is reached both with $T_d = 3.5$ s and 4 s, larger than the one seen in Case A.
- 84th percentile: in the Case A, values increase with the parameter but often in a non-monotonic way. For $T_d = 4$ s, $\Pi_{\mu, \text{opt}}$ drops at near zero values for $T_p = 0.2$ s: this event could be considered as an outlier. In the Case B, the mesh of the optimums is practically the same, but without the abovementioned irregularities, forming a plateau for $T_d = 3.5$ s and 4 s, bigger than the one obtained in the 50th percentile, as expected.

6.2 Regression analyses

Regression analyses have been carried out to determine expressions useful to estimate the optimal friction values of the DCFP surfaces, the pier cap lateral displacement and the deformation of the isolators along each surface.

According to the values of the R^2 coefficients, the Case B regression analyses are clearly more accurate: by choosing $R_1 = 2R_2$ and adopting a smaller f_1/f_2 (2 instead of 4, but similar values may be adopted) the response of the system become more predictable with the derived expressions. Small friction surfaces show in any case a more predictable behaviour, according to the high values of R^2 reached by regression analyses of ψ_{x_6} and ψ_{x_8} . Due to their minor engineering interest and the

difficulties faced in regression of the optimal dimensionless friction values, 16th percentile values were not considered for regression.

6.3 Practical application

A short example of an application is here showed. Let us consider a bridge situated in L'Aquila, Italy: the geographic position and the site characteristics determine the a_0 input (spectral acceleration value for the design T_d), through the determination of the acceleration spectra, following the guidelines provided by (NTC, 2008). It is then possible to estimate the median value of the pier's cap displacement, the in-plant radii of the sliding surfaces necessary to ensure the isolator's deformability and the deck lateral deck displacement, which is necessary to design expansion joints and, if any, pipes and cables passing along the bridge. This procedure may be done for any Limit State, by varying the a_0 input.

It is assumed that $R_1 + R_2 = 1.5$ m, $V_N = 100$ years, $C_U = 1.5$.

T_d [s]	2.457
ω_d^2 [s ⁻²]	6.540
T_p [s]	0.13
Π_λ [-]	0.18

50th percentile

a_0 [m/s ²]		SLV		SLC	
		2.277		2.534	
$\Pi_{\mu,opt}$ [-]	0.3308	$f_{1,max}$ [-]	0.0768	$f_{1,max}$ [-]	0.0855
		$f_{2,max}$ [-]	0.0384	$f_{2,max}$ [-]	0.0427
ψ_{u_p} [-]	0.0172	$u_{p,max}$ [mm]	5.98	$u_{p,max}$ [mm]	6.66
ψ_{x_6} [-]	0.1501	$x_{6,max}$ [cm]	5.23	$x_{6,max}$ [cm]	5.82
ψ_{x_7} [-]	0.1892	$x_{7,max}$ [cm]	6.59	$x_{7,max}$ [cm]	7.33
ψ_{x_8} [-]	0.1514	$x_{8,max}$ [cm]	5.27	$x_{8,max}$ [cm]	5.87
ψ_{x_9} [-]	0.1898	$x_{9,max}$ [cm]	6.61	$x_{9,max}$ [cm]	7.36

84th percentile

a_0 [m/s ²]		SLV		SLC	
		2.277		2.534	
$\Pi_{\mu,opt}$ [-]	0.3985	$f_{1,max}$ [-]	0.0925	$f_{1,max}$ [-]	0.1029
		$f_{2,max}$ [-]	0.0463	$f_{2,max}$ [-]	0.0515
ψ_{u_p} [-]	0.0323	$u_{p,max}$ [mm]	11.24	$u_{p,max}$ [mm]	12.51
ψ_{x_6} [-]	0.2554	$x_{6,max}$ [cm]	8.89	$x_{6,max}$ [cm]	9.90
ψ_{x_7} [-]	0.3548	$x_{7,max}$ [cm]	12.35	$x_{7,max}$ [cm]	13.75
ψ_{x_8} [-]	0.2577	$x_{8,max}$ [cm]	8.97	$x_{8,max}$ [cm]	9.98
ψ_{x_9} [-]	0.3541	$x_{9,max}$ [cm]	12.33	$x_{9,max}$ [cm]	13.72

6.4 Future developments

The results of this study may be a starting point for further developments of the research.

- Having obtained the probability distribution of each relative displacement necessary to design an isolation system and the closed-form expressions for the 50th and the 84th percentiles, it could be interesting perform a statistic study to evaluate safety coefficients. This may be necessary to compensate the uncertainty linked to the closed-form expressions with small values of R^2 .
- The entire study may be performed again with Triple Friction Pendulum instead of DCFP bearings. The higher quantity of variables would require more simplifying assumptions, or, alternatively, a much higher number of numerical simulations.
- Bridges with variable height piers may be introduced, even considering 2nd order effects on the piers if and where necessary.
- The vertical component of the earthquake records may be considered, even considering 2nd order effects if and where necessary.

7 References

- Ang, & Tang. (2007). *Probability Concepts in Engineering - Emphasis on Applications to Civil and Environmental*.
- Azienda Accelerometrica Italiana (ITACA). (2016).
- Bowden, & Tabor. (1950, 1964, 1973).
- Castaldo, P., & Tubaldi, E. (2015). Influence of FPS bearing properties on the seismic performance of base-isolated structures. *Earthquake Engineering & Structural Dynamics*, 2817-2836.
- Castaldo, P., Amendola, G., & Palazzo, B. (2016). Seismic Reliability-based Design of Structures Isolated by FPS. (pp. 8431-8444). National Technical University of Athens.
- Constantinou, F. a. (n.d.). *2008a, 2008b*.
- Constantinou, M. C. (2004). *Friction Pendulum Double Concave Bearing*. State University of New York, Buffalo, NY. Retrieved from <http://nees.buffalo.edu/docs/dec304/FP-DC%20Report-DEMO.pdf>
- Constantinou, M. C., & Fenz, D. (2006). Behaviour of the double concave friction pendulum bearing. *Earthquake Engineering and Structural Dynamic*(35), 1403-24.
- Constantinou, Whittaker, Kalpakidis, Fenz, & Warn. (2007). Performance of Seismic Isolation Hardware Under Service and Seismic Loading.
- DPC-INGV S1 Project*. (2106). Retrieved from <http://esse1-gis.mi.ingv.it/>
- Fenz, D. M., & Constantinou, M. C. (2008). *Modeling Triple Friction Pendulum Bearings for Response Analysis, in Earthquake Spectra, Volume 24, No. 4*. Earthquake Engineering Research Institute.
- Ghasemi, H. (2004). Bolu Viaduct: Damage Assessment and Retrofit Strategy. *36th Joint Meeting - Panel on Wind and Seismic Effects*. Tsukuba, Japan: Public Works Research Institute.
- Iervolino, I., Cosenza, E., & Galasso, C. (2009). Spettri, accelerogrammi e le nuove norme tecniche per le costruzioni. *Progettazione Sismica*.

- Imhof, D. (2004). *Risk Assessment of Existing Bridge Structures*. VDM.
- Internet Site for European Strong Motion Data*. (2016).
- Kelly, J. M. (1990, May). Base Isolation: Linear Theory and Design, Vol. 6, No. 2. *Earthquake Spectra*, pp. 317-333.
- Kelly, J. M., & Naeim, F. (1999). *Design of Seismic Isolated Structures: from Theory to Practice*. John Wiley & Sons.
- Kelly, J. M., & Naeim, F. (1999). *Design of Seismic Isolated Structures: from Theory to Practice*. John Wiley & Sons, Inc.
- Kim, Y.-S., & Yun, C.-B. (2007). *Seismic response characteristics of bridges using double concave friction pendulum bearings with tri-linear behavior*.
- Lapointe, E. M. (2004). *An Investigations of the Principles and Practices of Seismic Isolation in Bridges Structures*. Retrieved from DSpace@MIT: <http://hdl.handle.net/1721.1/29412>
- Mohka, A., Constantinou, M., & Reinhorn, A. (1990, February 1). Teflon Bearings in Base Isolation I: Testing. *Journal of Structural Engineering*.
- Mohka, A., Constantinou, M., & Reinhorn, A. (1990, February 1). Teflon Bearings in Base Isolation II: Modeling . *Journal of Structural Engineering*.
- NTC. (2008). *Nuove Norme Tecniche per le Costruzioni*.
- Pacific Earthquake Engineering Research Center (PEER)*. (2006).
- Priestley, M., Seible, F., & Calvi, G. (1996). *Seismic Design and Retrofit of Bridges*. Wiley.
- Tubaldi, E. (2014). Probabilistic Seismic Response Assessment of Linear Systems Equipped. *Earthquake Engineering & Structural Dynamics*.
- Zayas, V. A., Low, S. S., & Mahin, S. A. (1990, May). A Simple Pendulum Technique for Achieving Seismic Isolation. *Earthquake Spectra*, pp. 317-333.

